

Mechanical Behaviour of Nanomaterials, Metallic Glasses and Advanced Materials

20th Technical Meeting, 2011
Paris, France

20



DESIGNING INNOVATIVE MATERIALS : THE STRATEGY OF ARCHITECTURED MATERIALS

Y. Bréchet

*Membre de l'Académie des Sciences
SIMAP, Grenoble Institute of Technology, BP75
38402 Saint Martin d'Herès Cedex, France*

In the general evolution of high performance materials, one can observe that the classical distinction between “structural” and “functional” materials is fading away. The requirements of weight and energy savings, the need to save resources, leads to the development of multifunctional materials. An emerging strategy for these materials consists in associating different materials, in a well controlled geometry. As a result, the classical distinction between materials and structures becomes less relevant. A number of challenges, both from a scientific and from a technological viewpoint, emerge and the key role of modelling methods and developing innovative processes will be outlined. Examples taken from different industrial fields will illustrate this deep evolution in materials design.

MECHANICAL PROPERTIES OF METALLIC GLASSES : RECENT ADVANCES

L. Greer

University of Cambridge, Department of Materials Science & Metallurgy Cambridge CB2 3QZ, United Kingdom

Metallic glasses (MGs) possess the highest yield stresses within the family of metallic materials [1]. Their toughness, however, covers a wide range and can be exceedingly low. It is correlated with their elastic properties, expressed as the ratio of shear to bulk moduli, or as Poisson's ratio ν [2]. This has guided the selection of MG compositions. Unfortunately, the high values of ν that favour toughness also correlate with worse glass-forming ability [3]. Another compromise in materials properties is that between yield stress and toughness. Recent work at CalTech has produced a bulk MG with high yield stress and high toughness [4,5]. Even more remarkable, especially for a monolithic glass, is that this material has a damage tolerance (the product of yield stress and toughness) that is higher than any other known material! We will consider this and related results, and consider whether the toughness of MGs might be still further improved. Our work has shown that elastic anisotropy induced in MGs is most evident for ν , which varies $\sim 10\%$ with orientation [6], easily spanning the range associated with brittleness or toughness [2]. Thus toughness might vary with orientation, permitting tailoring of properties, analogous to effects in aligned composites. Thus the recent results [4] on damage tolerance might be transcended. It is particularly pleasing that ν retains so much interest and importance in 2011, the 200th anniversary of the publication of Poisson's seminal work *Traité de Mécanique*.

References

- [1] M. F. Ashby, A. L. Greer, *Scripta Mater.* **54** (2006) 321-326.
- [2] J.J. Lewandowski, W.H. Wang, A.L. Greer, *Philos. Mag. Lett.* **85** (2005) 77.
- [3] G. N. Greaves, A. L. Greer, R. S. Lakes, T. Rouxel, *Nature Mater.*, submitted.
- [4] M.D. Demetriou et al., *Nature Mater.* **10** (2011) 123.
- [5] A.L. Greer, *Nature Mater.* **10** (2011) 88.
- [6] A. Concustell et al., *Scripta Mater.* **64** (2011) 1091.

FRACTURE TOUGHNESS-YIELD STRENGTH TRADE-OFF IN STEELS AND OTHER MATERIALS INCLUDING BULK METALLIC GLASSES

A. Pineau

*Membre de l'Académie des Technologies
Centre des Matériaux – Mines Paris-Tech B.P. 87 – 91003 Evry Cedex, France*

This presentation deals essentially with the ductile-to-brittle transition (DBT) in structural steels. In the introduction several definitions for the DBT temperature are given. It is shown that the ratio between the shear modulus, μ , and the bulk modulus, k , plays a key role in this transition. The theoretical work by Rice [1, 2] has shown that in crystalline materials ductile fracture defined as the emission of dislocations from a blunted crack occurs when the ratio μ/k is below a critical value. Recent studies on bulk metallic glasses (BMG) have shown a similar behaviour in these materials (see e.g. [3, 4]). In Zr based BMG it has been demonstrated that the fracture toughness can reach values as large as 100 KJ/m² (similar to those observed in steels) when the Poisson ratio reaches values of the order of 0.4, that is for small values of the μ/k ratio. In these BMG materials, crack blunting is linked to the formation of shear bands at the crack front. In structural steels brittle cleavage fracture is associated with the nucleation of cleavage cracks at carbide particles located ahead of the crack tip. The micromechanisms and the mechanics of cleavage fracture in these materials are also briefly described in the introduction. In particular the importance of grain boundaries as potential crack arrestors is underlined.

The second part of the presentation is devoted to the theories which have been recently developed to account for the temperature dependence of fracture toughness, K_{IC} , the scatter and the size effect observed in measurements of K_{IC} , and the influence of metallurgical inhomogeneities. Analytical expressions relating the fracture toughness and the yield strength for a given probability of failure are presented. The toughening effect of grain boundaries in polycrystalline materials is analyzed in some detail.

The third part deals with the initiation, the growth and the coalescence of cavities from second-phase particles (inclusions or precipitates). Only a short account on the modeling of ductile fracture is given. The main emphasis is laid on the transition. An attempt is made to explain the reasons for the existence of this transition observed in many materials, in particular in ferritic steels. It is shown that the DBT behaviour observed in fracture mechanics specimens or in Charpy impact tests can now be modelled using local fracture criteria introduced in finite element simulations (see e.g. [5]).

In the conclusion the emphasis is laid on a number of research studies which have to be made for a better understanding of the trade-off between the yield strength and the fracture toughness of materials.

References

- [1] Rice J.R. and Thomson, *Phil. Mag.* 29 (1974) 73-97.
- [2] Rice J.R., *J. Mech. Phys. Solids* 40 (1992) 239-271.
- [3] Lewandowski J.J., Wang W.H. and Greer A.L., *Phil. Mag. Letters* 85 (2005) 77-87.
- [4] Hennan D. and Anand L, *Acta Mater.* 57 (2009) 6057-6074.
- [5] Pineau A., *Int. J. Fract.* 150 (2008) 129-156.

ULTRA-HIGH STRENGTH MATERIALS – DO WE NEED HOMGENEOUS OR HETEROGENOUS STRUCTURES ?

D. Embury

*Adjunct Professor
UBC Vancouver, Canada*

For many engineering structures we envisage using materials which have strength levels approaching the theoretical limit; In general this imposes limits on the combinations of strength and ductility we can achieve. Thus it is useful to examine if we can develop some general guidelines to help in the development of these materials. This presentation will examine some possible guidelines and also explore whether these structures should be homogenous or heterogenous eg architected in form.

NANOSTRUCTURED METALS : FROM THE NANOSCALE TO THE MICROSACLE

E. Lavernia

Distinguished Professor

Department of Chemical Engineering and Materials Science

University of California, Davis, CA 95616, USA

Abstract Nanostructured (i.e., 1–100 nm grain size) and ultrafine-grained (i.e., 100–1000 nm grain size) metals with multiple-length-scale microstructures are of interest due to their unusual combinations of physical and mechanical properties. Cryomilled nanostructured Al powders, for example, provide unique characteristics that can be tailored as hierarchical architectures given their excellent thermal stability which renders them ideal for various fabrication methods. In this overview, cryomilled materials are reviewed and discussed paying particular attention to the balance between strength and ductility; primary consolidation and secondary processing methods; microstructural evolution during consolidation; and mechanical response of consolidated materials. The deformation behavior and the underlying mechanisms are discussed in an effort to shed light into the fundamental behavior of hierarchical nanostructured materials.

1. INTRODUCTION

Nanostructured materials, in which the grain sizes are usually in the range of 1~100 nm, and ultra-fine grained materials, in which the grain sizes are in the range of 100-1000 nm, have the potential of revolutionizing traditional materials design via atomic-level structural control to tailor engineering properties. Mechanical attrition/milling (MA), a widely used approach for synthesis of nanostructured materials, induces severe cyclic plastic deformation in powders and promotes the formation of nanostructures [1]. Mechanical alloying/milling has demonstrated the capability to generate a variety of nanostructured powders, such as single-phase (bcc, fcc and hcp) metals, intermetallic compounds, and numerous alloys [2-5]. The major advantage often quoted is its simplicity, the applicability to essentially all classes of materials [3], and the ability to introduce structures with multiple length-scales, ranging from the micronscale to nanoscale [6], for various applications. Similarly, the drawbacks that are usually cited are: i) contamination from milling media and /or atmosphere, and ii) the need to consolidate the powder product without coarsening the nanostructures. The cryogenic mechanical milling, or “cryomilling” process [7], can be effectively used to produce nanostructured aluminum alloys while diminishing contamination from atmosphere (powder protected from inert cryogenic liquid [7]) and milling medium (low input energy, low diffusivity at cryogenic temperatures), and has been successfully employed to produce a number of bulk nanostructured alloys. In addition, oxide, nitride and oxy-nitride dispersoids, 2-10 nm in diameter and with a mean spacing of 50-100 nm in the Al matrix, presumably formed *in-situ* during cryomilling by the co-adsorption of nitrogen and oxygen onto clean aluminum surfaces, contribute to the enhanced thermal stability of nanostructures generated by cryomilling [8]. In other alloys, the reported increase in thermal stability in cryomilled Fe-Al powders has been attributed in part to the formation of the ultra-fine oxy-nitride particles (γ -Al₂O₃ and AlN) during cryomilling [9]. It has also been shown that cryomilling may provide grain size stabilization in other alloy compositions such as Ni-Al [10].

Partly due to the enhanced thermal stability that is introduced during cryomilling, bulk nanostructured Al alloys have been fabricated by using various commercial available powder metallurgy techniques, such as hot isostatic pressing, quasi-isostatic forging, spark plasma sintering, hot extrusion, and etc. Despite the numerous published studies by groups around the world, the high strength is often accompanied by low ductility. One possible origin for the low ductility in powder metallurgy synthesized nanostructured materials may be attributed to processing artifacts include porosity, insufficient interfacial bonding and impurities [11]. However, even in cases when the extrinsic artifacts are not present, their ductility is still very low, which is mainly due to premature force/necking instabilities, i.e., low strain hardening rate which is caused by their low dislocation storage efficiency resulting from their small grains and/or nearly saturated dislocation density [12]. Therefore, improving the low ductility of nanostructured materials can be achieved by postponing/suppressing strain localization or elevating their strain hardening rate, or both. An example of the former approach is to introduce a bi- or multi-modal grain size distribution [13-15]. Xiang et al. [16] demonstrated that nanostructured Cu films well bonded on a polymer substrate can sustain tensile strains up to 10% without appreciable cracks and up to 30% with discontinuous microcracks. By contrast, poorly bonded Cu films form channel cracks at strains about 2%. More recently, Fang et al. [17] showed that nanostructured Cu films

confined by a coarse grained Cu substrate can sustain a tensile true strain exceeding 100% without cracking through suppressing strain localization with a gradient grain size transition. The latter approach includes introducing pre-existing nano-scale growth/deformation twins [18-20], nano-particles/precipitates in a nanostructured matrix [21], multiple-phase alloys or composites [22], phase-transformation plasticity [23], or high-angle grain boundaries and low dislocation density [24]. In nano-twinned Cu prepared by electrodeposition, Lu et al. [19] exhibited ultra-high yield strength (900 MPa) and good ductility (13%). In nanostructured Al 7075 prepared by HPT, Liddicoat et al. [25] showed that the hierarchical architecture including high density of dislocations, subnanometer intragranular solute clusters, and nanometer-scale intergranular solute structures, and nanoscale grains (average size 26 nm) is responsible for the combined high strength (~ 1GPa) and ductility (~8%).

In this paper, our knowledge of bottom-up fabrication of nanostructured and ultrafine grained materials is reviewed and the consolidation techniques are discussed. More specifically, the present review addresses the following topics: cryomilling mechanisms and thermal stability; consolidation approaches; and mechanical behavior of consolidated materials. The mechanical behavior and the associated mechanisms underlying the behavior of cryomilled Al alloys are discussed in an effort to shed light into the fundamental behavior of ultrafine-grained and nanostructured materials with hierarchical architectures.

2. NANOSTRUCTURED POWDER VIA CROMILLING AND ITS THERMAL STABILITY

Powder evolution during the cryomilling process involves three distinct stages, i.e., (i) particle flattening, (ii) unsteady particle welding and fracture, (iii) equiaxed particle formation and steady-state deformation, during which a balance between fracture and cold welding is established as microstructural refinement approaches the material limit (~25 nm for Al), as shown in Figure 1. In view of the fact that severe plastic deformation during milling is a stochastic process, adequate milling time is required in order to obtain a microstructure with nanoscale grain sizes. There are several advantages to cryomilling as compared to milling at room temperature. First, powder welding to the milling media is suppressed, resulting in a more efficient milling outcome. Second, oxidation reactions during milling are reduced under the protection of inert cryogenic liquid environment. Third, the milling time required to attain a nanostructure is significantly reduced, because the low temperature suppresses the annihilation of dislocations and the accumulation of a higher dislocation density is possible. As an example, a high density of dislocations of $1.7 \times 10^{17} \text{ m}^{-2}$ was observed in a cryomilled Al-Mg alloy [26, 27].

With approaching the minimum grain size approached after ~8 hours, continued cryomilling does not lead to further grain refinement, however, the nitrogen content continues to increase leading to the formation of nitrides or oxynitride phases that dramatically increase thermal stability of the nanostructured powder, as shown in Figure 2. The excellent thermal stability thus provides a wide processing window to consolidate the nanostructured powder to different length scales using a variety of techniques.

3. CONSOLIDATION OF CRYOMILLED POWDERS

Engineering application of nanostructured metallic powders requires efficient methods of consolidation to produce bulk materials with close to 100% theoretical density. Several commercially available approaches are currently being used to consolidate the nanostructured metallic and composite powders, including as hot isostatic pressing (HIP), CeraconTM forging (quasi-isostatic forging), cold isostatic pressing (CIP), spark plasma sintering (SPS), followed by secondary thermomechanical procedures such as CeraconTM forging, extrusion, and others to further improve the consolidation quality. The pressure and temperature are two critical parameters for consolidation. HIP has been widely used as a primary consolidation route. Since the consolidation of the milled powder usually requires high temperatures for extended time periods, grain growth is likely to occur. In the case of HIP consolidation, diffusional processes can lead to micron-size grains forming in the triple point areas between the nano-grained prior powder particles, the applied pressure can also lead to stress assistant growth of the nano-grains. To avoid significant grain growth during consolidation, CIP has been employed to consolidate cryomilled powders. Compared to HIP processing, CIP is operated at room temperature, but with a much higher isostatic pressure. Although nearly full density is attainable in the CIP'ed materials followed by secondary thermomechanical processing, the ductility of the materials processed via CIP is generally low. This is due to the presence of prior particle boundaries, usually decorated with a surface oxide, that are not removed during consolidation. To break up and disperse the prior particle boundaries, a shear stress needs to be applied to the material. Therefore, secondary processing, such as extrusion, rolling or

forging is generally required. Ceracon forging is found to be effective to break up the prior particle boundaries during the primary consolidation step.

4. MECHANICAL PROPERTIES OF CRYOMILLED MATERIALS

The true tensile stress curves as a function of true strain of 5083 Al alloys processed via four different routes are shown in Figure 3(a). The cryomilled 5083 Al alloy consolidated via CIP and extrusion showed mono-modal grain size distribution with an average value of approximately 150–200 nm [28]. The cryomilled 5083 Al alloy consolidated via HIP and extrusion exhibited a bimodal grain size distribution with small grains of about 30 nm, and some large grains of approximately several hundred nanometers [15]. For comparison, a mono-modal 5083 Al alloy consolidated via a different HIP and extrusion route with the mean grain size of about 500 nm is also included in the figure [29]. The coarse-grained 5083 Al alloy has a grain size of 200 μm [30]. The highest value of yield strength of 713MPa is observed in the cryomilled 5083 Al alloy consolidated via CIP and extrusion. However, this sample shows an extremely low ductility of 0.3%. The ductility in cryomilled Al alloys decreases with decreasing grain size, as observed in many other nanostructured materials. In an effort to enhance the ductility of nanostructured materials, Tellkamp et al. [15] demonstrated the capability to tailor the mechanical properties of a nanostructured cryomilled 5083 Al alloy by introducing a bimodal grain size distribution. The bimodal 5083 Al shows a yield strength of 334MPa, ultimate strength of 462MPa and an elongation of 8.4%. By contrast, the mono-modal 5083 Al with an average grain size of 500 nm consolidated by HIP and extrusion showed higher strength but lower ductility. Similar results were attained in cryomilled 5083 Al composite with a tri-modal microstructure, as shown in Figure 3(b). The tri-modal composite consists of 10% B₄C particles, 30% unmilled coarse-grained 5083 Al and the balance nanostructured 5083 Al. It is interesting to note that this material exhibits high yield strength of over 1 GPa when it consolidated via CIP and extrusion. Significant micro-yielding was not observed in the elastic deformation region of the stress–strain curve, although the yield strength of the coarse-grained 5083 Al regions is much lower than that in nanostructured 5083 Al regions. This unique phenomenon can be explained in terms of the load transfer associated with the tri-modal microstructure [31] and hierarchical architecture [32]. The applied load on the coarse-grained Al can be effectively transferred to the nanocrystalline Al, because a good interface between the coarse-grained Al and the nanocrystalline Al have developed during consolidation due to the same chemical composition. In the tri-modal composite, however, the load applied on the nanocrystalline Al is further transferred to the stronger B₄C particles due to a clean interface between the nanocrystalline Al and the B₄C that forms during cryomilling. In order to improve material plasticity, a strategy was utilized to generate multiple-length-scales grain structure. As mentioned previously, this approach (in terms of the hierarchical strategy, n=1) has provided a pathway to tailor material systems with targeted combinations of mechanical properties by blending nanostructured powders with coarser-grained powders in prescribed proportions. When a crack generated in a nano-grained region reaches the coarse-grained region, it encounters soft, ductile grains that dissipate energy, slow the advancing crack, and enhance ductility on a macroscopic level. Recently, cryomilling has been extended to synthesize nano-grained 5083 Al alloy matrix reinforced with boron carbide (B₄C) particles (n=2) (ultra-high strength) and coarse-grained (high toughness) 5083 Al matrix alloy regions [33], which have been shown to exhibit a compressive strength of over 1GPa with tailorable ductility by controlling the consolidation routes, as shown in Figure 3(b).

5. SUMMARY

Bulk nanostructured Al alloys and composites have matured into a new class of materials that is being considered in a variety of structural applications. More importantly, the nanoscale provides materials scientists with an additional degree of freedom to design microstructures with unusual physical and mechanical attributes. The successful synthesis of large-scale so-called multi-scale materials is of technological and scientific significance. From a technological point of view, it will be feasible to obtain engineering materials that retain the structural and chemical attributes of particles/grains in the nanometer size range. From scientific point of view, multi-scale materials will permit systematic investigations of the physical and mechanical behavior, as well as novel phenomena as related to multiple length scales.

Acknowledgements

The author would like to acknowledge financial support by the Office of Naval Research (Grant number ONR N00014-08-1-0405).

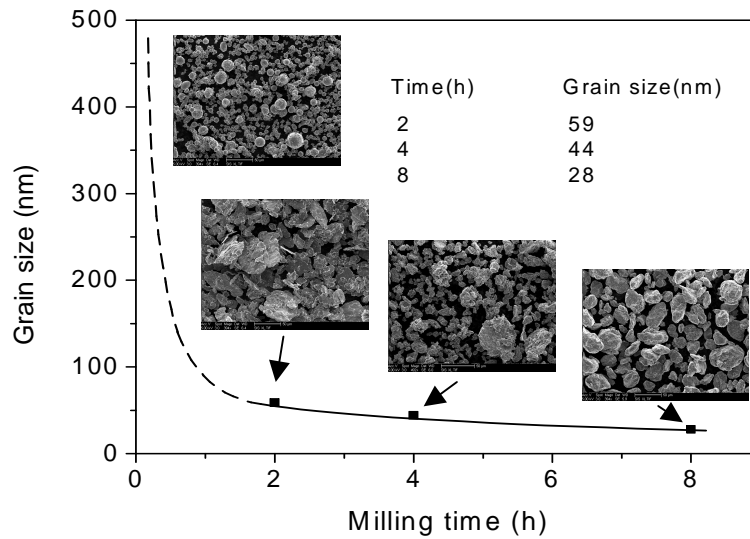


Figure 1. Grain size and powder particle morphology of Al 5083 as a function of cryomilling time [6].

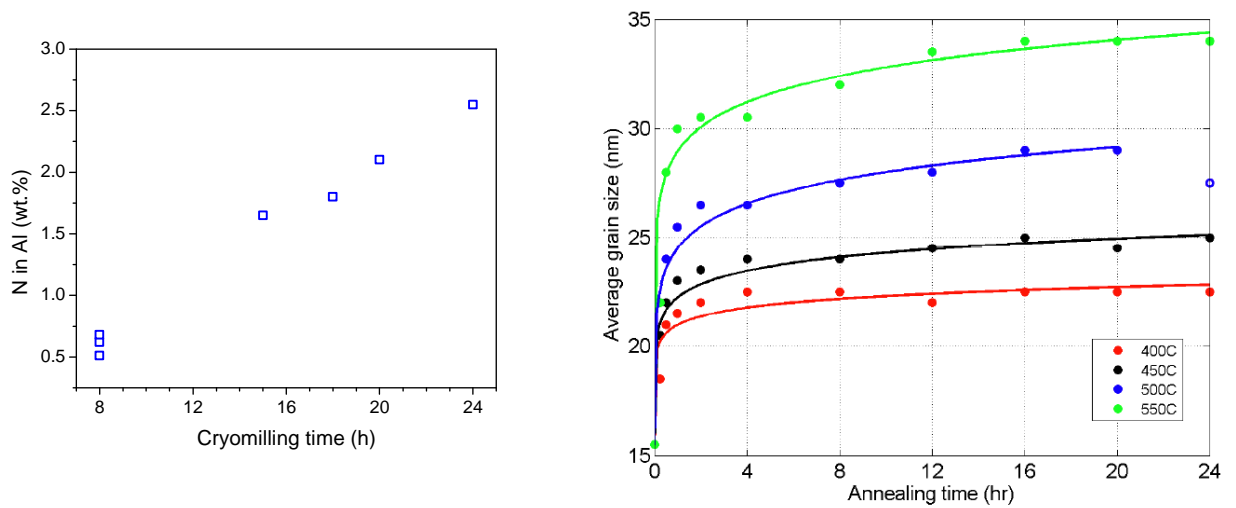


Figure 2. (a) Nitrogen content as a function of cryomilling time of Al 5083-14.3 wt.% B₄C composite powder [34]. (b) The grain size as a function of annealing time at different temperatures of Al 5083-14.3 wt.% B₄C composite powder cryomilled for 24 hours with liquid nitrogen [35].

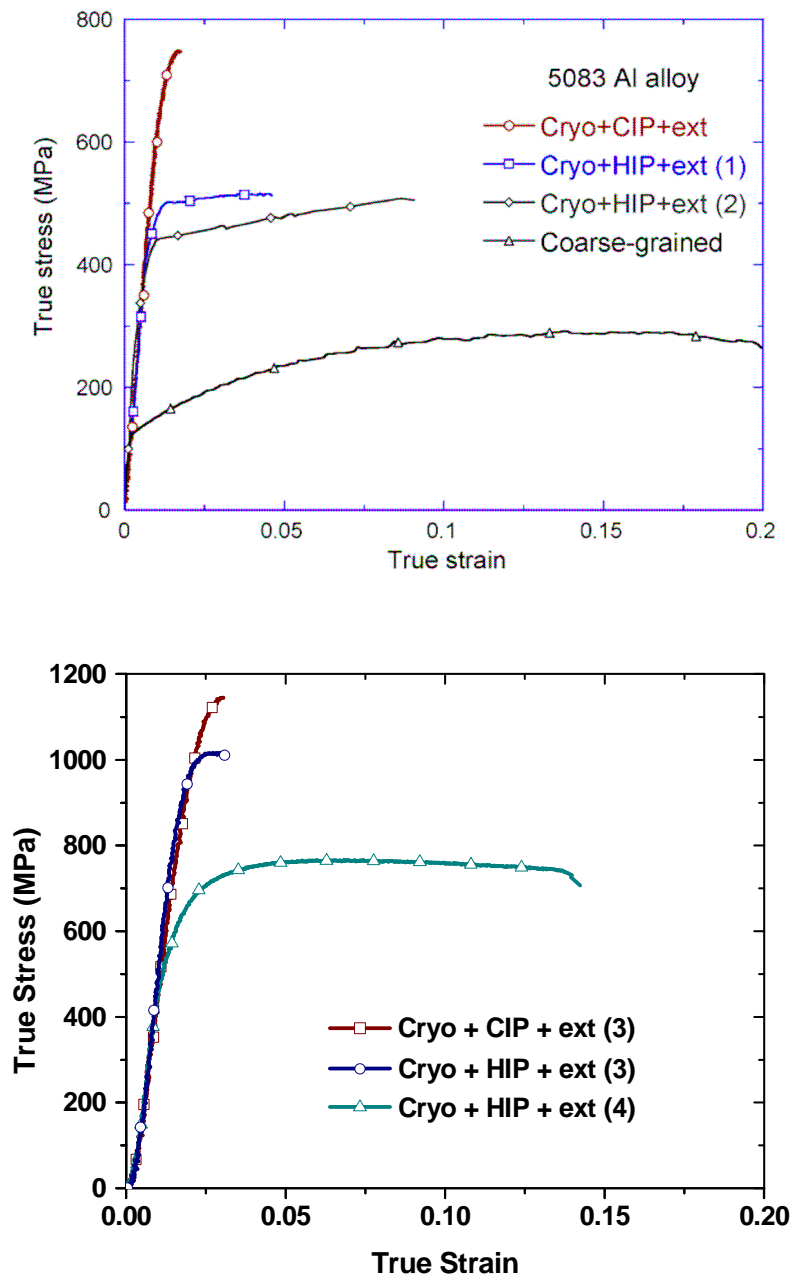


Figure 3. (a) True tensile stress as a function of true stain of cryomilled Al 5083 alloys [29]. (b) True compressive stress as a function of true strain of cryomilled Al 5083-10% B₄C-30% coarse-grained Al 5083 composites [34].

References

- [1] J.S. Benjamin, *Metallurgical Transactions A*, 1 (1970) 2943-2951.
- [2] C.C. Koch, *Nanostructured Materials*, 2 (1993) 109-129.
- [3] C.C. Koch, *Nanostructured Materials*, 9 (1997) 13-22.
- [4] H.J. Fecht, *Nanostructured Materials*, 6 (1995) 33-44.
- [5] C. Suryanarayana, *Progress in Materials Science*, 46 (2001) 1-184.
- [6] Z.H. Zhang, B.Q. Han, K.H. Chung, E.J. Lavernia, *Metallurgical and Materials Transactions A*, 37A (2006) 2265-2273.
- [7] M.J. Luton, C.S. Jayanth, M.M. Disko, S. Matras, J. Vallone, Cryomilling of nano-phase dispersion strengthened aluminum, in: *Mat. Res. Soc. Symp. Proc.*, 1989, pp. 79-86.
- [8] F. Zhou, J. Lee, E.J. Lavernia, *Scr. Mater.*, 44 (2001) 2013-2017.
- [9] R.J. Perez, H.G. Jiang, C.P. Dogan, E.J. Lavernia, *Metall. Mater. Trans.*, A29 (1998) 2469-2475.
- [10] B.J.M. Aikin, R.M. Dickerson, D.T. Jayne, *Scripta Metallurgica et Materialia*, 30 (1994) 119-122.
- [11] H. Gleiter, *Progress in Materials Science*, 33 (1989) 223-315.
- [12] Z. Budrovic, H. Van Swygenhoven, P.M. Derlet, S.V. Petegem, B. Schmitt, *Science*, 304 (2004) 273-276.
- [13] Y.M. Wang, M.W. Chen, F.H. Zhou, E. Ma, *Nature*, 419 (2002) 912-915.
- [14] Y.H. Zhao, T. Topping, J.F. Bingert, J.J. Thornton, A.M. Dangelewicz, Y. Li, W.S. Liu, Y.T. Zhu, Y.Z. Zhou, E.J. Lavernia, *Advanced Materials*, 20 (2008) 3028-3033.
- [15] V.L. Tellkamp, A. Melmed, E.J. Lavernia, *Metall. Mater. Trans. A*, 32 (2001) 2335-2343.
- [16] Y. Xiang, T. Li, Z.G. Suo, J.J. Vlassak, *Appl. Phys. Lett.*, 87 (2005).
- [17] T.H. Fang, W.L. Li, N.R. Tao, K. Lu, *Science*, (2011).
- [18] L. Lu, X. Chen, X. Huang, K. Lu, *Science*, 323 (2009) 607-610.
- [19] L. Lu, Y.F. Shen, X.H. Chen, L.H. Qian, K. Lu, *Science*, 304 (2004) 422-426.
- [20] Y.H. Zhao, J.F. Bingert, X.Z. Liao, B.Z. Cui, K. Han, A. Serhueva, A.K. Mukherjee, R.Z. Valiev, T.G. Langdon, Y.T. Zhu, *Advanced Materials*, 18 (2006) 2949-2953.
- [21] Y.H. Zhao, X.Z. Liao, S. Zheng, E. Ma, Y.T. Zhu, *Advanced Materials*, 18 (2006) 2280-2283.
- [22] G. He, J. Eckert, W. Loser, L. Schultz, *Nature Materials*, 2 (2003) 33-37.
- [23] K.X. Tao, H. Choo, H.Q. Li, B. Clausen, J.E. Jin, Y.K. Lee, *Applied Physics Letters*, 90 (2007).
- [24] Y.H. Zhao, J.F. Bingert, Y.T. Zhu, X.Z. Liao, R.Z. Valiev, Z. Horita, T.G. Langdon, Y.Z. Zhou, E.J. Lavernia, *Applied Physics Letters*, 92 (2008) 081903.
- [25] P.V. Liddicoat, X.Z. Liao, Y.H. Zhao, Y.T. Zhu, M.Y. Murashkin, E.J. Lavernia, R.Z. Valiev, S.P. Ringer, *Nat. Commun.*, 1 (2010).
- [26] F. Zhou, X.Z. Liao, Y.T. Zhu, S. Dallek, E.J. Lavernia, *Acta Mater.*, 51 (2003) 2777-2791.
- [27] X.Z. Liao, J.Y. Huang, Y.T. Zhu, F. Zhou, E.J. Lavernia, *Philos. Mag.*, 83 (2003) 3065-3075.
- [28] B.Q. Han, Z. Lee, D. Witkin, S. Nutt, E.J. Lavernia, *Metall. Mater. Trans. A*, 36A (2005) 957-965.
- [29] E.J. Lavernia, B.Q. Han, J.M. Schoenung, *Mater. Sci. Eng. A*, 493 (2008) 207-214.
- [30] S.Y. Chang, J.G. Lee, K.T. Park, D.H. Shin, *Mater. Trans.*, 42 (2001) 1074-1080.
- [31] J. Ye, B.Q. Han, Z. Lee, B. Ahn, S.R. Nutt, J.M. Schoenung, *Scr. Mater.*, 53 (2005) 481-486.
- [32] S.P. Joshi, K.T. Ramesh, *Scr. Mater.*, 57 (2007) 877-880.
- [33] J. Ye, Z. Lee, B. Ahn, J. He, S.R. Nutt, J.M. Schoenung, *Metall. Mater. Trans. A*, 37A (2006) 3111-3117.
- [34] R. Vogt, in: *Chemical Engineering and Materials Science*, University of California, Davis, 2010.
- [35] L. Hashemi-Sadraei, S.E. Mousavi, R. Vogt, Y. Li, Z. Zhang, E.J. Laverna, J.M. Schoenung, *Metallurgical and Materials Transactions A*, (2011) accepted.

RESIDUAL STRESSES DURING DEFORMATION OF NANOCRYSTALLINE METALS : IN-SITU XRAY DIFFRACTION AND SIMULATIONS

H. Van Swygenhoven^{1,2} and S. Van Petegem¹

¹ Paul Scherrer Institut, CH-5232 Villigen, Switzerland

² Ecole Polytechnique Fédérale de Lausanne, CH-1015 Lausanne, Switzerland

Abstract. Combining in-situ mechanical testing during x-ray diffraction and insights from computer simulations suggest that in nanocrystalline metals the built-up of residual stresses is suppressed compared to what is typically observed for coarse-grained materials. The results stress the importance of the initial stress state of nanocrystalline materials and of the heterogeneity of the microstructure at the nanoscale.

1. INTRODUCTION

Nanocrystalline (nc) metals have been the focus of numerous experimental and theoretical studies in the past two decades. With respect to the mechanical properties it is well known that nanocrystalline metals exhibit increased strength and strain rate sensitivity compared to their coarse-grained counterparts [6],[7],[8]. The mechanisms responsible for these enhanced properties are still under debate. It is generally accepted that when the grain size is reduced below 100nm, dislocation sources inside the grains become scarce and dislocation pile-ups are largely reduced. On the other hand, grain boundaries (GB) start playing a more prominent role, acting for instance as both sources and sinks for dislocations in a single dislocation regime [9],[10],[11],[12]. Such a role for GBs has been suggested by molecular dynamics simulations (MD) [13],[14],[15].

In-situ X-ray diffraction in nc-Ni has revealed the reversibility of diffraction peak broadening during plastic deformation, demonstrating the lack of a permanent residual dislocation network after deformation [16],[17],[18]. Stress-reduction experiments on nc-Ni showed that the long-range (athermal) and short-range (thermal) stresses for dislocation propagation are both large [19], supporting the hypothesis that dislocation propagation is hindered by grain boundary pinning [20],[21],[22]. For even smaller grain sizes a transition from dislocation-mediated plasticity to pure grain boundary accommodation mechanism is to be expected [7] and the role of shear banding [23] mechanism such as coupled GB motion are discussed [24].

This work reports on in-situ mechanical testing during x-ray diffraction of nanocrystalline Ni. It is shown the built-up of residual stresses is suppressed compared to what usually observed for coarse-grained metals. The results are interpreted with the help of molecular dynamics and quantized plasticity simulations.

2. EXPERIMENTAL

The material under investigation is nanocrystalline Ni synthesized by pulsed electro-deposition. It has a number-averaged grain size of 26nm and a mild {100} out-of-plane texture. Impurities mainly consist of Sulphur (500ppm) and some Fe, Cu and Co (less than 200ppm).

Uniaxial tensile tests were performed on 3mm dogbone-shaped specimens with a cross-section of 200×200μm². The specimens were cut by electro-discharge machining (EDM). After EDM, the samples were electrolytically polished to remove any damaged layer caused by the spark erosion process. The applied strain was measured directly by a high-resolution optical extensometer.

In-situ mechanical testing during x-ray diffraction was performed at the powder diffraction station of the Materials Science Beamline at the Swiss Light Source (SLS). The diffracted beam is recorded by a one-dimensional position-sensitive multistrip detector with an angular resolution of 0.0039° . This setup allows measuring X-ray diffraction patterns spanning 120° continuously during straining of the specimens. Typical acquisition times for one full diffraction spectrum range between 1s and 10s. All diffraction peaks could be fitted satisfactory with a split Pearson VII function yielding the peak position, peak broadening (here described by the full-width at half-maximum - FWHM) and other parameters reflecting the peak shape. More details about the in situ setup and the analysis procedure can be found in ref [25].

3. RESULTS

3.1 Evolution lattice strain

Continuous tensile testing during x-ray diffraction was performed with a strain rate of 10^{-4} s^{-1} . Figure 1A displays the corresponding stress-strain relationship. Due to the applied stress the lattice spacing is changed, which is reflected by a peak movement. For a given crystallographic direction hkl the relation between peak position θ_{hkl} and lattice strain ε_{hkl} (in units of microstrain) is given by:

$$\varepsilon_{hkl} = -\cot(\theta_{hkl})\Delta\theta_{hkl} \times 10^6 \quad (1)$$

where $\Delta\theta_{hkl}$ represents the deviation of the peak position from the position before loading. Figure 1B represents the evolution of the lattice strain for the $\{111\}$, $\{200\}$, $\{220\}$ and $\{311\}$ grain families along the transverse direction. Multiple experiments were performed in order to verify the reproducibility of the results. The dashed lines in figure 1B represent linear fits for the data points recorded at stresses below 0.8GPa. The deviation between the data points and the linear fits is shown in figure 1C.

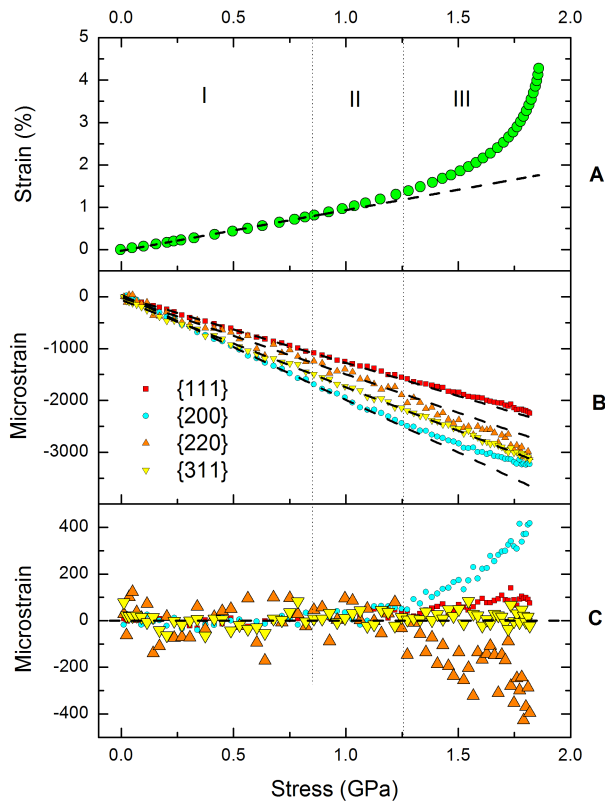


Figure 1. A) Stress-strain data for a continuous tensile test, B) corresponding evolution of the transverse elastic lattice strain for the $\{111\}$, $\{200\}$, $\{220\}$ and $\{311\}$ diffraction peaks. The dashed lines represent linear fits, C) deviation from linearity.

3.2 Evolution peak broadening

A series of in-situ load-unload cycles during x-ray diffraction have been performed. After each unload the sample is kept free of applied stress for 10min. Figure 2A displays the corresponding stress/strain data. Figure 2B shows the evolution of the FWHM of the {111} and {311} diffraction peak in the unloaded state. Note that in each unloaded state multiple diffraction patterns have been acquired. During this period the FWHM slightly decreases, in particular at plastic strains above 1%. This is due to relaxation effects that take place after unloading. Such relaxation effects have been observed before [18], [26]. In the early stages of plastic deformation the FWHM clearly decreases. This trend is reversed for plastic strains above 5%.

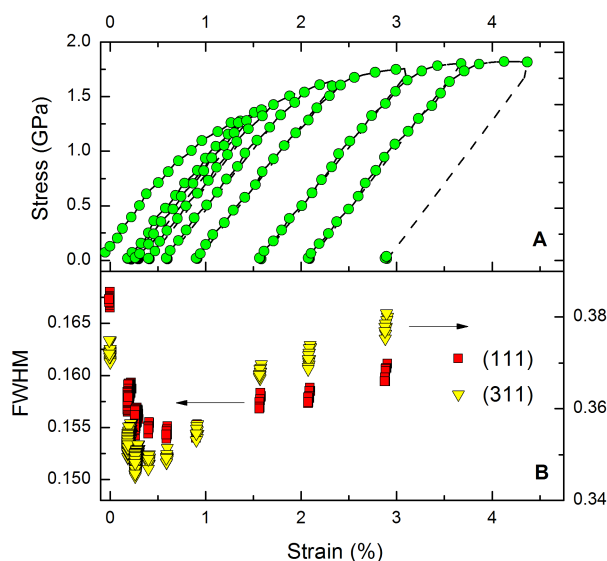


Figure 2. A) Stress-strain data of a series of load-unload cycles, B) corresponding evolution of the FWHM of the {111} and {311} diffraction peak after unloading.

4. DISCUSSION

Based on the observed evolution of the elastic lattice strain and peak broadening the stress-strain curve of nanocrystalline Ni may be divided into three parts: I-elastic, II-microplastic and III-macroplastic, as indicated on figure 1A. After the initial elastic regime a microplastic regime is present, during which the peak broadening decreases whereas the elastic lattice strain does not alter. After the microplastic regime, full plasticity sets in, characterized by a decreased strain hardening and changes in both elastic lattice strain and peak broadening. In what follows these two parameters are discussed in more detail.

4.1 Elastic lattice strain

It is well established that in coarse-grained anisotropic f.c.c. metals the elastic lattice strain along certain crystallographic directions divergences upon plastic deformation. This is linked to the built-up of intergranular stresses, which is the consequence of elastic and plastic anisotropy and corresponding load transfer between grain families [27].

Recently it was suggested that upon plastic deformation of some nanocrystalline metals intergranular stresses do not change, or are at least significantly lower compared to what is observed for coarse-grained materials [28], [29], 0. This may be interpreted as evidence for the presence of grain boundary processes, such as grain boundary sliding, at the expense of intra-granular slip.

The results shown in figure 1C provide similar results; in the microplastic regime there is little built-up of intergranular stresses. Also in the macroplastic regime magnitude of the intergranular strain is relatively low compared to what is observed for coarse-grained Ni. In order to understand this behaviour quantized crystal plasticity (QCP) modelling has been performed. The details of the model can be found at Ref [31]. QCP is

based on two main principles: i) at the nanoscale slip is quantized; when a dislocation travels from one GB to another a local shear strain of the order of b/d is produced, where b is the burgers vector and d the grain diameter. This is accompanied by a large stress relief [32]. ii) There exists a broad, spatially non-uniform, asymmetric distribution of critical stresses to activate slip. This is justified by the heterogeneous nature of the microstructure of nanocrystalline metals (grain size distribution, nature of GBs, nature of dislocation nucleation sites, GB obstacle strengths, etc.). Given these assumptions the model predicts for a given amount of plastic strain decreasing values for inter-granular strains with decreasing grain diameter. This can be rationalized by considering that at the nanoscale the role of the Schmid factor is reduced. Indeed, for large-grained materials with a relatively narrow distribution of critical stresses the slip distribution in the material is predominantly determined by the grain orientation distribution. This naturally leads to load transfer from 'soft' grain families to 'hard' grain families [27]. At the nanoscale the effect of the grain orientation distribution is reduced; it is now the distribution of critical stresses that allows for large load transfers between grains within the same grain family (in particular at small deformation), thereby averaging out load transfer between grain families.

4.2 Peak broadening.

There are several possible reasons for the initial decrease of peak broadening in the microplastic regime. In some nanocrystalline metals stress-induced grain growth has been observed, which would lead to such a decrease in peak broadening. However, it is well-known that electrodeposited Ni is very stable against grain growth. This has been established recently by extensive electron microscopy investigations [28].

Part of the peak broadening is due to the distribution of different stress levels in grains with a given grain family. The initial decrease may therefore be related to a narrowing of this distribution. It can be anticipated that grains with high initial stress levels yield early, thereby causing large stress-relief in these grains and their surroundings.

Finally a decrease of the peak broadening may be related to a decrease of elastic inhomogeneous strains within the grain interiors. Such inhomogeneous strains can originate from, for instance, dislocations and stress concentrations at GBs.

In coarse-grained metals an increase of the peak broadening upon plastic deformation is expected because of an increase in dislocation density. For the case of nc Ni only a mild increase of the peak broadening is observed. Most likely this increase is related to an increase in the density of GB stress concentrations. They originate from dislocations that have been absorbed by GBs. This is confirmed with the help of molecular dynamics (MD) simulations: diffraction patterns calculated from deformed nanocrystalline MD configurations suggest that stress concentrations at GBs have similar x-ray diffraction footprints compared to lattice dislocations inside grain interiors. This explains why, for instance, the {311} diffraction peak exhibits a larger increase in peak broadening compared to the {111} diffraction peak [20].

5. CONCLUSIONS

In-situ mechanical during x-ray diffraction allows studying the evolving microstructure during deformation. For nanocrystalline Ni it is found that the built-up of residual stress is suppressed compared to what is usually found for large-grained f.c.c metals. By using molecular dynamics and quantized crystal plasticity simulations it is shown that this is an expected result, and is therefore not necessarily linked to transition from intra-granular slip to grain boundary mediated mechanisms.

Acknowledgments

The authors acknowledge the help of J. Zimmermann and M. Weisser. The QCP simulations were performed by L. Lin and P.A. Anderson. HVS thanks the Swiss National Science Foundation of financial support.

References

- [6] K.S. Kumar, H. Van Swygenhoven, S. Suresh, *Acta Mater.* 51 (2003) 5743.
- [7] M.A. Meyers, A. Mishra, D.J. Benson, *Prog. Mater. Sci.* 51 (2006) 427.
- [8] R.J. Asaro, S. Suresh, *Acta Mater.* 53 (2005) 3369.
- [9] K.S. Kumar, S. Suresh, M.F. Chisholm, J.A. Horton, P. Wang, *Acta Mater.* 51 (2003) 387.
- [10] R.C. Hugo, H. Kung, J.R. Weertman, R. Mitra, J.A. Knapp, D.M. Follstaedt, *Acta Mater.* 51 (2003) 1937.
- [11] M.W. Chen, E. Ma, K.J. Hemker, H.W. Sheng, Y.M. Wang, X.M. Cheng, *Science* 300 (2003) 1275.
- [12] L. Wang, E. Zhang, E. Ma, X.D. Han, *Appl. Phys. Lett.* 98 (2011) 051905.
- [13] H. Van Swygenhoven, P.M. Derlet, A.G. Froseth, *Acta Mater.* 54 (2006) 1975.
- [14] H. Van Swygenhoven, P.M. Derlet, A. Hasnaoui, *Phys. Rev. B* 66 (2002) 8.
- [15] H. Van Swygenhoven, P.M. Derlet, A.G. Froseth, *Nat. Mater.* 3 (2004) 399.
- [16] Z. Budrovic, H. Van Swygenhoven, P.M. Derlet, S. Van Petegem, B. Schmitt, *Science* 304 (2004) 273.
- [17] Z. Budrovic, S. Van Petegem, P.M. Derlet, B. Schmitt, H. Van Swygenhoven, E. Schafner, M. Zehetbauer, *Appl. Phys. Lett.* 86 (2005) 231910.
- [18] S. Brandstetter, H. Van Swygenhoven, S. Van Petegem, B. Schmitt, R. Maass, P.M. Derlet, *Adv. Mater.* 18 (2006) 1545.
- [19] S. Van Petegem, S. Brandstetter, H. Van Swygenhoven, J.L. Martin, *Appl. Phys. Lett.* 89 (2006) 073102.
- [20] S. Brandstetter, P.M. Derlet, S. Van Petegem, H. Van Swygenhoven, *Acta Mater.* 56 (2008) 165.
- [21] S. Brandstetter, Z. Budrovic, S. Van Petegem, B. Schmitt, E. Stergar, P.M. Derlet, H. Van Swygenhoven, *Appl. Phys. Lett.* 87 (2005) 231910.
- [22] S. Van Petegem, S. Brandstetter, B. Schmitt, H. Van Swygenhoven, *Scripta Mater.* 60 (2009) 297.
- [23] J.R. Trelewicz, C.A. Schuh, *Acta Mater.* 55 (2007) 5948.
- [24] T.J. Rupert, D.S. Gianola, Y. Gan, K.J. Hemker, *Science* 326 (2009) 1686.
- [25] H. Van Swygenhoven, B. Schmitt, P.M. Derlet, S. Van Petegem, A. Cervellino, Z. Budrovic, S. Brandstetter, A. Bollhalder, M. Schild, *Rev. Sci. Instr.* 77 (2006) 013902.
- [26] J. Rajagopalan, J.H. Han, M.T. Saif, *Science* 30 (2007) 1831.
- [27] B. Clausen, T. Lorentzen, T. Leffers, *Acta Mater.* 46 (1998) 3087
- [28] H. Q. Li, H. Choo, Y. Ren, T. A. Saleh, U. Lienert, P.K. Liaw, F. Ebrahimi, *Phys. Rev. Lett.* 101 (2008) 015502.
- [29] Y. M. Wang, R.T. Ott, A.V. Hamza, M.F. Besser, J. Almer, M.J. Kramer, *Phys. Rev. Lett.* 105 (2010) 215502.
- [30] S. Cheng, A.D. Stoica, X.-L. Wang, Y. Ren, J. Almer, J.A. Horton, C.T. Liu, B. Clausen, D.W. Brown, P.K. Liaw, L. Zuo, *Phys. Rev. Lett.* 103 (2009) 035502.
- [31] L. Li, P.M. Anderson, M.G. Lee, E. Bitzek, P.M. Derlet, H. Van Swygenhoven, *Acta Mater* 57 (2009) 812.
- [32] E. Bitzek, P.M. Derlet, P.M. Anderson, H. Van Swygenhoven, *Acta Mater.* 56 (2008) 4846.
- [33] S. Brandstetter, K. Zhang, A. Escudero, J.R. Weertman, H. Van Swygenhoven, *Scripta Mater* 58 (2008) 61.

IMPERFECTION, RATE AND SIZE DEPENDENT PLASTIC LOCALIZATION IN THIN NANOCRYSTALLINE METALLIC FILMS

T. Pardoen^{1,3}, M. Coulibier^{1,3}, M.S. Colla^{1,2}, H. Idrissi⁴, B. Wang⁴, D. Schryvers⁵, and J.P. Raskin^{2,3}

¹*Institute of Mechanics, Materials and Civil Engineering,*

Université catholique de Louvain, Place Sainte Barbe 2, B-1348 Louvain-la-Neuve, Belgium

²*Information and Communication Technologies, Electronics and Applied Mathematic*

Université catholique de Louvain, B-1348 Louvain-la-Neuve, Belgium

³*CeRMiN, Research Center in Micro and Nanoscopic Materials and Electronic Devices, Université catholique de Louvain, B-1348 Louvain-la-Neuve, Belgium*

⁵*EMAT, University of Antwerp, Groenenborgerlaan 171, 2020 Antwerpen, Belgium*

The resistance of thin metallic films to plastic localization is an important issue in flexible electronics, thin coatings on deformable substrates, and several types of MEMS. From a fundamental perspective, thin metallic films often involve nanocrystalline structures which can be easily modified by changing the deposition parameters, offering a wide range of possibilities to study interface dominated plastic deformation mechanisms in nanostructured systems. The resistance to plastic localization is controlled by the strain hardening, strain rate sensitivity, and presence of imperfections. Experimental results obtained using a nanomechanical lab-on-chip technique on Al, AlSi and Pd films with thickness between 50 and 500 nm show several types of size effects affecting the ductility. The Al films, with ~200 nm grain size, demonstrate moderate strain hardening capacity, significant rate sensitivity and an accumulation of dislocations inside the grains. The Pd films involve ~30 nm grain size containing a high density of fine coherent ~2 nm thick growth twins offering multiple barriers to dislocation motion, and sources for dislocation storage and multiplication. The very high strain hardening capacity coming from the dislocation/twin boundary interactions does not lead to large ductility due to failure mechanisms initiating after 2 to 4 % strain. A strong statistical dependence of the ductility on the overall size of the sample is also observed. An imperfection type localization analysis is performed to rationalize the different contributions to the resistance to plastic localization.

UPDATES ON AVANCED LAYERED PERSONNEL ARMOR

J. O. Sinibaldi, R. S. Hixson, J.R. Garner, J. Denzel and C. W. Ong

Department of Physics, Naval Postgraduate School, Monterey, CA 93943, USA

Abstract. Utilizing shock compression physics considerations and explicit numerical techniques an advanced composite system for personnel armor was developed.[1]This composite system is composed of 4 layers, which when put in a specific order, this composite armor has been shown experimentally to be more effective in resisting penetration than a steel plate of equivalent (and slightly greater) areal density. This design consists of a very hard 1st layer to deform and fracture the projectile, an orthotropic 2nd layer to slow down the shock wave propagation in the through thickness direction, whilst allowing rapid propagation in the transverse directions, a 3rd porous layer to absorb the shock wave energy through PV-work, and a 4th layer to provide confinement for the porous medium. This research provides updates on a very hard alumina (Al₂O₃) Ceramic layer, and a transversely isotropic layer composed of Dyneema HB25 fibers in a polyethylene matrix, that is the first and second layers, respectively. The alumina ceramic and Dyneema layers were subjected to dynamic experiments with planar shock inputs to provide high fidelity Hugoniot equations of state, and for alumina ceramic, also the Hugoniot elastic limit and the spall strength. In a shock speed versus particle velocity space (U_s-u_p), the Dyneema showed a nonlinear Hugoniot relationship in the through direction (perpendicular to the fiber direction) and was found to be: $U_s = -1.673u_p^2 + 4.847u_p + 0.902$. The alumina ceramic showed a linear Hugoniot relationship of: $U_s = 0.936u_p + 10.53$; with a Hugoniot elastic limit between 74.7 kbar and 90.7 kbar; and a spall strength of 2.71 kbar. Due to the low spall strength (less than 3 kbar) of alumina ceramic in comparison to its Hugoniot elastic limit (near 90 kbar), initial considerations for future work have been made for the use of glassy metals, ultra fine grain tungsten carbide in Cobalt matrix ceramics, and other high strength ductile materials.

1. INTRODUCTION

Utilizing shock compression physics considerations and explicit numerical techniques an advanced composite system for personnel armor was developed.This composite system is composed of 4 layers, which when put in a specific order, this composite armor has been shown experimentally to be more effective in resisting penetration than a steel plate of equivalent (and slightly greater) areal density.[1]

A description of the various projectile/armor and shockwave/armorinteractions during the impact process through the 4 layers is narrated below;followed by a conceptual sketch of this composite armor system – shown in Figure (1).

As the projectile impacts the **first layer**, the projectile should undergo plastic deformation. This is accomplished byselecting a high yield strength, high impedance material to resist penetration from compressiveforces as much as possible causing significant plastic deformationin the projectile. This layer also helps to decrease theimpulse delivered into subsequent layers. Previous work [1] selected an Alumina Ceramic (Al₂O₃) material, Corbit 98 (98% alumina), however due to the lack of fundamental dynamic material response data for Corbit 98, the hydrocodes simulations were performed with the material properties from a different alumina ceramic, “technical ceramic” with a 99.5% alumina content. Although the authors believe them to have similar behavior, obtaining the exact dynamic response for Corbit 98 would increase the fidelity of hydrocodes simulations and provide avenues for the improvement of this armor concept through optimization studies.

The **second layer** is the wave-spreading layer that uses special orthotropic composites,with a sound speed ratio as high as possible of its lateral to axial longitudinal sound speeds. This provides the mechanism necessary to spread shockwaves laterally away from the incident axis. Thus causing significantstress wave attenuation.Previous work selected Dyneema HB25 material as the orthotropic wave-spreading layer material. Dyneema is an ultra-high-molecular weight polyethylene fiber in a polyethylene matrix. Due to a lack of data

in the literature on the dynamic response of Dyneema, the authors had previously deduced appropriate estimates for the Dyneema material properties from careful literature studies of similar fiber based materials. It is believed that the discrepancies between experimental data and simulations in previous work [1] can be substantially improved by obtaining the specific dynamic response properties for Dyneema HB25. Further work utilizing the exact material properties, could easily yield a much better optimized armor concept.

The **third layer** functions as the energy absorption mechanism, which utilizes porous materials to convert kinetic energy into waste heat through PV-work done during the compression of the pores within these types of materials. Previous work utilized two different polyurethane foams, which provided sufficient evidence to verify the predicted effects of this energy absorption mechanism. Future work will concentrate on the selection of optimum materials for this layer.

The **fourth layer** is the final stopping layer to prevent penetration of projectiles with nominal velocities. Through impedance matching, this layer also provides prevention against spall for the porous layer. Previous work selected an aluminum plate for its ductility, strength, and low density to keep a favorable overall areal density. However, it is expected that much lighter and better impedance matching materials can be selected.

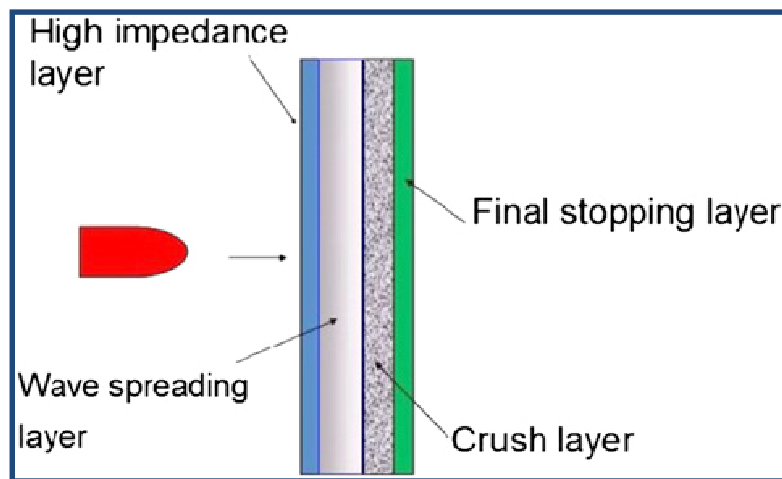


Figure 1. Schematic of the proposed composite armor system.

1.1. Goals and Objectives

The motivation for this study was to provide an avenue to advance and optimize this multi-layered armor concept. This was accomplished by performing fundamental studies of the dynamic response of materials for the High strength, high impedance layer and for the wave spreading orthotropic material layer, the first and second layers, respectively.

Therefore, the focus of this work was on the fundamental experiments that were required to obtain a) the Hugoniot for Corbit 98, along with its Hugoniot elastic limit (HEL) and its spall strength; and b) the Hugoniot for Dyneema HB25. Brief considerations for potential alternative materials for these first two layers are briefly discussed.

1.2. Technical Approach

In order to properly understand the dynamic response of these two materials, Corbit 98 and Dyneema HB25, a careful characterization of the initial condition of these materials is necessary. This was followed by a set of dynamic experiments designed to simplify the theoretical manipulation of the complex multi-dimensional equations by putting the materials under uni-axial strain conditions – by using planar shock experiments. Thus, by combining the theories from conservation laws (mass, momentum and energy) and elasticity, with the fundamental characterizations and the particle velocity measurements during dynamic experiments, we were able to obtain the desired Hugoniot, elastic limit, and spall strength measurements.

2. THEORY

All materials respond dynamically to the impulsive loading imparted to them during a dynamic event, such as armor being impacted by small arms fire, in a way that is governed by their inherent properties. Dynamic deformations follow physical processes that are governed by the laws of physics and materials science. Thus, in order to predict the behavior of these materials under dynamic impacts, one must understand that the propagation of shock waves in conjunction with the elastoplastic response of the materials are intertwined and one must take these into account. The theories behind such responses are not new and can be accessed in many well written works by Kolsky, Meyers and I am sure others [2,3], however it will be beneficial to extract key results and present those herein to illustrate the required design of experiments as well as the required treatise of the data recorded. We first cover the aspects of isotropic materials due to their much simpler and elegant solutions when compared to more complex materials. This represents the behavior of Corbit-98 ceramic. A following section deals with orthotropic materials that will be used to understand the behavior of Dyneema.

2.1. Isotropic materials

When a material is loaded under a stress, it responds by contracting or expanding, depending on whether the stress applied puts the material in compression or in tension, respectively. Therefore, the material strain is proportional to the stress loading. The relationship between stress and strain in the linear elastic region is characterized by a constant known as the Young's modulus, E , and is given as the ratio of stress over strain. Young's modulus is a fundamental modulus for states of *uniaxial stress*. Once a material reaches the limit for linear response it begins to transition from elastic to plastic deformation. Strain that occurs as a result of plastic deformation is unrecoverable, and so by definition not elastic. The region of plastic deformation is an important region for the materials involved in this research. Since in armor applications materials are subjected to high velocity projectile impacts, where considerable plastic deformations are involved. However, the elastic deformation regime is also important for impact problems. In the elastic regime, the stresses and strains are related through the general constitutive relation, which consists of 36 independent constants. However, for isotropic materials the constitutive relations are much simpler reducing down to 12 constants that are composed of only 2 independent parameters – the Lamé constants, λ and μ . The Lamé constants are specific to each material and can be found by measuring the longitudinal, C_L , and shear, C_S , sound speeds which are then used to determine the bulk sound speed, C_B :

$$C_L = \sqrt{\frac{\lambda + 2\mu}{\rho_0}}, \quad C_S = \sqrt{\frac{\mu}{\rho_0}} \quad \text{and} \quad C_B = \sqrt{C_L^2 - \frac{4}{3}C_S^2}$$

Similarly, the various elastic moduli can be expressed in terms of the 2 Lamé constants as follows:

$$E = \mu \frac{3\lambda + 2\mu}{\lambda + \mu}, \quad G = \mu, \quad K = \lambda + \frac{2}{3}\mu, \quad \text{and} \quad F = \lambda + 2\mu$$

Where E , G , K , and F are the Young's, Shear, Bulk, and Longitudinal moduli, respectively. Another quantity of importance is the Poisson's ratio, ν , which indicates the relative compressibility of the material. This can also be defined in terms of the Lamé constants:

$$\nu = \frac{\lambda}{2(\lambda + \mu)}$$

If a sufficient number of these parameters are known, a material model can then be developed to accurately predict the response of materials under different loading conditions.

Once it is understood how a material will respond to a static load, the next logical step is to demonstrate the response of the material due to a dynamic load, specifically for shock wave loading conditions. If one sets up the experiment to be performed using planar impact geometry, the degrees of freedom of the problem become reduced. It can be assumed that all volume changes occur in a single direction and therefore the problem yields itself to a uniaxial strain loading analysis.

2.2. Orthotropic materials.

In a similar manner we can simplify the general anisotropic stiffness matrix for orthotropic materials and obtain the following constitutive relations:

$$\begin{bmatrix} \sigma_{xx} \\ \sigma_{yy} \\ \sigma_{zz} \\ \sigma_{yz} \\ \sigma_{zx} \\ \sigma_{xy} \end{bmatrix} = \begin{bmatrix} \frac{1-v_{yz}v_{zy}}{E_y E_z \Delta} & \frac{v_{yx}+v_{zx}v_{yz}}{E_y E_z \Delta} & \frac{v_{zx}+v_{yx}v_{zy}}{E_y E_z \Delta} & 0 & 0 & 0 \\ \frac{v_{xy}+v_{xz}v_{zy}}{E_z E_x \Delta} & \frac{1-v_{zx}v_{xz}}{E_z E_x \Delta} & \frac{v_{zy}+v_{zx}v_{xy}}{E_z E_x \Delta} & 0 & 0 & 0 \\ \frac{v_{xz}+v_{xy}v_{yz}}{E_x E_y \Delta} & \frac{v_{yz}+v_{xz}v_{yx}}{E_x E_y \Delta} & \frac{1-v_{xy}v_{yx}}{E_x E_y \Delta} & 0 & 0 & 0 \\ 0 & 0 & 0 & 2G_{yz} & 0 & 0 \\ 0 & 0 & 0 & 0 & 2G_{zx} & 0 \\ 0 & 0 & 0 & 0 & 0 & 2G_{xy} \end{bmatrix} \begin{bmatrix} \varepsilon_{xx} \\ \varepsilon_{yy} \\ \varepsilon_{zz} \\ \varepsilon_{yz} \\ \varepsilon_{zx} \\ \varepsilon_{xy} \end{bmatrix}$$

where,

$$\Delta = \frac{1-v_{xy}v_{yx}-v_{yz}v_{zy}-v_{zx}v_{xz}-2v_{xy}v_{yz}v_{zx}}{E_x E_y E_z}$$

But due to the symmetries of such orthotropic materials, the stiffness matrix must be symmetric about its diagonal and thus the number of independent parameters needed reduces further from the 12 shown above to 9 where the upper off-diagonal components are equal to the lower ones.

2.3. Dynamic Elastoplastic Theory

The physics at hand during a high-speed impact produce strain rates on the order of 10^6 to 10^8 s⁻¹. Therefore one must test the materials whose strength is most likely strain rate dependent at similar conditions. This can be performed with shock waves. Furthermore, the materials can be put under uniaxial strain loading conditions by using planar shocks. This allows a great theoretical simplification as will be shown here.

From the conservations laws of mass, momentum and energy across a shockwave we can come up with the relations called the *jump conditions* that allow us to “jump” from one side of a planar shock to the other. These relations are described below:

$$\text{mass: } \frac{\rho_0}{\rho} = 1 - \frac{u_p}{U_s}$$

$$\text{momentum: } P - P_0 = \rho_0 U_s u_p$$

$$\text{energy: } E - E_0 = \frac{1}{2}(P + P_0)(V_0 - V)$$

where P , V , and E represent the pressure, specific volume and specific energy; U_s and u_p represent the shock speed and particle velocity; and ρ represents the density. The subscript “0” indicates the material immediately ahead of the shock. No subscript represents the material properties immediately behind the shock.

By measuring certain key properties, and using these fundamental jump conditions for shock waves, one can develop an accurate equation of state (EOS) model for that material. The EOS contains fundamental thermodynamic information about the material that can be used to then predict how that material will respond to arbitrary shock compression. The EOS however, contains no information regarding the elastic-plastic response (dynamic strength) of the material.

Since we are using shock waves to compress the materials, measuring the material Hugoniot lends itself to these types of analyses. The Hugoniot curve is a locus of end states as materials are shock compressed. The Hugoniot is typically plotted in P - V space, P - u_p space or in U_s - u_p space. The latter is due to a linear relationship between U_s and u_p that is prevalent for most metals:

$$U_s = C_0 + Su_p$$

Here S is a constant that can be determined from a linear least-squares fit of the data. C_0 can be taken to be approximately equal to the bulk sound speed, C_B , at ambient conditions.

Since a planar shockwave puts a material under uniaxial strain conditions, for isotropic materials we can further reduce the stiffness matrix to a single component, and using the Lamé constants it becomes:

$$\sigma_x = (\lambda + 2\mu)\varepsilon_x$$

However in dynamic yielding experiments, the point at which this stress exceeds the dynamic elastic limit is called the Hugoniot Elastic Limit (HEL), σ_{HEL} . The HEL can be related to the yield stress, Y , through the young modulus and hooke's law as follows:

$$\sigma_{HEL} = Y \left(1 + \frac{\lambda}{2\mu} \right) = Y \left(\frac{1-\nu}{1-2\nu} \right)$$

This is very convenient to estimate the dynamic strength, the HEL, because most materials are readily characterized in a quasi-static uniaxial stress condition where the Yield stress and Poisson's ratio are measured.

3. EXPERIMENTAL SET-UP

3.1. Hugoniot Measurements

The generation of planar shockwaves for the dynamic characterization of these materials was accomplished through the use of a light-gas gun system to accelerate a flat plate to velocities up to 0.5 km/s. This flat plate would then impact the target material and at impact, the interface would suddenly have a discontinuity in particle velocities where two shock waves are generated. One shock is travelling into the target material and the other travels into the flyer plate. This resolves the problem of such discontinuity and provides new boundary conditions behind the shocks, where both the pressures and the particle velocities of both materials must be equal.

Figure (2b) shows a schematic of an x-t diagram that shows the conditions in both materials before and after the shock waves. Figure (2a) shows a schematic of the two plates impacting each other and also shows a VISAR probe, which how we measured the particle velocity. The piezoelectric pins are used to determine the onset of impact. This in conjunction with the onset of particle velocity data at the back of the target, indicates the time it took for the shock wave in the target to travel its thickness. Thus using a priori measurements of target thickness one can now calculate the shock speed. VISAR is an acronym for velocity interferometer system for any reflector, details on how it works can be found in Hemsing and Barker et al. papers [4, 5].

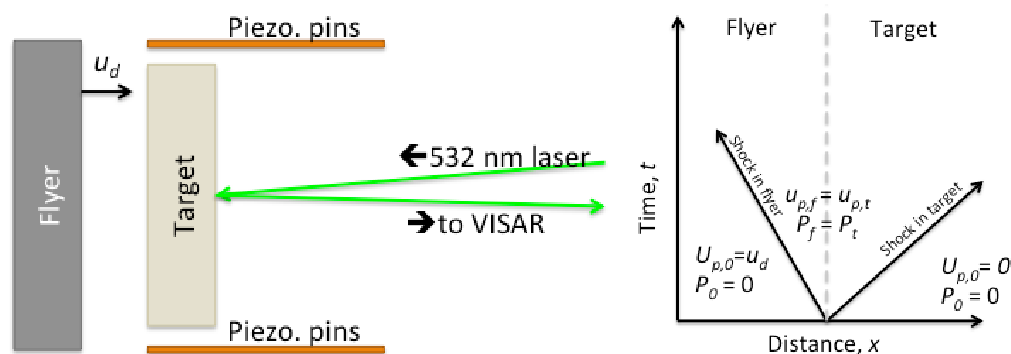


Figure 2. Schematic of a planar flyer plate impacting a planar target material and VISAR diagnostic probe; and x-t diagram of shock waves in flyer and target and their initial and boundary conditions.

These simple configurations allows to obtain various US uP pairs for different velocity impacts (u_d). Multiple experiments are required to construct a Hugoniot. In addition, during the uP measurements it is possible to

obtain a measurement of the HEL. Since at low speed impacts, a longitudinal shock wave will precede the plastic shock, one can easily distinguish such measurements in the VISAR record and obtain a particle velocity for the dynamic yield point. This in turn can be converted to stress and obtain the HEL:

$$\sigma_{HEL} = \rho_0 U_{Se} u_{P,HEL}$$

where $U_{S,e}$ is the elastic shock speed, and $u_{P,HEL}$ is the particle velocity behind the elastic shock.

3.2. Spall Strength Measurements

When measuring the spall strength (material strength in tension) one must design the experiments in such a way to make sure the target is put in tension by the intersection of two sets of release waves traveling in opposite directions. Selecting a flyer of about half the thickness of the target typically does this. A schematic of this concept is shown in Figure (3), an x-t diagram of the wave interactions.

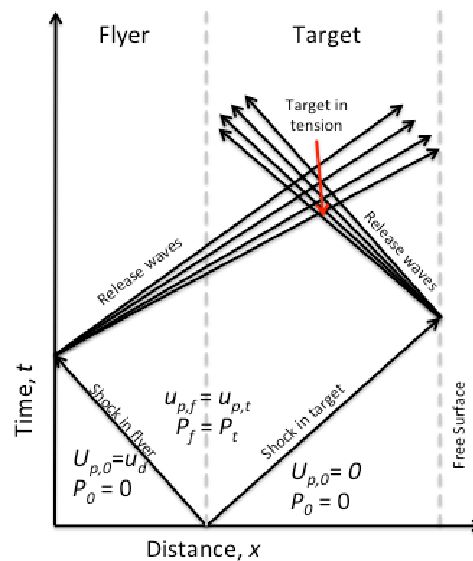


Figure 3. x-t diagram schematic for a spall measurement experiment.

From Figure (2) one can see that the VISAR is measuring the particle velocity at the free surface of the target. From t_0 to t_2 the VISAR should read zero velocity, from t_2 to t_4 the VISAR will read the velocity behind the shock wave at the free surface and immediately after t_4 , the velocity will drop up to some minimum at which time the particle velocity will suddenly increase again. If this is observed, one can determine that the material has failed under tension. Had the material been able to support these tensile forces, the release waves would have driven the particle velocity all the way down to zero.

We can now calculate the material strength under tension, however one must be careful to realize that the VISAR is measuring the free surface particle velocity, which is exactly twice the particle velocity behind the shock. Therefore a 0.5 factor must be included in the data analysis to get the true u_p and not the u_{fs} :

$$\sigma_{spall} = \frac{1}{2} \rho_0 U_x \Delta u_{fs}$$

where u_{fs} is the free surface velocity measured by the VISAR, the $\frac{1}{2}$ term is used to convert from free surface velocity to in-material particle velocity, and U_x is taken to be the elastic sound speed if the material is under the yielding point, or it is taken to be the bulk sound speed if the material is in its plastic states.

3.3. Other Material Characterization at Ambient Conditions

Other important material characterizations were needed to obtain all the parameters required to solve for σ_{HEL} , σ_{spall} , P , V , etc... Specifically these are the density, and the longitudinal and shear sound speeds - ρ_0 , C_L and C_S , respectively.

The initial density, ρ_0 , was measured by the Archimedean immersion technique, which carefully measures the volume of the liquid displaced by the target samples and the weight of the target dry and submerged in liquid.

The longitudinal and shear sound speeds, C_L and C_S , were measured by the echo sounding technique, where a perpendicular ultrasonic transducer is placed on top of the sample and is connected to a high-speed oscilloscope. This transducer sends a pulse into the target sample and the reflecting sound waves are recorded on the oscilloscope. Typically 7 to 15 reflections were recorded. The time between them was extracted and using a linear least-squares fit a time of flight can be obtained. The target thickness measurements are used to determine the path length of these sound waves and a simple division of distance over time elapsed is used to obtain the longitudinal sound speed. Similarly for the shear sound speed, a transverse ultrasonic transducer is mounted on the target and the reflection of these shear waves is recorded on an oscilloscope.

4. RESULTS AND DISCUSSION

4.1. Corbit 98 Ceramic (98% Al_2O_3)

Corbit 98 was selected for the first layer of our armor concept due to the high yield strength of ceramics, it's intended to produce substantial plastic deformation into the projectile threats. The Corbit 98 samples were ground to 50mm diameter with a nominal thickness of about 6.4mm. They were lapped on a diamond impregnated flat to reach very flat, parallel surfaces. The flyer plates were made of Z-cut sapphire due to its high yield point. Such is required to simplify the reflected waves from having reflected release waves from both the elastic and plastic shocks. Longitudinal and shear sound speeds and initial density measurements for this material are listed in table 1:

Table 1. Physical properties of Corbit 98 and other alumina ceramics of similar densities.

Material	Longitudinal C_L (km/s)	Sound Speed	Shear C_S (km/s)	Density ρ_0 (g/cc)
Corbit 98	10.549 ± 0.016		6.159 ± 0.021	3.864 ± 0.005
Al-995 [6]	10.34		6.21	3.81
Hot Pressed [6]	10.59		6.17	3.92
AD-995 [7]	10.56		6.24	3.89

Our material compares very favorably with hot-pressed ceramic as described by Gust and Royce [6], and the Coors AD-995 material measured by Grady [7] and Reinhart [8].

Six shots were completed for Corbit-98. Two of these shots were also used to measure spall strength, the other four shots had a Z-cut sapphire window in the back of the target to start to measure sound speeds at pressure in Corbit 98. However that will be the topic of a future endeavor. The results from our measurements of u_d , U_s , u_p , P (same as σ_x), σ_{HEL} , and σ_{spall} are tabulated below in Table (2) and plotted graphically in Figure (4).

Table 2. Corbit 98 experimental test matrix and summary of results.

Shot No.	Impact Velocity (km/s)	Shock Speed (km/s)	Particle Velocity (km/s)	Pressure (kbar)	Hugoniot Elastic Limit (kbar)	Spall Strength (kbar)
NPS10-3*	0.242	10.68	0.121	49.6	n/a	signal loss
NPS10-5	0.199	10.60	0.054	22.1	n/a	n/a
NPS10-6	0.191	10.59	0.051	20.9	n/a	n/a
NPS10-7	0.306	10.59	0.161	65.7	n/a	n/a
LANL1	0.796	10.34	0.426	170.3	79.6 ± 15	n/a
LANL2*	0.480	10.806	0.243	101.5	82.7 ± 8	2.71

*Tests performed with a free surface behind the target aimed to obtain spall strength data.

The progression of these tests shows an interesting trend that it was initially hard to comprehend. If we pay attention to shock speed, U_s , as a function of flyer impact speed, u_d . The data shows that as u_d is decreased from 0.242 to 0.191 km/s the U_s decreases from 10.68 to 10.59 km/s as expected. However, on shot NPS10-7, the impact speed was increased to 0.306 km/s but the shock speed measured remained at the low point of 10.59 km/s. To achieve higher impact velocities, a higher performance gun was needed and the following shots were

performed at Los Alamos National Laboratory. At which point a very fast impact speed was chosen with u_d of 0.796 km/s. To our surprise, the shock speed measured dropped even lower to a velocity of 10.34 km/s. At this time, our research team was somewhat perplexed and we started to compare our data with other data of similar alumina ceramics available in the literature. We knew that other physics were starting to take over for these numbers to make sense, and once we plotted our data along with the data from Grady et al., and Reinhart et al., we saw it clearly. It appears that at particle velocities between 0.15 and 0.5 km/s the material starts to yield and transitions from its elastic response to its plastic response. Thus a final shot was requested from Los Alamos high performance gun at an intermediate impact velocity value of 0.48 km/s to try to narrow down the elastic-plastic transition point more closely. This impact velocity produced the highest shock speed obtained of 10.806 km/s confirming our understanding of the behavior represented by the data.

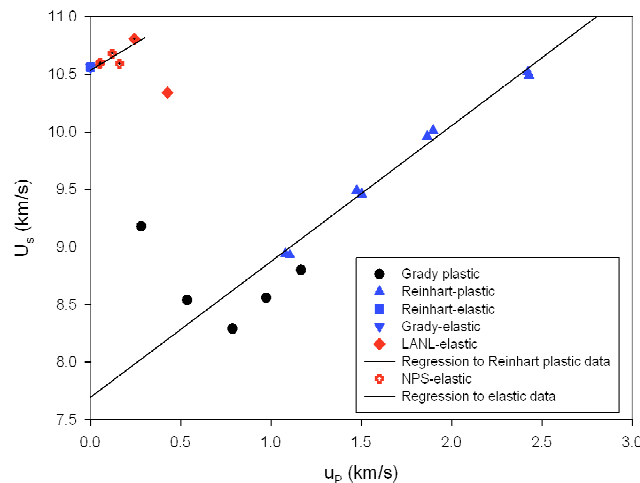


Figure 4. Hugoniot plot for Corbit 98 and comparison with similar alumina ceramics from Grady et al., and Reinhart et al.

The alumina ceramic showed in the elastic range a linear Hugoniot relationship of: $U_s = 0.936u_p + 10.53$. Particle velocity and shock pressures tracked linearly with impact velocity. Due to the use of the high performance gas gun at Los Alamos, the shock pressures reached exceeded the yielding point of Corbit 98 and the Hugoniot Elastic Limit was measured on both shots. An average value of 81.2 kbar was determined to be the HEL for Corbit 98.

With regards to Spall measurements, at NPS, a 4 to 8 micron thick aluminum foil was attached to the back side of the Corbit 98 target in shot NPS10-3. However soon after the shock pressure was reached, the VISAR system lost signal amplitude and the release information was not acquired. This was most probably due to either delamination of the aluminum foil (which was attached using Angstrom Bond epoxy) or due to the porosity of alumina ceramics, micro-jets on the ceramic could have easily damaged the reflecting surface (the aluminum foil) as the shock wave exited the ceramic, causing a loss in the reflection signal needed by the VISAR interferometer. A second attempt at these measurements was made at Los Alamos, where instead of an aluminum foil attached with epoxy, a chemical vapor deposition of aluminum was performed on the backside of the ceramic. The CVD deposited aluminum seemed to survive quite well the shock interactions and produced a clear signal that yielded a spall strength of 2.71 kbar. Further testing should be performed to corroborate this value. More details of these experiments can be found in Denzel's Master Thesis, Ref. [9].

4.2. Dyneema HB25

Dyneema HB25 is composed of many layers made out of ultra-high-density polyethylene(UHDPE) fibers oriented 90 degrees from layer to layer within a polyethylene epoxy matrix. This material was selected as the second layer in our armor concept, the wave dispersion layer due to its theoretical high sound speed along the fiber directions and the potential for a much slower sound speed perpendicular to the fiber orientations. Figure (5a) shows a schematic of the Dyneema fiber layers' orientation, and Figure (5b) shows a scanning electron microscope picture of the top Dyneema layer. In this work we focus on the through direction (perpendicular to the fiber directions) of Dyneema HB25.

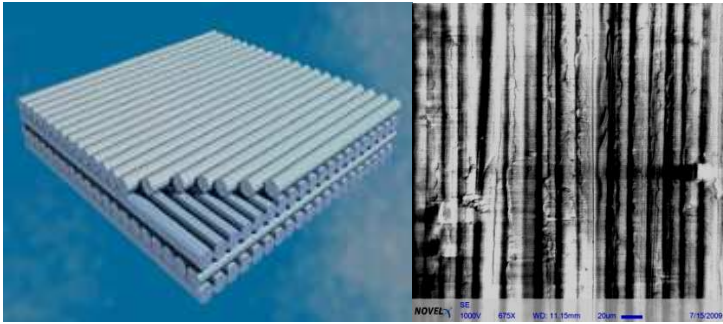


Figure 5. a) Schematic of Dyneema HB25 construction, and b) scanning electron microscope view of the top Dynnema layer, where the fibers can be easily distinguished with diameters from 10 to 15 μm .

Five test shots were performed with Dyneema, the objective was to obtain the Hugoniot along the direction perpendicular to the fiber directions – the low sound speed direction. Three of these tests were performed using conventional shot configuration shown in Figure (2) with a Lucite (PMMA) window behind the target plate and a thin aluminum foil glued between the Dyneema and the PMMA window. The last two shots were performed in an alternate configuration where the Dyneema target was encapsulated between two Cu plates (fully annealed oxygen free high conductivity copper – OFHC Cu). This shot configuration is shown in Figure (6).

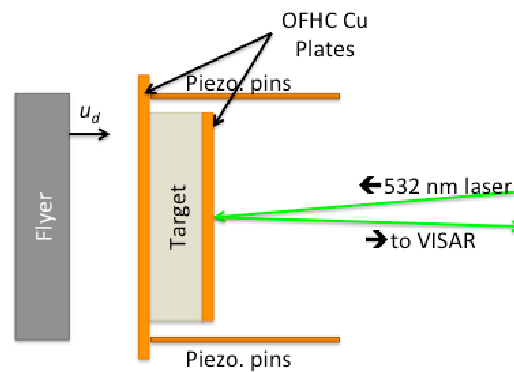


Figure 6. Alternate shot configuration: Dyneema encapsulated between two OFHC Cu plates.

Table 3 tabulates the experimental test conditions and summarizes the results from each test. By varying the impact velocities between 0.25 and 0.90 km/s and flyer materials from Al6061 to OFHC Cu, shock pressures between 4.6 and 32.7 kbar were reached with shock speeds between 2.046 and 3.894 km/s and corresponding particle velocities between 0.237 and 0.884 km/s were recorded. Figure (7) shows a plot of the Hugoniot in U_s - u_p space and shows a comparison with data from Chapman[10] on a slightly different type of UHDPE fiber material and with two different initial densities of HDPE material from Marsh [11].

Table 3. Dyneema HB25 experimental test matrix and summary of results.

Shot No.	Impact Velocity (km/s)	Impacting Flyer Material	Shock Speed (km/s)	Particle Velocity (km/s)	Pressure (kbar)
NPS10-11	0.404	Al-6061	2.181	0.354	7.33
NPS10-15	0.408	Al-6061	2.432	0.353	8.14
NPS10-17	0.250	OFHC-Cu	2.046	0.237	4.60
NPS10-22	0.256	OFHC-Cu	2.144	0.245	9.44
WSU-1	0.900	OFHC-Cu	3.894	0.884	32.70

Within this low-pressure range, Dyneema showed a nonlinear Hugoniot relationship in the through direction (perpendicular to the fiber direction) and was found to be: $U_s = -1.673u_p^2 + 4.847u_p + 0.902$. This fit assumes that the anchor point for the Hugoniot will be near the bulk sound speed of Dyneema and the shear and longitudinal sound speeds presented by Chapman [10] were used to calculate the bulk sound speed. It also appears from the data of this research that the Hugoniot for Dyneema will likely trend to a more traditional

linear response at higher pressures. It is also worth noting that the material we studied is not identical to that studied by Chapman, and so some differences are to be expected. More details of these experiments can be found in Garner's Master Thesis, Ref. [12].

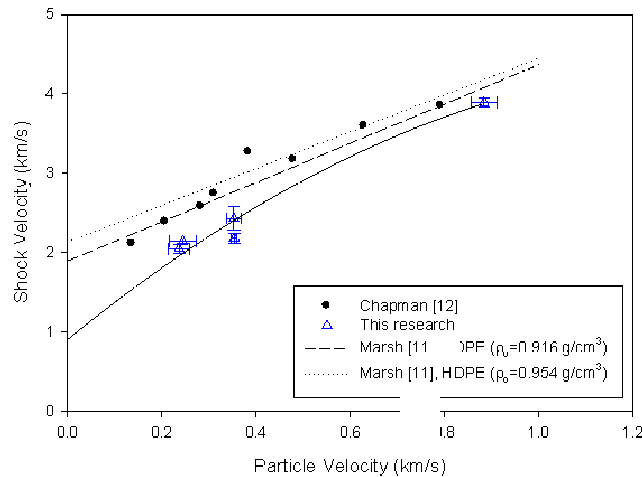


Figure 7. Hugoniot plot for Dyneema HB25

5. CONCLUSIONS AND FUTURE WORK

The first two layers of the armor concept, the high strength – plastic deformation layer, and the wave dispersion layers were identified as Corbit 98 ceramic and Dyneema HB25 fiber composite layers, respectively. These were subjected to dynamic experiments with planar shock inputs to provide high fidelity Hugoniot equations of state. In a shock speed versus particle velocity space (U_S-u_p), the Dyneema HB25 showed a nonlinear Hugoniot relationship in the through direction (perpendicular to the fiber direction) and was found to be: $U_S = -1.673u_p^2 + 4.847u_p + 0.902$. The Corbit 98 ceramic showed a linear Hugoniot relationship of: $U_S = 0.936u_p + 10.53$; with a Hugoniot elastic limit between 74.7 kbar and 90.7 kbar; and a spall strength of 2.71 kbar.

Armed with these high fidelity dynamic response of material characterization, we envision re-doing Ong's hydrocode simulations [1 and 13]. This will lead us to investigate and evaluate any further discrepancies between simulations and experiments.

Furthermore, during experimental testing by Ong [1, 13], it was found that the high strength Corbit 98 ceramic would shatter into millions of small particles. Thus a low spall strength had been anticipated. But due to the very low value of 2.7 kbar, future work would benefit from studying the dynamic response of glassy metals that have much higher (> 10x) spall strengths but with a HEL of only about 50% that of Corbit 98.

With regards to the Dyneema fiber composite material, much further work is needed to characterize the Hugoniot along the fiber direction. In addition, other fiber based materials such as FBO and carbon nanotubes have the potential to have even higher intra-fiber sound speeds and most likely, similar perpendicular sound speeds.

Acknowledgments

The authors would like to thank Dr. Jensen and his team at Los Alamos National Laboratory and Dr. Gupta and his team at Washington State University for their collaborative efforts and for allowing us to use their high performance gas guns, their continuing support, and their outstanding efforts and dedication to this project. We also would like to acknowledge Mr. Jaksha and Mr. Barone of the Naval Postgraduate School for their outstanding support with precision machining and custom electronics development, respectively. We also thank the Office of Naval Research for their funding support during the last three years and the Lawrence Livermore National Laboratory for funding Dr. Sinibaldi's efforts on this project during the last phases of this project.

References

- [34] C.W. Ong, C.W. Boey, R.S. Hixson, J.O. Sinibaldi, "Advanced Layered Personnel Armor", *Int. J. Imp. Eng.*, 38 (2011) 369-383.
- [35] Kolsky, Stress Waves in Solids, Dover (1963).
- [36] Meyers, Dynamic Behavior of Materials, Wiley, (1994).
- [37] R.W. Hemsing, "Velocity Sensing Interferometer (VISAR) Modification", *Rev. Sci. Inst.*, 50:1, (1979) 73-78.
- [38] L.M. Barker and R.E. Hollenbach, "Laser Interferometer For Measuring High Velocities Of Any Reflecting Surface", *J. App. Phys.*, 43:11,(1972) 4669-.
- [39] W. H. Gust and E. B. Royce, "Dynamic Yield Strengths of B4C, BeO, and Al2O3Ceramics," *Journal of Applied Physics*, vol 42, No. 1, January (1971).
- [40] D. E. Grady, "Dynamic Properties of Ceramic Materials," Report SAND94-3266, Sandia National Lab, Albuquerque, NM, February (1995).
- [41] W. D. Reinhart and L. C. Chhabildas, "Strength Properties of Coors AD995 Alumina in the Shocked State," *International Journal of Impact Engineering*, vol.29, pp. 601–619, (2003).
- [42] J.R. Denzel, "Determination of Shock Properties of Ceramic Corbit 98: 98% Alumina", *Master Thesis*, Naval Postgraduate School, Monterey, CA, (2010).
- [43] D. J. Chapman, C. H. Braithwaite, and W. G. Proud, "The response of Dyneema to shock-loading", *Shock Compression of Condensed Matter-2009*, American Institute of Physics, (2009).
- [44] S. P. Marsh, LASL Shock Hugoniot Data, University of California Press, (1980).
- [45] J. R. Garner, "Dynamic Material Properties Of Orthotropic Polymer And Molybdenum For Use In Next Generation Composite Armor Concept", *Master Thesis*, Naval Postgraduate School, Monterey, CA, (2011).
- [46] C. W. Ong, "Investigation Of Advanced Armor Using Layered Construction", *Master Thesis*, Naval Postgraduate School, Monterey, CA, (2009).

STRESS CORROSION FRACTURE OF GLASS

F. Lechenault⁴, C. Rountree², F. Cousin³, L. Ponson⁵, J.-P. Bouchaud⁵, S. Chapuliot and E. Bouchaud¹

¹⁻³ CEA-Saclay, 91191 Gif-sur-Yvette Cedex, France

¹ Service de Physique de l'Etat Condensé (SPEC)

² Service de Physique et Chimie des Surfaces et Interfaces (SPCSI)

³ Laboratoire Léon Brillouin (LLB)

⁴ LCVN, UMR 5587 CNRS-UM2, Place Eugène Bataillon, 34095 Montpellier Cedex 5, France

⁵ Institut Jean Le Rond d'Alembert, Case 162, 4 Place Jussieu, 75252 Paris Cedex, France

⁶ CFM, 6 Boulevard Haussmann, 75009 Paris, France

⁷ AREVA, Tour Areva, 92084 Paris-La Défense, France

Although the stress corrosion fracture of silicate glasses in a humid environment was characterized long ago, the mechanisms involved at the nanometer scale are still controversial. In particular, the existence of a damage zone is an open question.

So that one may probe the quantity of water entering the glass during the fracture process, we have grown subcritical cracks in a controlled stable way within a saturated heavy water atmosphere. The fracture surfaces were probed with neutron reflection, and it was shown that heavy water had actually penetrated into the bulk of the material around the crack tip by ~10nm. Since water molecules hydrolyze the Si-O bonds, their presence reveals the existence of damage.

In order to predict the water concentration profile, we have built up a finite element (FE) model which takes into account the enhanced diffusion of water in the highly deformed solid around the crack tip which progresses at a prescribed applied stress intensity factor KI. Damage is supposed to be proportional both to time and to the water concentration. The resulting water concentration profile is shown to be consistent with the neutron reflection measurements. The model also leads to an exponential dependence of the crack velocity with KI, as observed in Stage I stress corrosion. We believe that this model is a good description of the stress corrosion phenomenon in an amorphous material.

STRAIN-HARDENING IN NANO-STRUCTURED SINGLE PHASE STEELS : MECHANISM AND CONTROL

O. Bouaziz^{1,2} and D. Barbier²

¹ArcelorMittal Research, Voie Romaine-BP30320, 57283 Maizières-lès-Metz Cedex, France

²Centre des Matériaux, Ecole des Mines de Paris, CNRS UMR 7633, B.P. 87, 91003 Evry Cedex, France

Abstract. The detrimental effect of grain size refinement on the strain hardening is highlighted in single phase steels. A physical based approach for understanding the underlying mechanisms is presented. In order to overcome this limitation a promising metallurgical route exploiting the thermal stability of mechanically induced twins in austenitic steels has been successfully applied to a stainless grade confirming the opportunity to get nano-structured alloys exhibiting high yield stress with high strain-hardening.

1. INTRODUCTION

In order to combine yield stress higher than 1000MPa and damage resistance, there is actually a major issue for the development of single phase steels for structural applications. The main strategy reported in the literature is based on an intense grain refinement down to submicronic size. As reported in Fig.1., while the strength can be significantly increased by reducing the grain size, a crucial limitation is a very low uniform elongation due to the decrease in strain-hardening capability. This aspect is very detrimental for the stability of the plastic flow required for any forming operation. This problem is not only related to single phase iron based system. All the metallic alloys exhibit the same trends. This is the reason why this publication present in a first part a mechanistic approach explaining the effect of grain size refinement on the strain hardening and a promising strategy for overcoming this limitation is presented in the last part.

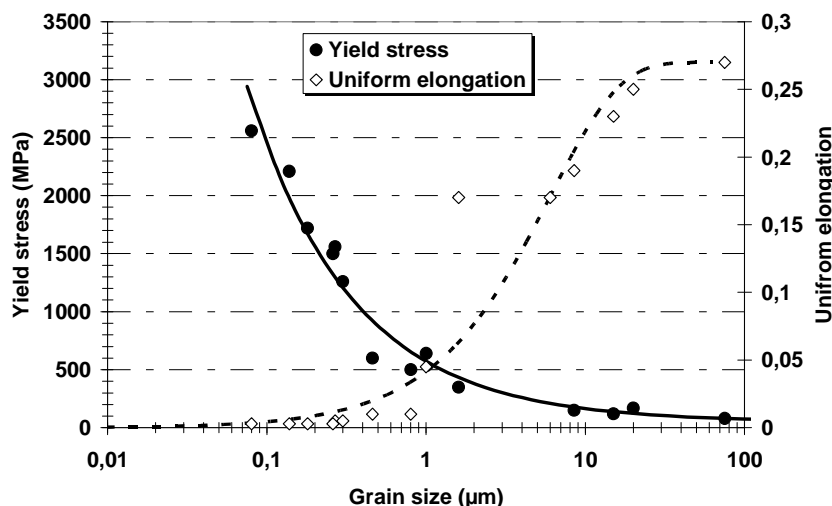


Figure 1. Evolutions of the yield stress and of uniform elongation as a function of grain size for pure iron and IF steels (data from [1-5]).

2. MECHANISMS AND MODELLING

For nano-crystalline materials, there appears to exist a general consensus regarding the principal features of plastic deformation in the range of ultrafine or nano scale grain sizes. These are as follows:

- The growing role of the diffusion-controlled mechanisms of plasticity associated with grain size reduction is expected to lead to the following effects: (i) decrease in the strain hardening and (ii) increase of the strain rate sensitivity of the flow stress [6].
- Grain boundaries act as both sources and sinks for dislocations, as demonstrated mainly by large-scale molecular dynamics (MD) simulations [7-9].

Despite the successes of MD modelling in identifying the elementary mechanisms of plasticity of nanocrystals, it is not always easy in such simulations to extract the underlying physical processes. Part of the problem is the time scale of the MD simulations, which is not representative of the real deformation time scale. Issues with the predictive capability of MD simulations and the interpretation of the events observed in numerical experiments have been recently discussed by Helena van Swygenhoven [9]. This is the reason why a “transparent” physical based approach has been recently proposed and assessed suitable to explain the low strain-hardening capability in nanostructured materials through a low storage rate of dislocations [10]. A grain of diameter d is considered. If a dislocation is nucleated at a grain boundary and traverses the grain, the plastic shear strain it produces is given by :

$$\gamma = \frac{b}{d} \quad (1)$$

where b is the magnitude of the dislocation Burgers vector.

The characteristic time taken by a dislocation to be emitted and to travel through the grain is :

$$t_p = \frac{\gamma}{\dot{\gamma}} = \frac{b}{d \cdot \dot{\gamma}} \quad (2)$$

with $\dot{\gamma}$ being the plastic shear rate.

After traversing the grain, the dislocation can be stored at the boundary (as in the case of the classical Hall-Petch picture of pile-up formation) or to be absorbed into the boundary. Absorption basically means that the atomic step that would be produced by the dislocation is accommodated by “re-shuffling” of atoms - most probably by diffusion along the boundary. The relaxation time for this diffusive mechanism of dislocation accommodation within the boundary can be estimated as :

$$t_r = \frac{d^2}{D_{gb}}, \quad (3)$$

where D_{gb} is the grain boundary diffusivity, which we shall assume to be grain-size independent.

Using Eqs. (2) and (3) it is now possible to define a critical grain size d_c for which the two characteristic times are equal. Setting

$$t_r = t_p \quad (4)$$

yields for the critical grain size :

$$d_c = \left(\frac{D_{gb} \cdot b}{\dot{\gamma}} \right)^{1/3} \quad (5)$$

Obviously, for $d \ll d_c$ the diffusive relaxation is predominant, and the storage of dislocations is negligible. In this regime, no strain hardening will occur.

Of course, the cessation of dislocation storage on crossing the d_c boundary is an idealisation, as due to a distribution of grain sizes some grains would be ‘supercritical’ and will still contribute to strain hardening. It can be claimed, however, that a pronounced drop in the strain hardening coefficient will occur when d falls below d_c .

To quantify the effect of the grain size on the strain hardening behaviour within a common approach, we use the Kocks-Mecking-Estrin (KME) model of strain hardening [11-14]. In this model, the evolution of the dislocation density ρ is controlled by the dislocation mean free path L represented through :

$$\frac{1}{L} = \frac{1}{d} + k\sqrt{\rho} \quad (6)$$

Here k is a constant coefficient, which can be expressed in terms of the Stage II strain hardening coefficient for a coarse-grained material. Diffusive relaxation and the attendant loss of ability of grain boundaries to act as impenetrable obstacles to dislocations can be included in the dynamic recovery term of the evolution equation. Indeed, in the spirit of the above argument and using Eqs. (2) and (3), we can define the probability for a dislocation not to get absorbed in a boundary as :

$$P = \exp\left(-\frac{t_p}{t_r}\right) \quad (7)$$

or

$$P = \exp\left(-\left(\frac{d_c}{d}\right)^3\right) \quad (9)$$

If this probability is zero, all the emitted dislocations are absorbed by grain boundaries and storage is not possible. However, instead of having an abrupt transition between the strain hardening and no strain hardening cases, we include this probability in the KME evolution equation for the dislocation density:

$$\frac{d\rho}{d\gamma} = \frac{1}{bL^*} - f\rho, \quad (10)$$

where f is the strain rate and temperature dependent coefficient, which describes the kinetics of dynamic recovery irrespective of the grain size. The modified mean free path L^* is given by

$$\frac{1}{L^*} = \frac{P}{d} + k\sqrt{\rho}, \quad (11)$$

For a coarse-grained material, P is equal to unity, and the original KME model is recovered. In a general case, the efficiency of grain boundaries in storing dislocations is modified by the grain size dependent factor P , which vanishes asymptotically when d decreases below d_c .

3. A STRATEGY TO OVERCOME THE LIMITATION

Recently it has been shown that the limitation of the decrease in strain-hardening in nanostructured single phase steels can be overcome for Fe-Mn-C austenitic Twinning Induced Plasticity steels by exploiting the thermal stability of mechanically induced twins [15]. It has been reported that an excellent combination of yield stress and work-hardening rate can be achieved by inducing a high density of twins by deformation at room temperature followed by a recovery treatment removing dislocations but keeping the twins. This metallurgical route is now applied to an austenitic stainless steel. A 316L grade has been selected. The as-received material has been cold rolled of 37% reduction. The thermal stability of mechanically induced twins has been assessed. As shown in Fig.2, they are stable even after a recovery treatment at 600°C during one hour. So the tensile behaviour has been characterized for samples in as-received conditions, as-cold rolled and cold rolled followed by the recovery treatment as shown in Fig3. In order to assess the effect on the strain-hardening, it has been plotted in Fig 4 as a function of flow stress. If in as-rolled condition, the strain-hardening is rapidly negligible, the recovered sample exhibits an obvious superior combination between flow stress and strain-hardening compared to the steel in as-received conditions. These results confirm that this route is relevant for producing materials with an excellent combination between yield stress and strain-hardening by microstructural scale refinement.

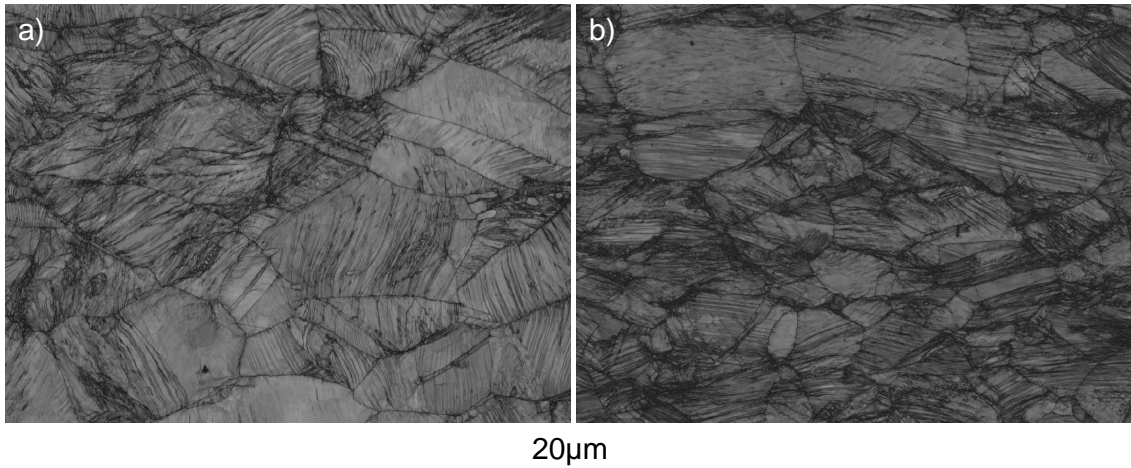


Figure 2. (a) Mechanically induced twins after 37% cold rolling and (b) after recovery at 600°C during one hour.

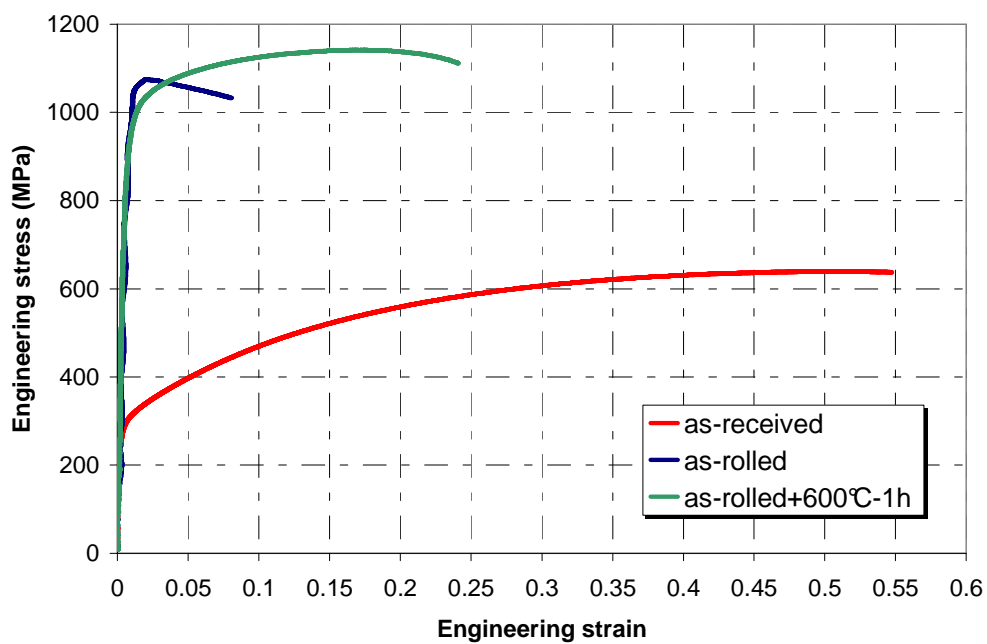


Figure 3. Engineering stress-engineering strain tensile curves for as-received, as-rolled without and with a recovery treatment

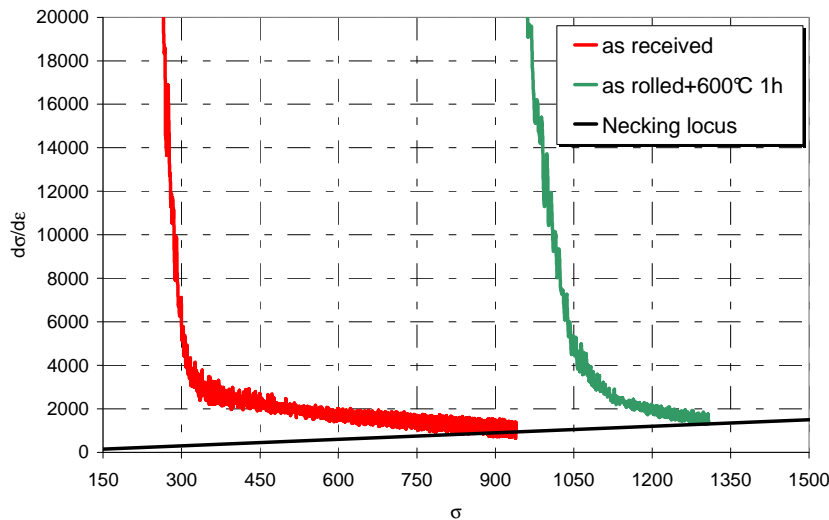


Figure 4. Strain-hardening as a function of flow stress showing the beneficial effect of the proposed metallurgical route.

4. CONCLUSION

The limitation of the strategy of grain size refinement has been highlighted in single phase steels due to the detrimental effect on the strain-hardening controlling the stability of plastic flow required for forming operations. A physical based approach is now available for understanding the underlying mechanisms based on emission, gliding and absorption of dislocations as a function of grain size. In order to overcome this limitation a promising metallurgical route, exploiting the thermal stability of mechanically induced twins in austenitic steels, has been applied to a stainless grade confirming the opportunity to get nano-structured alloys exhibiting high yield stress with high strain-hardening.

References

- [1] S. Takaki, K. Kawasaki, Y. Kimura, J. of Mat. Proc. Tech. Vol. 117 (2001) 359.
- [2] D. Jia, K.T. Ramesh, E. Ma, Acta Mater. 51 (2003) 3495.
- [3] N. Tsuji, Y. Ito, Y. Saito, Y. Minamino, Scr. Mat. Vol.47 (2002) 893.
- [4] O. Bouaziz, T. Iung, M. Kandel, C. Lecomte, J. Phys IV Vol.11 (2001) 223.
- [5] O. Bouaziz, A. Aouafi, S. Allain, Mat. Sc. Forum Vol.584-586 (2008) 605.
- [6] H.S. Kim, Y. Estrin, Appl. Phys. Lett. 79 (2001) 4115.
- [7] K.S. Kumar, H. Van Swygenhoven, S. Suresh, Acta Mater. 51 (2003) 5743.
- [8] D. Wolf, V. Yamakov, S.R. Hillpot, A. Mukherjee, H. Gleiter, Acta Mater. 53 (2005) 1.
- [9] H. Van Swygenhoven, P.M. Derlet, A.G. Froese, Acta Mater. 54 (2006) 1975.
- [10] O. Bouaziz, Y. Estrin, Y. Bréchet, J.D. Embury, Scripta Mat., 63 (2010) 477.
- [11] U.F. Kocks, H. Mecking, Acta Met., 29 (1981) 1865.
- [12] Y. Estrin, H. Mecking, Acta Met., 32 (1984) , 57
- [13] Y. Estrin, « Unified Constitutive Laws of Plastic Deformation », ch. 2, Ed. Krausz, Acad. Press (1996)
- [14] U.F. Kocks, H. Mecking, Prog. Mater. Sci. 48 (2003) 171.
- [15] O. Bouaziz, C. Scott, G. Petitgand, Scripta Mat., 60 (2009) 714.

GENERATION OF NANOCOMPOSITES BY SEVERE PLASTIC DEFORMATION

R. Pippan, A. Bachmaier, A. Hohenwarter and G. Rathmayr

Erich Schmid Institute of Materials Science, Austrian Academy of Sciences, Jahnstr.12, A-8700 Leoben, Austria

This presentation will give an introduction to the generation of nanostructured materials by Severe Plastic Deformation SPD. The paper will be focused on two types of materials. The first one is generated by SPD of coarse composites. This results at very heavy deformation finally in a nanocomposite or sometimes amorphous material. Attention will be devoted to different phenomena during this transformation of the coarse microstructure to the nanostructure. This will contain the grain and phase fragmentation and the formation of super saturated solid solutions and the formation of new phases. The second class of materials is produced by consolidation of powders or sheets of different materials. The final generated bulk materials are similar as the first type. However, due to the freedom in the choice of the pre-materials complete new classes of materials can be generated. In principle, this technique is similar to mechanical alloying, however in this SPD process one ends with a bulk materials. Furthermore, the composition is better defined because no impurities from milling are introduced. Besides the physical phenomena involved during the deformation also the effect of processing parameters as the effect of the strength of the individual phases, the SPD temperature, type of processing, the enthalpy of mixing, etc., will be analysed. The different phenomena resulting in deformation of the nanocomposites and the often generated supersaturated solid solutions will be discussed.

MECHANICAL BEHAVIOR OF ULTRAFINE-GRAINED ALUMINUM AS A FUNCTION OF STRAIN RATE, TEMPERATURE AND LOADING MODE

J. Kokkonen, M. Hokka and V-T Kuokkala

Tampere University of Technology, Korkeakoulunkatu 6, 33101 Tampere, Finland

Abstract Mechanical behavior of equal-channel angular pressed ultrafine-grained commercially pure aluminum was investigated at strain rate range 10^{-4} ... $6 \cdot 10^3$ s⁻¹ and temperatures between -100 °C and +80 °C in compression, tension, and torsion using both low rate hydraulic materials testing machines and Hopkinson Split Bar techniques. For accurate measurement of deformation, the torsion tests as well as some of the tensile tests were also monitored using low and high speed digital photography, which allowed the spatial strains on the specimen surface to be determined with the digital image correlation (DIC) technique. The grain size of the material was found to be quite heterogeneous, varying from 0.1 to 50 μm with an average value around 0.9 μm. In low strain rate compression and torsion tests, the material shows almost ideally plastic behavior, but with increasing strain rate and/or decreasing temperature the material starts to show also slight strain hardening. Despite the heavy deformation during the ECAP treatment, the material is still characteristically ductile, although in tension and torsion the material is prone to deformation localization, which starts rapidly after the yielding. However, even after 300% of shear strain in torsion the specimen does not fail despite the heavily localized deformation. The material shows a clear overshoot in the flow stress after yielding and whenever the strain rate is suddenly increased during the test. After a sudden decrease of strain rate, correspondingly, the flow stress shows a significant drop before saturation through strain hardening at a constant but lower level than before the strain rate drop. The magnitude of this transient behavior during both increase and decrease of strain rate depends on the strain rate and temperature.

1. INTRODUCTION

Ultrafine-grained (UFG) materials with grain size between 100...1000 nm can be manufactured for example by means of severe plastic deformation (SPD). One of the commonly used severe plastic deformation techniques is equal-channel angular pressing (ECAP), where a billet of material is pressed through a die with a channel of constant cross sectional area that makes a sharp bend of 60...120° between the input and output ends of the die. During equal-channel angular pressing the microstructure of face centered cubic (fcc) metals is transformed from deformed cellular sub-grain structure with large proportion of low angle boundaries to ultrafine-grained structure with high amount of high angle boundaries and low amount of sub-structures inside the grains [1-4]. Usually the billet must be pressed through the die several times to enter the ultrafine-grained regime. The existence of so-called non-equilibrium grain boundaries has been proposed for severe plastically deformed ultrafine-grained and nanocrystalline materials [5]. Non-equilibrium boundaries are thought to contain an excess of extrinsic dislocations, exhibit high energy state, and to induce long range stresses inside the grains.

Saturation of flow stress has been reported in several articles for ultrafine-grained commercially pure aluminum at room temperature [6-10]. It is commonly accepted in the literature that the steady state flow is a consequence of a balance between dynamic recovery and strain hardening, which are both based on complex dislocation interactions. Stress saturation can be caused either by the decreased rate of strain hardening or by increased rate of dynamic recovery, or the combination of both. It has been suggested [11] that the reduction in the strain hardening capability of UFG copper is partially caused by the low amount of sub-grain structures so that the storage rate of dislocations inside the grains is reduced and the major part of the dislocations are able to reach the high angle grain boundaries where they are annihilated. In the literature the rate of dynamic recovery has been suggested to increase due to increased rate of diffusion. Amouyal et al. [12,13] suggested that UFG Cu and Cu-Zr exhibit higher rate of diffusion due to the non-equilibrium grain boundaries that formed during the ECAP process. They measured diffusion rates over two orders higher for non-equilibrium boundaries than for relaxed boundaries similar to those in coarse grained materials. Divinski et al. [14] found free volume in the form of non-equilibrium interfaces, vacancy clusters, nanovoids, and micropores, which they suggested to increase the short-circuit diffusion rate of the material significantly at low temperatures. Setman et al. [15] measured very high concentrations of deformation-induced vacancies in Cu and Ni after the ECAP procedure. High amount of vacancies drive diffusion and increase the rate of annihilation of dislocations for example by dislocation climb, and therefore, also the rate of dynamic recovery. Fujita et al. [16] showed that the

interdiffusion rates in UFG Al alloys with high amount of high angle boundaries are much higher compared to materials with high amount of low angle boundaries.

Ahmed et al. [17] suggested that grain boundary mediated deformation itself contributes only marginally to plastic deformation although the increased rate of dynamic recovery at grain boundaries makes plastic deformation possible in UFG and nanocrystalline materials. Chinh et al. [18], on the other hand, have reported grain boundary sliding in micro-indentation tests at room temperature due to an excess of extrinsic dislocations at non-equilibrium grain boundaries. According to them, sliding can accommodate a significant part of the plastic deformation. The role of grain boundary sliding and other grain boundary processes that could carry plastic deformation at room temperature in UFG fcc materials is still under debate, but it is generally accepted that grain boundary processes have a significant effect on the plastic deformation properties of ultrafine-grained and nanocrystalline fcc metals.

Ultrafine-grained commercially pure aluminum has been reported in the literature to exhibit yield point or stress overshoot behavior [7, 19, 20]. Hockauf et al. [7] attributed the upper yield point phenomenon in this material to microstructural rearrangement due to strain bath change, which causes softening after yielding. Gragio et al. [21] observed plastic instability and yield overshoot in rolled coarse-grained commercially pure aluminum, which they suggested to be a consequence of textural softening. They tested their material at several orientations with respect to the rolling direction, and in some orientations the material showed yield peaking and softening, whereas for other orientations no signs of peaking and succeeding softening were seen. Tsuji et al. [20] reported a distinct yield drop behavior and Lüders band formation for commercially pure UFG aluminum, and Nijs et al. [22] similar phenomena for Al-1 wt.% Mg.

2. MATERIAL

The ultrafine-grained structure of commercially pure aluminum 1070 was achieved by equal-channel angular pressing of the material through a 2-turn die four times using the route C+B_C. The dimensions of the bars with a square cross-section were 120*26*26 mm. Figure 1 shows an electron backscatter diffraction (EBSD) orientation imaging map of the material taken perpendicular to the ECAP pressing direction. The grain structure is heterogeneous with a bimodal size distribution, containing areas of large grains (up to 50 μm) with internal dislocation and cell structure, and areas of ultrafine grains where the deformation has induced refinement of grains that are fairly free from internal defect structures. The average grain size d_{avg} of the material is between 0.8...1.1 μm depending on the ECAP-plane (X, Y, Z) and place of observation. Boundaries with misorientations of 15° or more were defined as high angle boundaries (HABs) for the grain size determination, while boundaries below 2° were omitted in the analysis.

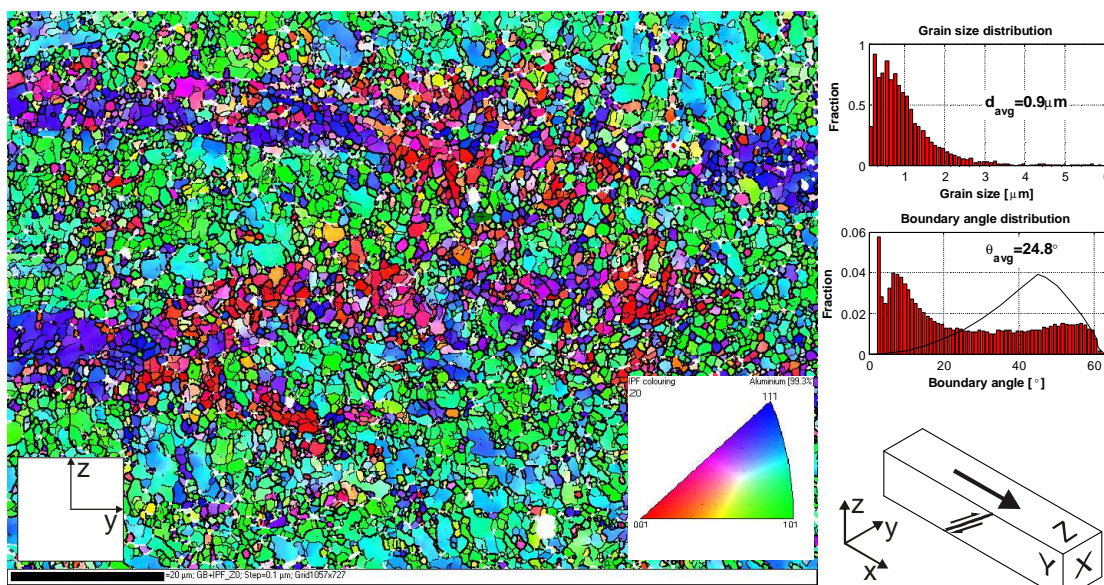


Figure 1. IPF-colored EBSD orientation imaging map (OIM) taken from the plane X (perpendicular to the pressing direction), revealing the grain structure of the material. Boundary angle and grain size distribution diagrams are shown on the right hand side of the figure.

The boundary angle distribution diagram shows a peak at angles around 10°, while the highest frequency of boundaries still occurs at low misorientation angles. The distribution of the angles is far from the Mackenzie distribution, i.e., random distribution of boundary angles in the cubic lattice. The fraction of HABs (>15°) determined from four maps of the X plane is 59%, and the average grain boundary angle θ_{avg} is 25°. Due to the still relatively high amount of low angle boundaries and slightly elongated grains especially on the Y-plane, the material hardly has any superplastic properties. The fraction of HABs and the average boundary angle seem to be in the same range with the values found in the literature. Articles report the fraction of HABs to be within the range of 40...81% and the average boundary angle within the range of 19...30.3° for commercially pure aluminum produced using routes C or B_c after 8 or more passes [3, 4, 23-25]. The benefit of using modern EBSD equipment and software for orientation imaging is the ability to cover large areas to get reliable and statistically relevant data of the grain structure and texture of the material. The disadvantage of the method is the poor resolution resolving small misorientations below 2°, which might lead to too high fraction of HABs and too high value of the average boundary angle.

3. RESULTS AND DISCUSSION

At quasi-static strain rates, the studied ultrafine-grained aluminum shows ideally plastic behavior in compression at RT and 80 °C after some softening or hardening in the beginning, as shown in Figure 2a. When the strain rate is increased, the material starts to show more persistent strain hardening, especially when the temperature is decreased to -100 °C (blue curve in Figure 2a). Figure 2c shows how the material behaves at higher compressional strains. The tests were interrupted at every 10% of true strain to renew the MoS₂ based lubrication. At 10^{-3} s^{-1} the material slightly softens at RT before the stress level settles to a more or less constant value, and hardens a little bit in the beginning of the test at 80 °C before the flow stress saturates. At $\sim 2000 \text{ s}^{-1}$ the material shows low but positive strain hardening rate throughout the test. Under shear deformation in torsion tests shown in Figure 2b, the material softens slightly at the lowest strain rate $1.6 \cdot 10^{-4} \text{ s}^{-1}$, but as the strain rate is increased, the behavior first changes to steady state flow at intermediate strain rates and then to slight but definitive hardening at strain rates above 500 s^{-1} . At higher strains in high strain rate torsion tests the material starts to soften obviously due to adiabatic heating. Figure 2b shows the localization of the shear deformation during a torsion test at the strain rate of $1.6 \cdot 10^{-4} \text{ s}^{-1}$. Regardless of this severe localization of deformation the specimen does not fail even after 300% of shear strain.

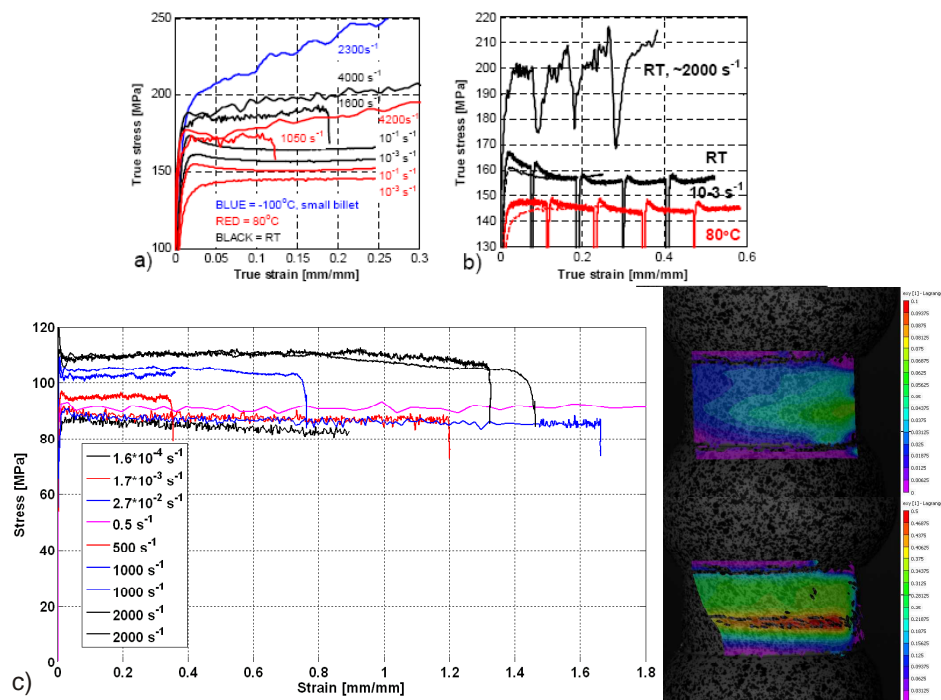


Figure 2. Behavior of UFG aluminum in compression at broad ranges of strain rate (a), interrupted compression tests at RT and 80°C at 10^{-3} s^{-1} and at RT at $\sim 2000 \text{ s}^{-1}$ (b), and behavior of the material in torsion (c). The color plots on the right show how the DIC determined surface deformation of the torsion specimen evolves when loaded at the strain rate of $1.6 \cdot 10^{-4} \text{ s}^{-1}$.

As seen in Figure 3a, in tension the material suffers from immediate necking due to tensile instability. Decreasing temperature and increasing strain rate affect the yield strength of the material similar to the compression tests. Still at 800 s^{-1} and $-50 \text{ }^\circ\text{C}$ the material does not show enough strain/strain rate hardening to postpone the neck formation although the stress does not anymore start to decrease immediately after yielding. Figure 3b shows the deformation on a tensile specimen surface tested at 1600 s^{-1} up to 21% of engineering strain. The deformation is concentrated in the center region of the specimen gage section due to necking, which starts quite soon after initial yielding, as shown by the waterfall plot in Figure 3b. Neither shear bands nor Lüders bands were observed in the tensile specimens of the used geometry.

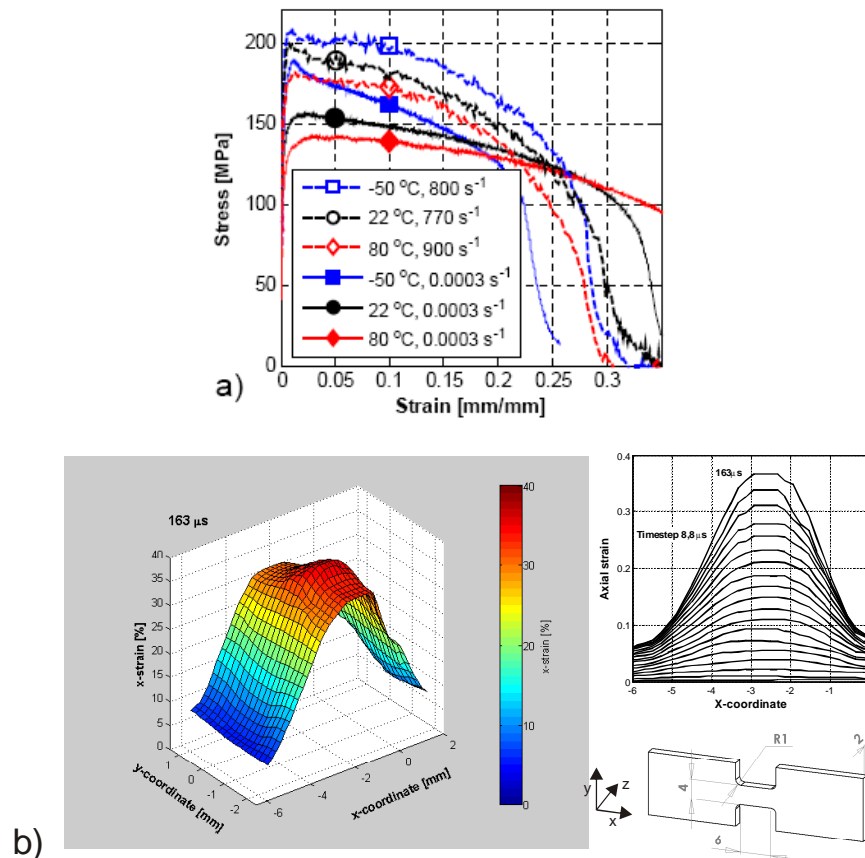


Figure 3. Deformation of UFG aluminum in tension at different initial temperatures and strain rates (a), and deformation of the tensile specimen surface in a test conducted at 1600 s^{-1} as determined with the DIC technique (b).

In compression and shear the test material shows smooth stress overshoot in the beginning of the test at quasi-static and intermediate strain rates. After overshoot the stress drops gradually to a more or less constant level. At very low strain rates in shear the material shows slight softening. Overshooting of stress is also observed in some of the compression and shear tests done at high strain rates with the Hopkinson technique, but the reliability of the data at small strains in Hopkinson tests is somewhat questionable due to the finite time needed to reach the stress equilibrium. In some of the tensile tests a small stress peak is also slightly visible, but no signs of Lüder's deformation were witnessed. At the lowest strain rates (10^{-3} s^{-1} and below), and especially when the temperature is increased, the overshoot is usually missing and the material shows slight hardening before the stress reaches a constant value. The overshoot phenomenon has been reported earlier in tension e.g. by May et al. [19] at higher quasi-static strain rates. Overshooting appears again if the material is unloaded and reloaded, as can be seen in Figure 2b. The mobile dislocations carrying out the deformation are obviously either pinned or relaxed at unloading, resulting in the yield peak when the material is reloaded. At these temperatures dislocations carry out the major part of plastic deformation of the material, but the generation, annihilation and reactions of dislocations are likely to be affected also by the increased diffusion rates, especially at the (possible) non-equilibrium boundaries, leading to diffusion assisted climb of dislocations due to the increased amount of deformation induced vacancies, or even grain boundary sliding. Recovery of the

mobile dislocations during unloading may also become significant due to the increased rate of diffusion. Saimoto et al. [26] studied the dynamic point defect pinning of dislocations in coarse grained commercially pure aluminum and reported weaker transients when strain rate was changed, i.e., less hardening when strain rate was decreased and lower peaking and softening when strain rate was increased. They suggested that dislocation pinning by vacancies and vacancy clusters causes these transients when the strain rate change disturbs the dynamic balance in the occurrence of pinning. This explanation also for the current ultrafine-grained material is supported by the fact that very high vacancy concentrations have been reported for severely deformed fcc metals, which could lead to strong transients at yielding. It is noticeable that in our material the peaking persists and happens again when the material is reloaded. This implies that if the peaking is caused by the pinning of dislocations by vacancies, the vacancy content would persist as well.

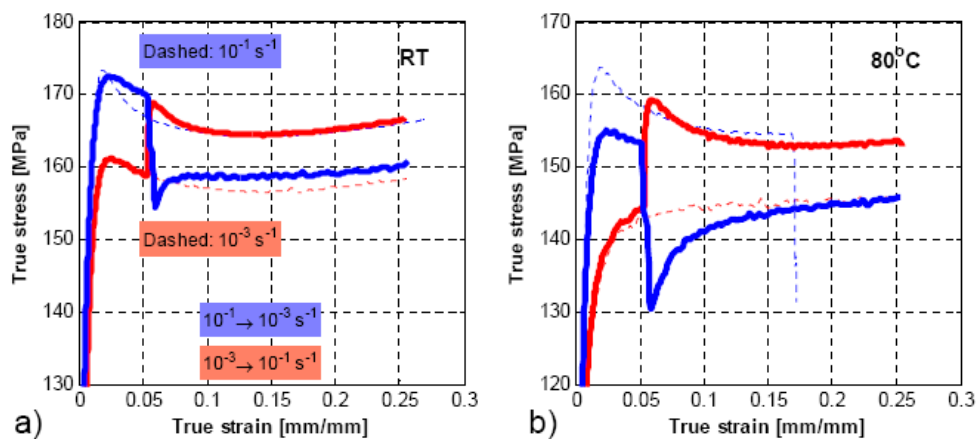


Figure 4. Strain rate jump experiments at low strain rates a) at room temperature, and b) at 80°C.

The studied material shows also very distinct transients when the strain rate is suddenly changed, as shown in Figure 4. This implies that the dynamic equilibrium between different dislocation processes leading to the ideally plastic behavior is disturbed during these events. When the strain rate is increased during the test, the stress first rises and overshoots, after which the material softens to a new saturation level that is higher than the saturation stress before the increase. The overshooting of stress at strain rate increase resembles that observed during the initial yielding, and therefore it may be concluded that they both are caused by the same phenomenon. At strain rate decrease the stress drops significantly, after which the material hardens to a new saturation stress level that is lower than before the decrease. The magnitude and duration of the transients increase proportionally more when the temperature or the change in the strain rate is increased within the tested temperatures (RT and 80 °C) and strain rates (10^{-3} , 10^{-2} , and 10^{-1} s⁻¹). May et al. [8] reported similar transients for their commercially pure UFG aluminum when they changed strain rate during the test, which they attributed to dynamic strain ageing by impurity atoms. Commercially pure aluminum contains always some amount of impurity atoms and in UFG state probably also a high concentration of vacancies, which may induce dislocation pinning and dynamic strain aging. The grain size of commercially pure UFG aluminum has also been reported to increase slightly during simple compression after the ECAP procedure [8, 9]. May et al. [8] suggested that during the compression the high angle boundaries stay nearly intact whereas the low angle boundaries migrate and dissolve during deformation. Valiev et al. [27], on the other hand, suggested that due to the non-equilibrium boundaries the grain boundaries of UFG Cu migrate during simple compression and the grain size increases. Blum et al. [28] suggested that the grain size of UFG materials should not be treated as constant during deformation after severe plastic deformation but as variable, which depends on the effective stress and strain. The above mentioned re-organization of the microstructure may have an effect on the transients when the material yields or the strain rate is changed during a test, because the mechanisms contributing to the plastic deformation are disturbed from their former state when the plastic strain rate changes. However, the exact reasons for the stress overshoot at yielding and at strain rate increase and for the significant stress drop and subsequent hardening at strain rate decrease are still not perfectly clear and need further investigations.

4. CONCLUSIONS

Ultrafine-grained ECAP processed commercially pure aluminum 1070 with high amount of high angle boundaries exhibits stress saturation or slight softening at low and intermediate strain rates in shear under torsional loading and in simple compression. The material shows increasing hardening at higher strain rates and lower temperatures where the strong dynamic recovery of the UFG material is partially suppressed. The material is prone to deformation localization, as evidenced by digital image correlation (DIC) methods, under torsional loading in shear and in uniaxial tension due to the absence of high enough rate of strain hardening. The material is still characteristically ductile being able to undergo large torsional (shear) and compressional deformations without failure. The material also shows distinct transients at yielding and at strain rate changes, but no definite cause for the transient behavior could be identified.

Acknowledgements

This work was supported by the Graduate School of Tampere University of Technology and by the Academy of Finland under grant No. 133653.

References

- [47] Iwahashi Y., Horita Z., Nemoto M., Langdon T.G. "The process of grain refinement in equal-channel angular pressing", *Acta Mater.*, 49 (1998) 3317-3331.
- [48] Terhune S.D., Swisher D.L., Oh-Ishi K., Horita Z., Langdon T.G., McNelley T.R. "An investigation of microstructure and grain-boundary evolution during ECA pressing of pure aluminium", *Metall Mater Trans A*, 33A (2002) 2173-2184.
- [49] Reihanian M., Ebrahimi R., Moshksar M.M., Terada D., Tsuji N. "Microstructure quantification and correlation with flow stress of ultrafine grained commercially pure Al fabricated by equal channel angular pressing (ECAP)", *Mater Charat*, 59 (2008) 1312-1323.
- [50] Cabibbo M., Blum W., Evangelista E., Kassner M.E., Meyers M.A. "Transmission electron microscopy study of strain-induced low- and high-angle boundary development in equal-channel angular-pressed commercially pure aluminum", *Metall Mater Trans A*, 39 (2008) 181-189.
- [51] Valiel R.Z., Korznikov A.V., Mulyukov R.R. "Structure and properties of ultrafine-grained materials produced by severe plastic deformation", *Mat Sci Eng A-Struct*, 168 (1993) 141-148.
- [52] Rosochowski A., Olejnik L., Gagne J., Ladeveze N., Rosochowska M. "Compression behavior of UFG aluminum", *Proc of the 9th Int. Conference on Material Forming ESAFORM 2006*, (2006) 543-546
- [53] Hockauf M., Meyer L.W., "Work-hardening stages of AA1070 and AA6060 after severe plastic deformation", *J Mater Sci*, 45 (2010) 4778-4789
- [54] May J., Höppel H.W., Göken M. "Strain rate sensitivity of ultrafine-grained aluminium processed by severe plastic deformation", *Scripta Mater*, 53 (2005) 189-194
- [55] El-Danaf E.A., Soliman M.S., Almajid A.A., El-Rayes M.M. "Enhancement of mechanical properties and grain size refinement of commercial purity aluminum 1050 processed by ECAP", *Mater Sci Eng A*, 458 (2007) 226-234
- [56] Sun P.L., Cerreta E.K., Gray III G.T., Bingert J.F. "The effect of grain size, strain rate, and temperature on the mechanical behavior of commercial purity aluminum", *Metall Mater Trans A*, 37A (2006) 2983-2994
- [57] Blum W., Li Y.J. "Influence of grain boundaries on steady-state deformation resistance of ultrafine-grained Cu", *Phys Stat So*, 201 (2004) 2915-2921.
- [58] Amouyal Y., Divinski S.V., Estrin Y., Rabkin E. "Short-circuit diffusion in an ultrafine-grained copper-zirconium alloy produced by equal channel angular pressing", *Acta Mater*, 55 (2007) 5968-5979.
- [59] Amouyal Y., Divinski S.V., Klinger L., Rabkin E. "Grain boundary diffusion and recrystallization in ultrafine grain copper produced by equal channel angular pressing", *Acta Mater*, 56 (2008) 5500-5513.
- [60] Divinski S.V., Ribbe J., Baither D., Schmitz G., Reglitz G., Rösner H., Sato K., Estrin Y., Wilde G. "Nano- and micro-scale free volume in ultrafine grained Cu-1 wt.%Pb alloy deformed by equal channel angular pressing", *Acta Mater*, 57 (2009) 5706-5717.
- [61] Setman D., Schafner E., Korznikova E., Zehetbauer M.J. "The presence and nature of vacancy type defects in nanometals obtained by severe plastic deformation", *Mat Sci Eng A-Struct*, 493 (2008) 116-122.
- [62] Fujita T., Horita Z., Langdon T.G., "Using grain boundary engineering to evaluate the diffusion characteristics in ultrafine-grained Al-Mg and Al-Zn alloys", *Mat Sci Eng A-Struct*, 371 (2004) 241-250.
- [63] Ahmed N., Hartmaier A., "Mechanisms of grain boundary softening and strain-rate sensitivity in deformation of ultrafine-grained metals at high temperatures", *Acta Mater*, 59 (2011), 4323-4334.
- [64] Chinh N.Q., Szommer P., Csanádi T., Langdon T.G., "Flow processes at low temperature in ultrafine-grained aluminum", *Mat Sci Eng A-Struct*, 434 (2006) 326-334.
- [65] May J., Amberger D., Dinkel M., Höppel H.W., Göken M. "Monotonic and cyclic deformation behaviour of ultrafine-grained aluminium", *Mat Sci Eng A-Struct*, 483-483 (2008) 481-484.
- [66] Tsuji N., Ito Y., Saito Y., Minamino Y. "Strength and ductility of ultrafine grained aluminum and iron produced by ARB and annealing", *Scripta Mater*, 47 (2002) 893-899.

- [67] Gracio J.J., Lopes A.B., Rauch E.F. "Analysis of plastic instability in commercial pure Al alloys", *J Mater Process Tech*, 103 (2000) 160-164.
- [68] Nijs O., Holmedal B., Friis J., Nes E. "Sub-structure strengthening and work hardening of ultra-fine grained aluminium-magnesium alloy", *Mat Sci Eng A-Struct*, 483-484 (2008) 51-53.
- [69] Sun P.L., Cerreta E.K., Gray III G.T., Rae P. "The influence of boundary structure in the mechanical properties of ultrafine grained AA1050", *Mat Sci Eng A-Struct*, 410-411 (2005) 265-268.
- [70] Berta M., Apps P.J., Prangell P.B. "Effect of precessing route and second phase particles on grain refinement during equal-channel angular extrusion", *Mat Sci Eng A-Struct*, 410-411 (2005) 381-385.
- [71] Cabibbo M. "A TEM Kikuchi pattern study of ECAP AA1200 via routes A, C, B_c", *Mat Charact*, 61 (2010) 613-625.
- [72] Saimoto S., Cooley J., Larsen H., Scholler C. "Kinetic analysis of dynamic point defect pinning in aluminium by strain rate changes", *Phil Mag*, 89 (2009) 853-868.
- [73] Valiev R.Z., Kozlov E.V., Ivanov Yu. F., Lian J., Nazarov A.A., Baudelet B. "Deformation behaviour of ultra-fine-grained copper", *Acta metal mater*, 42 (1994) 2467-2475.
- [74] Blum W., Li Y.J., Durst K. "Stability of ultrafine-grained Cu to subgrain coarsening and recrystallization in annealing and deformation at elevated temperatures", *Acta Mater*, 57 (2009) 5207-5217.

STUDY OF THE DYNAMIC COMPRESSION BEHAVIOR OF BULK NANOMATERIALS BY SPLIT HOPKINSON PRESSURE BAR : CASE STUDY FOR ALUMINIUM-DIAMOND NANOCOMPOSITES, AND NANOSTRUCTURED MOLYBDENUM

C. Terner, E. Barraud, S. Lemonnier and F. Moitrier

French German Research Institute of Saint-Louis, 5 rue du Général Cassagnou, 68300 Saint-Louis, France

The extremely demanding specifications for ballistic protection and ammunition require the development of materials with highly advanced mechanical properties. Combatant protections involve the use of materials that combine high mechanical strength, hardness and high ductility with reduced weight. Aluminium as a lightweight metal possesses high potential for this area, but to fulfil this task its limited mechanical properties have to be improved. A solution is the development of a nanocomposite, associating a nanostructured aluminium matrix with nanoscale reinforcements in the form of nanodiamonds, which combine very high hardness with low weight. The liners of shaped charge ammunition demand materials with high purity, high density and high ductility. Among the possible liner materials, Molybdenum exhibits in comparison to copper, the most currently used metal, a 15% higher density, a potentially higher ductility in the jet during the detonation and a 30% higher sonic velocity. Up to now only coarse grain materials have been used, and it is expected that a refinement of the microstructure lead to a strong increase in the performances of the shaped charge.

Currently, powder metallurgy is the most efficient way for the fabrication of bulk nanostructured materials and nanocomposites and is well suited to ceramics as well as metals including aluminium and molybdenum. In this study the powder was energetically activated by high energy ball milling to refine the grain size to the nanoscale and then densify by sintering using the Spark Plasma Sintering process to produce a nanostructured bulk material.

The influence of the nanostructure on the materials sensitivity to deformation at different strain rates has been studied through quasistatic and dynamic compression tests. For the aluminium, in the quasistatic as well as in the dynamic test, the strengths increase regularly with the milling time up to 3 hours milling. For higher milling times, no more increase is observed and the maximum strength value reaches over 400MPa in both conditions. These results evidence that the energetically activation of the aluminium powder by high energy ball milling, nanoscale structure refinement and defect introduction, does not seem to have an effect on the sensitivity to strain rate changes in the mechanical strength. Contrary, the addition of 5 at% nanodiamonds leads to different behaviours for quasistatic and dynamic compression tests. No stabilisation in the material strength is observable and for 10 hours milling, values of about 500MPa and 850MPa are reached respectively for quasistatic and dynamic tests. So the resistance of aluminium-diamond nanocomposites is higher than the resistance of the pure aluminium and is strongly dependent of strain rate sensitivity. For the molybdenum specimens the material strength increases with the milling time up to about 2200MPa and 2700MPa respectively for the quasistatic and dynamic tests indicating that molybdenum samples are sensitive to strain rate changes.

DIAMOND LIKE CARBON COATINGS FOR AUTOMOTIVE APPLICATION : EFFECT OF MICROSTRUCTURE ON HARDNESS MEASUREMENT METHODOLOGY BY NANOINDENTATION METHOD

J. Benoist¹, T. Thomé², M. Diaby¹, M. Neret², T. Prenant², J. Guy¹, A. Ponzi¹, N. Eckle¹, S. Ben Rhouma³, G. Meunier¹ and V. Branger¹

¹PSA Peugeot Citroën, Centre technique de Belchamp, 25218 Montbéliard France

²PSA Peugeot Citroën, Centre technique de Vélizy, Route de Gisy, 78 943 Vélizy-Villacoublay, France

³PSA Peugeot Citroën, Centre technique de La Garenne, 18 rue des Fauvelles 92250 La Garenne Colombes, France

Abstract. Engine and gear box downsizing in automotive industry leads to severe mechanical working conditions and require innovative solutions to reduce wear and friction losses.

Diamond-Like Carbon (DLC) coatings are known to have excellent tribological properties such as low wear coefficient and high hardness, which vary according to the deposition parameters. Hardness is one of the most important characteristic for this kind of coating for a given application in automotive industry. However, it is difficult to measure it with a quantitative method and nonetheless nanoindentation seems to be the most adapted, we show with a concrete example that coating thickness can have a huge influence on the hardness determined by nanoindentation. Indeed, hardness can be underestimated because of the substrate influence in certain cases. Additional information like the knowledge of the thickness, the sp²/sp³ ratio and the wear resistant with the antagonist pieces are needed for a complete qualification of the DLC.

1. INTRODUCTION

Engine and gear box downsizing in automotive industry lead to severe mechanical working conditions and requires innovative solutions to reduce wear and friction losses in these mechanical machines [1]. The pollution cost for one given amount of CO₂ emission is so high that previously expensive technology becomes advantageous in the case of mass production.

Diamond-Like Carbon (DLC) coatings are known to have excellent tribological properties such as low friction coefficient, wear resistance and high hardness and could be a generalized alternative for many given applications such as engine tappet, piston ring, piston pin and in automotive sport field [2, 3].

It is well known that DLC properties vary according to the deposition parameters and hardness is one of the most important characteristic for a given application in automotive industry. However, hardness is difficult to measure with a quantitative method because of the thickness influence in the case of extreme hard thin films [4]. Some phenomena appear like a non regular response of the coating during indentation and are difficult to understand for people not familiarized with these materials, particularly the hardness value to choose.

The first part of the present investigation consists in the hardness determination by nanoindentation and microstructural characterization performed by using a Scanning Electron Microscope equipped with a field emission gun and a X-Ray Photoelectron Spectroscopy to study their chemical composition, thickness, multilayer structure and sp²/sp³ ratio respectively. Then, we discuss about hardness measurement interpretation and finally the correlation with wear resistant tests to classify the DLC according to their hardness.

2. EXPERIMENTAL DETAILS AND RESULTS

2.1. Samples

The samples studied are engine piston pins coated by DLC of two different suppliers who use different coating technology. Indeed, three piston pins were coated by PVD technology while the last one was coated by PaCVD technology.

The following table 1 presents the different samples and information available given by the suppliers.

Table 1 : Sample's information.

Supplier	samples	Technology	DLC's family	Substrate
A	DLC 1	PVD	Ta-C	Stainless steel
	DLC 2	PVD	Ta-C	
	DLC 3	PVD	Ta-C	
B	DLC 4	PACVD	a-C:H	

The Ta-C coating is known to be very hard. There is no hydrogen and the fraction of tetrahedral carbon sp³ is very high.

2.2. Nanoindentation

Nanoindentation measurements were performed with a commercial CSM nanoindenter instrument, equipped with a Berkovitch indentation probe diamond tip. It is a three-sided Berkovitch pyramid with an apex angle of 65.3 degrees. Indentations were performed on DLC surface. Scanning area is about 1.5 mm X 100 μm. Nanoindentation theory and methodology are described in references [5, 6 and 7]. Figure 1 represents the hardness gradient according to the load applied on each DLC. This corresponds to an indentation depth close to 50 nm for the slight load and close to 450 nm for the highest load. Plotting the hardness as a function of load and not as a function of depth favors regular curve in our case.

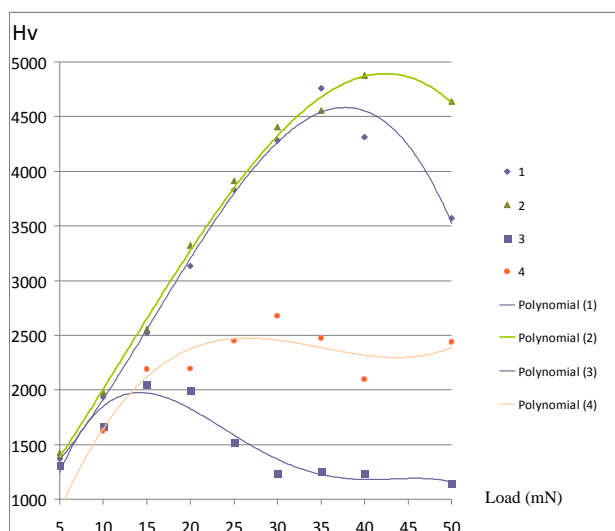


Figure 1. hardness gradient obtained on four different commercial DLC.

Polynomial simulations are superposed on the data to facilitate the comparative analysis with a better view. A first reasoning is to consider that hardness is close to the highest point of each plotted data and an easy interpretation of the curve suggests that DLC 1, 2 and 4 are much harder than DLC 3. The hardness values are reported in table 2.

2.3. XPS

sp²/sp³ ratio is determined by using a XPS AXIS ULTRA KRATOS. Analyses were performed on DLC surface with a monochromatic Al K α source of X-Rays (1486.6 eV). Scanning area is about 500x500 μm^2 .

Results obtained are also summarized in the table 2.

No significant difference is observed between DLC samples 1, 2 and 3. DLC4 has the highest sp²/sp³ ratio.

A higher sp²/sp³ ratio for the a:C-H DLC 4 coating was expected because of the technology used. But in the case of DLC 3, hardness gradient and maximum values are found lower than other Ta : C DLC coatings for a similar sp²/sp³ ratio. DLC 4 seems harder than DLC 3 although, Ta-C coating is known to be harder than a:C-H coating.

2.4. Scanning electron microscopy and sample preparation

Samples were prepared for scanning electron microscopy with a precision cut off machine SECOTOM 50 (BUEHLER) and finally by surface polishing using a STRUERS ROTOPOL-15 (Struers). Scanning electron microscopy was performed on a JSM-6340F JEOL microscope. Chemical analysis was performed with Energy Dispersive X-ray Analysis (EDX) with an INCA ENERGY 300 spectrometer coupled with the microscope.

Micrographs obtained enable measuring the thickness of the different layer of these DLC. Thickness and chemical composition of the different layers are also summarized in the following table 1.

The three Ti-Ta-C are composed of a Ti based intermediate adhesion layer and the DLC 4 has a Cr intermediate adhesion layer.

The DLC 3 is the thinnest one with a carbon base layer lower than 1 μm . DLC 2 and DLC 4 are composed of two carbon base layers doped with Si.

2.5. Tribological test

Tribological tests were performed with the 4 samples according to the following procedure.

Before the test, measurements of the sample roughness were carried out by using the Hommel Etamic Surfscan apparatus, equipped by a 2 μm -radius-stylus.

The connecting rod of the engine was machined to adapted the tribological system 'piston pin / conrod' to the bench test. The bench test used is a classical bearing machine which axis was set to rotate at a speed of 193 rpm/min representing a linear speed of 0.24 m/s. The load applied was 160 daN what leads to a contact pressure of 30 MPa.

The test was performed in a lubricated environment. The lubricant used was a commercial 5W30 grade one, and was heated at 110°C.

The complete duration of the tests was 150 minutes. A running-in of 60 minutes was carried out, and test was stopped at different interval for evaluation. The weigh loss compared was then calculated.

3. DISCUSSION

Table 2 : Synthesis of microstructural results : chemical compositions*, thickness, hardness and sp²/sp³ ratio.

Reference sample	Technology	Layer thickness (μm)	Chemical composition (at %)	sp ² /sp ³	Hardness (Hv)
DLC 1	Ti-Ta-C	1,2 μm	C**, O, Fe***, Si,	1.3	4800
		1 μm	C, Ti, Fe***, O		
DLC 2	Ti-Ta-C	2 μm	C**, Si, O	1.3	4900
		1,1 μm	C**, Si, O		
		0,3 μm	C, Ti, Si		
DLC 3	Ti-Ta-C	0,9 μm	C**, Fe***, Ti, Si, O	1.3	2050
		0,6 μm	C, Ti, O, Fe***		
DLC 4	Cr-a:C-H	0,6 μm	C**, Si, O,	1,9	2600
		1,2 μm	C**, Si, O, Cr		
		0,75 μm	C, Si, Cr, O		

*EDX analysis and confirmed by XPS Surface measurement.

**Major component.

***Microprobe size is slightly large than DLC thickness and Fe comes from stainless steel contribution.

Previous microstructural analysis and nanoindentation hardness measurement present some contradictions. Similar high sp³ ratio obtained for the DLC 1, 2 and 3 do not correspond to hardness measurement in the case of the DLC3.

The interpretation of hardness gradient measurement curves illustrated in figure 1 will help us to understand this phenomenon. In the following reasoning, it is easier to consider the simplest system where intermediate layer response is negligible and incorporate in substrate response

In a general manner, hardness gradient measurement by nanoindentation on thin films presents four phases as shown in figure 2.

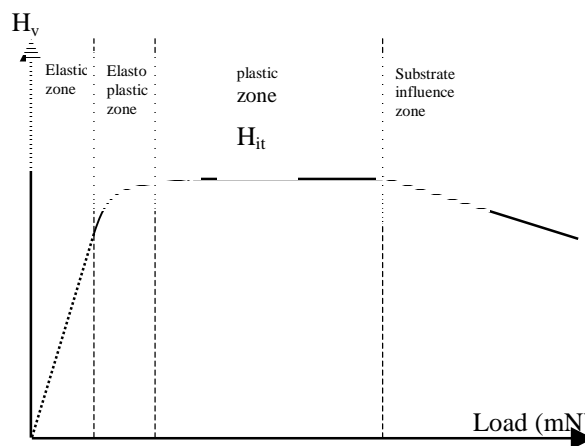


Figure 2 : hardness as a function of the elasto-plastic-substrate response

The first phase concerns the elastic zone and the hardness increases as a linear function of the load for the weakest load. The response of the DLC is only elastic and there is no dislocation activation. Hardness is not exploitable during this phase. The second phase corresponds to the elasto-plastic zone : over the elastic limit, there is a plastic zone and hardness increases more slowly with the load than in the first phase. The third phase would be the plastic zone and the hardness would be constant and is determined in this zone. The fourth zone corresponds to the influence of the substrate. The hardness decreases to that of the stainless steel substrate.

The DLC 4 corresponds very well to this kind of elasto plastic response with a large plastic zone response above 25 mN load.

But sometimes, the influence of substrate begins during the elasto-plastic phase or at the end of elastic phase. This is characteristic of extreme hard thin material on a soft substrate.

This is the main difficulty to determine exactly DLC hardness because before the complete development of the plastic zone, the substrate influence on the response appears. Then the increasing of the curve stop and it decreases to the substrate value. A maximum hardness is observed when substrate influence is more important than pure DLC plastic zone development. This is the case of DLC 1, 2 and 3.

Nonetheless, equivalent sp²/sp³ ratio between DLC 1 and 2 correlates to their corresponding equivalent hardness (4800 and 4900 Hv respectively). So, we can conclude that hardness at the top of the curve is close to the real hardness value.

This is not the case of DLC 3. Measured hardness is more than twice time lower. Knowing that the sp²/sp³ ratio was the same, then the hardness should have been approximatively equal to that of DLC1 and 2. In this case, the rich carbon layer is very thin and the influence of the substrate appears earlier than in the case of other DLC during nanoindentation. DLC 3 hardness would be much higher than this qualitative maximum hardness.

The consequence of this phenomenon is important because a C-H DLC seems harder than a Ta-C one as it is illustrated in figure 1 although this is not the case in reality. The interpretation of the first wear resistance test results briefly describes below will help us to confirm the hardness of the DLC.

Roughnesses of samples measured are shown in the table 3 below.

Table 3 : Roughness's sample.

	Ra (μm)	R (μm)
Substrate non-coated	0,03	0,11
DLC 1	0,80	0,44
DLC 2	0,07	0,43
DLC 3	0,03	0,14
DLC 4	0,03	0,13

According to this table, one can notice that roughnesses of samples DLC 3 and DLC 4 are quiet similar to that of the non coated substrate. But for samples coated by such PVD technology when the thickness of the coating increases, then it surface becomes rough; that is the case for the samples DLC 1 and DLC 2.

Knowing that hardness measured for DLC 1 and DLC 2 are so high, that could lead to a significant wear the antagonist part which is the bearing of the connecting rod. Figure 3 shows the evolution of the mass of connecting rod sample loss successively during the test.

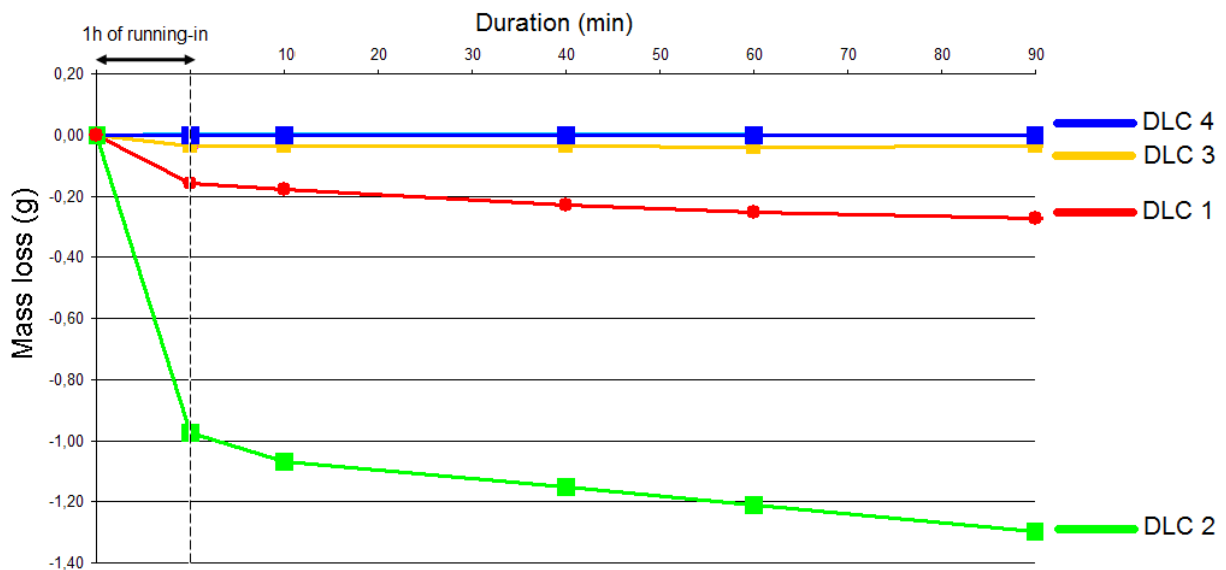


Figure 3 : Weight loss of sample during bench test.

From these tribological tests, one can establish a ranking of the four DLC.

Indeed, DLC 4 which seems to be harder than DLC 3 leads to a low wear of the connecting rod sample compared to that ran with DLC 3. This confirms that the hardness measured by nanoindentation for DLC 3 was minimized.

DLC 1 and DLC 2 produce a significant wear of their antagonist connecting rod bearing with a highest wear for DLC 2. This observation is explained by the surface roughness peaks of these coating made up of Ta-C with is very hard and acts as abrasive tools.

It is clear now that in the strict point of view of mechanical characteristics, DLC 1, 2 and 3 have the same high hardness order and that DLC 4 is soft compared to them.

3. CONCLUSION

In the case of extreme hard thin DLC on a soft substrate, the substrate influence decreases artificially the hardness level determined by nanoindentation. All results confirms the need to finely know the DLC sp²/sp³ ratio by XPS, the multilayer structure and associated thickness by SEM and the hardness gradient measurement by nanoindentation. These three techniques must be used together to correlate with wear and friction resistance test and roughness measurement to classify DLC coatings in automotive industry.

Acknowledgments

We thank PMXP/TAC PSA Peugeot Citroën Laboratory for his helpful and assistance for microstructural characterization.

We thank CIMB/IMPM/TLPA PSA Peugeot Citroën Laboratory for providing DLC samples.

References

- [75] Diamond -like carbon coatings, a new design element for tribological applications, J.Brand, C.Beckmann, B.Blug, G.Konrath, T.Hollstein, Industrial Lubrication and Tribology, 2002, vol. 54, no6, pp. 291-295
- [76] An overview on the tribological behavior of diamond-like carbon in technical and medical applications, R. Hauert, Tribology International, [Volume 37, Issues 11-12](#), November-December 2004, Pages 991-1003
- [77] Recent progress on the tribology of doped diamond-like and carbon alloy coatings: a review , C. Donnet Surface and Coatings Technology, Volumes 100-101, March 1998, Pages 180-186
- [78] Critical review of analysis and interpretation of nanoindentation test data, A.C. Fischer,-Cripps, Surface & Coatings Technology 200 (2006) 4153 – 4165
- [79] G. M. Pharr, W. C. Oliver, MRS Bulletin 17 (1992) 28.
- [80] W. C. Oliver, G. M. Pharr, J. Mater. Res. 8 (2) (1993) 1564.
- [81] Mesure de dureté par nano-indentation, O. Maciejak and P. Aubert, Sciences et techniques de l'Ingénieur NM 7 200 – 1, NM 7 200- 12

RECENT ADVANCES IN SHEAR-BANDING IN BULK METALLIC GLASSES

L. H. Dai and M.Q. Jiang

State Key Laboratory of Nonlinear Mechanics, Institute of Mechanics, Chinese Academy of Sciences, Beijing 100190, China

Abstract. Bulk metallic glasses (BMGs) have a series of intriguing mechanical, physical and chemical properties. However, plastic flow of BMGs at room temperature is prone to be highly localized into nanoscale shear bands, incurring very limit ductility prior to catastrophic fracture and impeding their applications. Therefore, clarifying the mechanism of initiation and propagation of shear band is of central importance in practices. From the scientific viewpoint, the very basic question why and how a nanoscale shear band forms in such atomic-disordered medium is interesting to scientists. Considerable attentions have been attracted to the shear-banding in BMGs during the past decades. This paper reviews the recent advances regarding this aspect, including experiments, continuum as well as atomistic modeling, and theoretical developments.

1. INTRODUCTION

Bulk metallic glasses (BMGs), due to the lack of long-range order (LRO) and the absence of traditional defects such as dislocation and grain boundary [1-5], have a series of intriguing mechanical, physical and chemical properties [6-11]. They have shown wide-spread potential applications as structural and functional materials [12-15]. However, plastic flow of BMGs at room temperature is prone to be highly localized into nanoscale shear bands [16-19]. The initiation and rapid propagation of shear band can induce catastrophic fracture with very limit ductility [20-21], impeding the further applications of BMGs. Essentially, the shear-banding in BMGs is a multiple temporal-spatial and trans-scale process controlled by different physical mechanisms, during which rate-dependent processes such as viscosity/momentum diffusion, thermal/energy diffusion, free volume/mass diffusion, instability nucleation and development should be involved [19, 22-27]. The key question is how these nonlinear and coupled processes with respective spatiotemporal scales govern the shear band formation and evolution in BMGs. In this paper, we present an overview of the inhomogeneous deformation behaviors of BMGs, focusing specifically on the origin (nucleation) and evolution (propagation) of shear-banding. Finally, a summary is concluded.

2. DEFORMATION MAP

In 1977, Spaepen constructed a deformation map of metallic glasses in the space of shear stress, temperature and shear strain rate. This map distinguishes the plastic deformation behaviors into two basic modes: homogeneous where each volume element of the sample contributes to the macroscopic strain [28-29], and inhomogeneous flows, where the strain is highly localized into a few very thin shear bands [16-19, 30-32]. Recently, Schuh et al. [33], Park et al. [34] and Furukawa and Tanaka [35] have developed the deformation map based on experiments or simulations. The crystalline defects such as dislocation, twin or grain boundary do not exist in BMGs without long-range order, which poses a significant challenge for understanding their flow mechanism. Although the precise picture how local atoms respond in deforming metallic glasses is not fully resolved, there is general consensus in metallic glass community that the fundamental unit process underlying plastic flow must be a local structural-rearrangement-type “*flow event*” that can accommodate shear strain. Two popular flow events have been proposed. One is the discrete atomic jump model, first introduced by Spaepen [16]. The other is the local atomic cluster motion, commonly termed the “shear transformation zone” (STZ), firstly proposed by Argon [17]. Following STZ model, Johnson and Samwer [36] further suggested a cooperative shear model (CSM) in terms of a potential energy landscape (PEL) perspective [37-38] to understand the yielding of BMGs. In fact, these “flow events” always correspond to the free volume dynamics within materials [10, 39]. We can therefore understand the flow of BMGs in the mechanical frame of the free volume [19, 26-27, 40].

3. PHYSICAL ORIGIN OF SHEAR BANDING INSTABILITY

The flow theories give a general picture how a metallic glass flows, but do not answer why the flow localize into such extremely thin shear band regions. There are two hypotheses as to why shear bands occur in metallic glasses. The first suggests that, shear-induced dilatation inherently in “flow event” causes the generation and coalescence of free volume, leading to a precipitous drop in viscosity within shear band. This idea was originate in the work of Spaepen [16]. Subsequent works from Argon [17], Steif et al. [41], Vaks [42], Falk and Langer [43], Huang et al. [27], Wright et al. [44] have also shown the importance of free-volume dynamics to shear instability. Here, the free volume formation is indeed a stress-drive structural change; hence, this hypothesis contends that shear banding in metallic glasses has a structural origin. The second contends that shear banding event in BMGs is thermal-initiated [45-46], similar to ASBs in crystalline alloys [47]. In fact, more and more works have indicated that the deformation of metallic glass is a thermo-mechanical process [24, 26, 48-50]. Recently, Jiang and Dai [19] presented a theoretical description of coupled thermo-mechanical deformation of BMG undergoing one-dimensional simple shearing. Through both the perturbation analysis and the shear banding analysis, they have revealed that the shear banding instability is a coupled thermomechanical process dominated by the local free-volume softening and assisted by the thermal softening [19]. It is found from their calculation (see Figure 1) that, during the shear localization process, the sharp bend up in the curve of free volume concentration is prior to that in the temperature rise

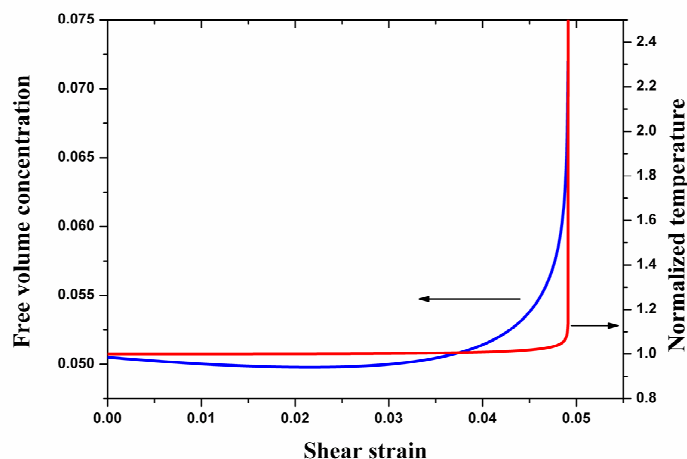


Figure 1. The evolution of free volume concentration and normalized temperature in the shear band as the applied shear strain increases.

The molecular dynamics (MD) simulation is generally believed to an effective way, providing an in situ and real time observation on the shear localization at the atomic level [43, 51-53]. A series of MD works [54-57] have indicated that the structural disordering or free volume in shear band is much more significant than that outside. In other words, the initiation of shear band is always accompanied by the local structural softening. Although it dose not trigger the shear localization, the temperature rise facilitates such process via promoting the free volume crease. At the final stage of shear banding and the resulting failure, the temperature rise should play significant role [58-60].

4. SHEAR BAND EVOLUTION PROCESS

Once it nucleates, a shear band would propagate forward driven by far-field loading. This post-instability process is inextricably linked to final fracture, thus has attracted growing attentions. The first attempt to clarify the detailed process of shear banding in metallic glasses was performed by Masumoto and Murata in 1976 [61]. Using a very hard tensile machine, they indirectly inferred that shear band propagation is rapid intermittent. Since then, great efforts [62-63] have been made to capture the process of single shear band in metallic glasses, but impeded by the limitation of spatiotemporal resolution of experimental technique. Recently, the infrared camera with 1000 Hz frame was used to observe in situ the dynamic shear-banding process in compression of Zr-based BMGs by Jiang et al [64], considering that shear banding causes an increase in temperatures. Such spatial resolution is still not able to seize a full shear banding process. However, based on the successive video

frames, they demonstrated the spatiotemporality of shear bands in metallic glasses. With decreasing strain rates, the plastic flow tends to be inhomogeneous in time and homogeneous in space; while with increasing rates, the plastic flow tends to homogeneous in time and inhomogeneous in space. The temporal feature of shear bands has been confirmed by Dai and co-workers [51]. They conducted MD nanoindentation of Cu-Zr metallic glasses at different loading rates. The simulation result showed that at higher strain rate the shear banding events operate successively, whereas at lower rate the shear events occur intermittently, exhibiting inhomogeneous in time, as shown in Figure 2. Serrated plastic flow phenomena have been widely observed in BMGs under deformation-constrained loading modes such as compression [23, 64-66] and indentation [33, 51-52, 67]. Considering the relation of the flow serration to the shear band dynamics, the shear band velocity could be predicted, suggesting a wide range of values, from $10^1\sim 10^3$ $\mu\text{m/s}$ [65-66, 68] to about several meters per second [68-69]. This range is many orders of magnitude smaller than that one expects, i.e. the shear wave speed of $\sim 10^2\text{-}10^3$ m/s.

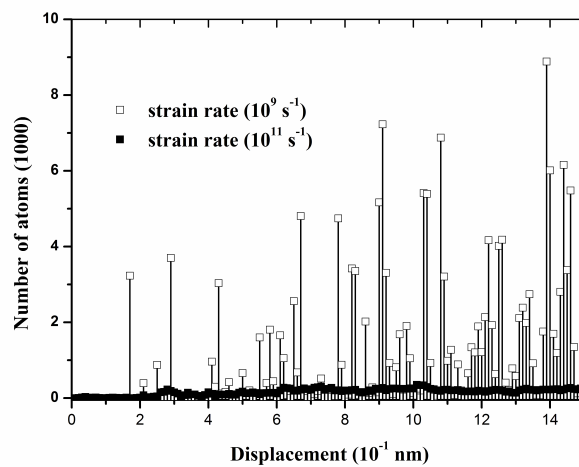


Figure 2. Temporal distributions of shear-banding events during nanoindentation at higher and lower strain rates.

It must be pointed out that the velocity calculations should first be based on the assumption regarding the mode of shear band propagation, i.e. the simultaneous or progressive fashion. Very recently, by developing dynamic “forced” shear technique of hat-shaped specimens, the shear band propagation mode was clearly determined by Jiang and Dai [70], i.e., the shear band is found to initiate in local plastic region, and then propagates with a well-defined front. For an advancing shear band, a very basic question is how much energy the shear band can consume prior to catastrophic cracking. Consequently, they further introduce the shear band toughness, initially proposed by Grady [71] for crystalline alloys, to measure the intrinsic resistance of materials to propagation of shear bands in BMGs [70]. As an important pattern in the evolution, the shear band thickness has attracted much attention [18]. Based on the analogy between dislocation motion and STZ operation, the shear-band thickness has been theoretically predicted by Jiang et al. [72]. The result demonstrates that the correlation between the shear-band thickness and the STZ size does not follow a simple linear relation, and the influence of otherwise parameters such as the activation free volume concentration due to STZs, the shear yield strain and Poisson’s ratio should be involved. The physics underlying the shear band thickness is the local topological instability of the activated STZs.

During the process of loading, if one shear band is not sufficient to dissipate the applied energy, additional shear bands would form within samples. Certainly, such multiplication phenomenon of shear bands is sensitive to loading mode [23], sample geometry [73], material composition [74], atomic topological order [75], etc. The operation of a single shear band will lead to stress unloading or strain relaxation in the vicinity of that shear band. Such local unloading or relaxation causes other shear bands to be excluded from that vicinity, resulting in multiple shear bands with characteristic spacing [76]. In addition, the magnitude of shear band extension can be represented by the shear displacement within the band. At the surface of sample, the shear displacement behaves as a shear offset [77]. It is assumed that a critical shear displacement is required to create a mature shear band, and additional displacement may initiate fracture of the material along the band. Recently, Jiang and Dai [78] performed a specific loading, i.e. turn machining, of a Vit 1 BMG to investigate the multiple shear

bands behavior. It is found that the removed material exhibits a unique lamellar chip due to repeated shear-band formation. The lamellar chip formation or the periodic multiple shear bands can be understood as a self-sustained limit-cycle phenomenon: there is autonomous feedback in stress, free volume and temperature in the primary shear zone, as shown in Figure 3. In particular, based on systematic 4-point bending tests on Vit 1 BMGs and further theoretical analysis, Chen et al [79] have revealed that the shear band propagation is controlled by the free volume softening, and however the resultant momentum diffusion leads to the multiplication of shear bands with a certain characteristic spacing.

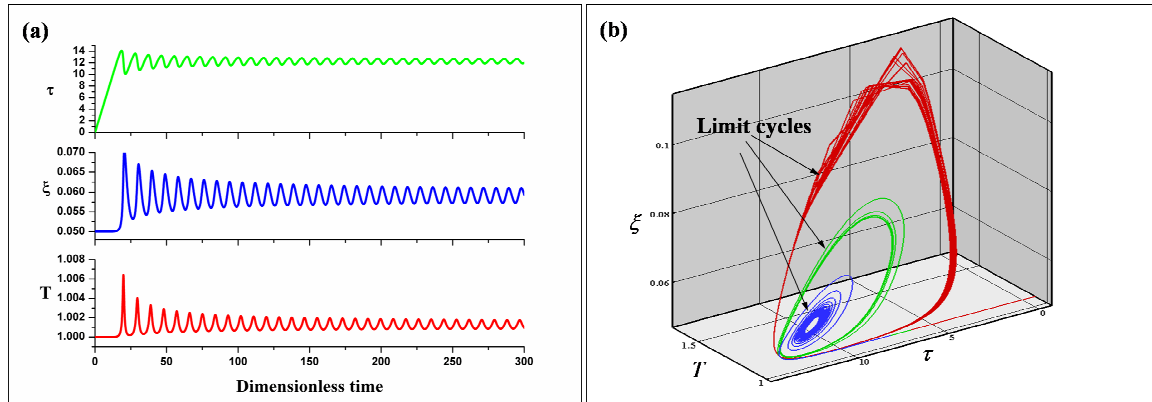


Figure 3. (a) Shear stress τ , free volume concentration ξ , and temperature T vs time t . (b) Trajectories (τ, ξ, T) converging towards stable limit cycles.

As we know, the macroscopic flow of BMGs occurs by the cascade of STZs [36]. As a result, STZs change into a loose configuration with a large volume, resulting in dilatation [80]. Such dilatation inducing hydrostatic stress during STZ formation, and thus the resultant macroscopic plastic flow should depend on pressure or normal stress [21]. Very recently, Sun et al [81] derived an intrinsic theoretical correlation between the pressure sensitivity coefficient and the dilatation factor in BMGs, taking shear-induced dilatation into consideration in STZ operations. Effect of pressure sensitivity on post-shear-banding behavior has been investigated by Yu et al [82] and Dubach et al [83]. It has been found that the increase of pressure sensitivity results in the more deviation of intersection angles of shear bands from 90° , and the shear band density significantly decreases. A similar trend has also been captured by Shi and Falk [53] using MD simulations, in which they performed a series of uniaxial tensile tests on binary models of a glass with different degree of structural relaxation. The enhanced pressure sensitivity or dilatation, on the one hand, facilitates the shear banding initiation, and on the other hand, reduces the multiplication of shear bands. This is apparently paradoxical, however, which can be explained within the content of the free volume. It is well known that during structural relaxation, the free volume within samples is decreased. In such surroundings with lower free volume content, the STZ operations become more difficult, because it requires more significant dilatation of the surrounding matrix. In fact, STZ operations occur preferentially in those regions being higher free volume as relatively less dilatation is required. Therefore, the relaxed samples with lower free volume content make against the formation of shear bands. However, for two samples with identical states, i.e. the same free volume content, if one has more dilatation during deformation, that is, creates more free volume, the shear banding instability should initiate more easily in this sample [19].

5. SUMMARY

As a unique deformation mode and a precursor of catastrophic failure, the nature of shear-banding in metallic glasses has both scientific and practical significance. In summary, we briefly conclude some general consensuses about the shear-banding behaviors as follows:

- 1) The characteristic thickness of shear bands in metallic glasses is about 10 nm, implying that the shear localization in metallic glasses has a structural, rather than a thermal, origin.
- 2) The shear band formation is usually accompanied by the density fluctuation and thus viscosity drop, indicating the lost of short-to-medium range order or equivalently the coalescence of free-volume within the band. The significant temperature rise occurs at the later stage of shear localization, especially at the final failure stage.

- 3) The shear-banding nucleates due to the cascade of stress-activated STZs or flow defects with the thermal fluctuation in the background. The shear band evolution is a dissipation system including thermal, momentum and free-volume dissipation out of shear band.
- 4) The shear bands can branch, intersect, multiple, be arrested and even suppressed, which contributes to the global plasticity of metallic glasses.

Acknowledgments

This work is supported by the NSFC (Grants Nos. 10725211, 11002144, 11023001, and 11021262), the National Natural Science Foundation of China-NSAF. Grant No: 10976100, and the National Basic Research Program of China (Grant No. 2009CB724401).

References

- [1] Bernal J. D., *Nature*, 185 (1960) 68-70
- [2] Miracle D. B., *Nature materials* 3(2004) 697-702
- [3] Sheng H. W., Luo W. K., Alamgir F. M., Bai J. M., and Ma E., *Nature*, 439 (2006) 419-425
- [4] Egami T., *JOM*, 62 (2010) 70-75
- [5] Hirata A., Guan P. F., Fujita T., Hirotsu Y., Inoue A., Yavari A. R., Sakurai T., and Chen M. W., *Nature Materials*, 10 (2011) 28-33
- [6] A.L. Greer, *Science*, 267 (1995) 1947-1953
- [7] W. L. Johnson, *MRS Bulletin*, 24 (1999) 42-56
- [8] A. Inoue, *Acta Materialia*, 48 (2000) 297-306
- [9] Wang W. H., Dong C., and Shek C. H., *Materials Science and Engineering R*, 44 (2004) 45-89
- [10] C. A. Schuh, T. C. Hufnagel, and Ramamurty U., *Acta Materialia*, 55 (2007) 4067-4109
- [11] Trexler M. M., and Thadhani N. N., *Progress in Materials Science*, 55 (2010) 759-839
- [12] Inoue A., and Takeuchi A., *Acta Materialia*, 59 (2011) 2243-2267
- [13] M.F. Ashby, and A.L. Greer, *Scripta Materialia*, 54 (2006) 321-326
- [14] Schroers J., Kumar G., Hodges T. M., Chan S., and Kyriakides T. R., *JOM*, 61 (2009) 21-29
- [15] Wang W. H., *Advanced Materials*, 21 (2009) 4524-4544
- [16] Spaepen F., *Acta Metallurgica*, 25 (1977) 407-415
- [17] Argon A. S., *Acta Metallurgica*, 27 (1979) 47-58
- [18] Dai L. H., and Bai Y. L., *International Journal of Impact Engineering*, 35 (2008) 704-716
- [19] Jiang M. Q., and Dai L. H., *Journal of the Mechanics and Physics of Solids*, 57 (2009) 1267-1292
- [20] Zhang Z. F., Echert J., and Schultz L., *Acta Materialia* 51 (2003) 1167-1179
- [21] Jiang M. Q., Ling Z., Meng J. X., and Dai L. H., *Philosophical Magazine*, 88 (2008) 407-426
- [22] Liu L. F., Dai L. H., Bai Y. L., Wei B. C. and Eckert J., *J. Non-Crystalline Sol.* 351 (2005) 3259-3270
- [23] Liu L. F., Dai L. H., Bai Y. L., Wei B. C., and Eckert J., *Mat. Chem. Phys.*, 93 (2005) 174-177
- [24] Dai L. H., Yan M., Liu L. F., and Bai Y. L., *Applied Physics Letters*, 87 (2005) 141916
- [25] Liu L. F., Dai L. H., Bai Y. L., Wei B. C., and Eckert J., *J. Mat. Reserch*, 21 (2006) 153-160
- [26] Gao Y. F., Yang B., and Nieh T. G., *Acta Materialia*, 55 (2007) 2319-2327
- [27] Huang R., Suo Z., Prevost J. H., and Nix W. D., *J. Mech. and Phys. Solids*, 50 (2002) 1011-1027
- [28] Schroers J., *Advanced Materials* 21 (2009) 1-32
- [29] Kawamura Y., Nakamura T., and Inoue A., *Scripta Materialia*, 39 (1998) 301-306
- [30] Ravichandran G., and Molinari A., *Acta Materialia*, 53 (2005) 4087-4095
- [31] Xie S., and George E. P., *Acta Materialia*, 56 (2008) 5202-5213
- [32] Wu F. F., Zhang Z. F., Jiang F., Sun J., Shen J., and Mao S. X., *Appl. Phys. Let.*, 90 (2007) 191909
- [33] Schuh C. A., Lund A. C., and Nieh T. G., *Acta Materialia*, 52 (2004) 5879-5891
- [34] Park K.-W., Lee C.-M., Lee M.-R., Fleury E., Falk M. L., and Lee J.-C., *Appl. Phys. Let.*, 94 (2009)
- [35] Furukawa A., and Tanaka H., *Nature materials*, 8 (2009) 601-609
- [36] Johnson W. L., and Samwer K., *Physical Review letters*, 95 (2005) 195501
- [37] Debenedetti P. G., and Stillinger P. H., *Nature*, 410 (2001) 259-267
- [38] Stillinger F. H., *The Journal of Chemistry Physics*, 88 (1988) 7818-7825
- [39] Heggen M., Spaepen F., and Feuerbacher M., *Journal of Applied Physics*, 97 (2005) 033506
- [40] Thamburaja P., *Journal of the Mechanics and Physics of Solids*, 59 (2011) 1552-1575
- [41] Steif P. S., Spaepen F., and Hutchinson J. W., *Acta Metallurgica*, 30 (1982) 447-455
- [42] Vaks V. G., *Physics Letter A*, 159 (1991) 174-178
- [43] Falk M. L., and Langer J. S., *Physical Review E*, 57 (1998) 7192-7205
- [44] Wright W. J., Hufnagel T. C., and Nix W. D., *Journal of Applied Physics*, 93 (2003) 1432-1437
- [45] Leamy H. J., Chen H. S., and Wang T. T., *Metallurgical Transactions*, 3 (1972) 699-708

- [46] Liu C. T., Heatherly L., Easton D. S., Carmichael C. A., Schneibel J. H., Chen C. H., Wright J. L., Yoo M. H., Horton J. A., and Inoue A., *Metallurgical and Materials Transactions A* 29A (1998) 1811-1820
- [47] Bai Y. L., *Journal of the Mechanics and Physics of Solids*, 30 (1982) 195-207
- [48] Yang Q., Mota A., and Ortiz M., *Computational Mechanics* 37 (2006) 194-204
- [49] Zhang H. W., Maiti S., and Subhash G., *J. Mechanics and Physics of Solids*, 56 (2008) 2171-2187
- [50] Thamburaja P., and Ekambaram R., *J. Mechanics and Physics of Solids*, 57 (2007) 1263-1273
- [51] Jiang S. Y., Jiang M. Q., Dai L. H., and Yao Y. G., *Nanoscale Research Letters*, 3 (2008) 524-529
- [52] Jiang M. Q., Jiang S. Y., Ling Z., and Dai L. H., *Computational Materials Science*, 46 (2009) 767-771
- [53] Shi Y. F., and Falk M. L., *Physical Review Letters*, 95 (2005) 095502
- [54] Bailey N. P., Schiøtz J., and Jacobsen K. W., *Physical Review B*, 73 (2006) 064108
- [55] Cao A. J., Cheng Y. Q., and Ma E., *Acta Materialia* 57 (2009) 5146-5155
- [56] Li Q. K., and Li M., *Physical Review B*, 75 (2007) 094101
- [57] Li Q. K., and Li M., *Applied Physics Letters*, 88 (2006) 241903
- [58] Yang B., Liu C. T., and Nieh T. G., *Applied Physics Letters*, 88 (2006) 221911
- [59] Yang B., Liu C. T., Nieh T. G., Morrison M. L., Liaw P. K., and Buchanan R. A., *Journal of Materials Research*, 21 (2006) 915-922
- [60] Liu Y. H., Liu C. T., Wang W. H., Inoue A., Sakurai T., and Chen M. W., *Physical Review Letters*, 103 (2009) 065504
- [61] Masumoto T., and Murata T., *Materials Science and Engineering* 25 (1976) 71-75
- [62] Neuhauser H., *Scripta Metallurgica*, 12 (1978) 471-474
- [63] Vinogradov A. Y., and Khonik V. A., *Philosophical Magazine*, 84 (2004) 2147-2166
- [64] Jiang W. H., Fan G. J., Liu F. X., Wang G. Y., Choo H. and Liaw P. K., *Int. J. Plast.*, 24 (2008) 1-16
- [65] Song S. X., and Nieh T. G., *Intermetallics* 17 (2009) 762-767
- [66] Maaß R., Klaumünzer D., and Löffler J. F., *Acta Materialia*, 59 (2011) 3205-3213
- [67] Dai L. H., Liu L. F., Yan M., Wei B. C., and Eckert J., *Chinese Physics Letters*, 21 (2004) 1593-1595
- [68] Klaumünzer D., Maaß R., Dalla Torre F. H., and Löffler J. F., *Appl. Phys. Letters*, 96 (2010) 061901
- [69] Wright W. J., Samale M. W., Hufnagel T. C., LeBlanc M. M., and Florando J. N., *Acta Materialia*, 57 (2009) 4639-4648
- [70] Jiang M. Q., and Dai L. H., *Acta Materialia*, 59 (2011) 4525-4537
- [71] Grady D. E., *Journal of the Mechanics and Physics of Solids*, 40 (1992) 1197-1215
- [72] Jiang M. Q., Wang W. H., and Dai L. H., *Scripta Materialia*, 60 (2009) 1004-1007
- [73] Huang Y. J., Shen J., and Sun J. F., *Applied Physics Letters*, 90 (2007) 081919
- [74] Liu Y. L., Wang G., Wang R. J., Zhao D. Q., Pan M. X., and Wang W. H., *Science*, 315 (2007) 1385-1388
- [75] Das J., Tang M. B., Kim K. B., Theissmann R., Baier F., Wang W. H., and Eckert J., *Physical Review Letters*, 94 (2005) 205501
- [76] Conner R. D., Li Y., Nix W. D., and Johnson W. L., *Acta Materialia*, 52 (2004) 2429-2434
- [77] Conner R. D., Johnson W. L., Paton N. E., and Nix W. D., *J. Applied Physics*, 94 (2003) 904-911
- [78] Jiang M. Q., and Dai L. H., *Acta Materialia*, 57 (2009) 2730-2738
- [79] Chen Y., Jiang M. Q., and Dai L. H., *Unpublished work*, (2011)
- [80] Jiang M. Q., and Dai L. H., *Physical Review B*, 76 (2007) 054204
- [81] Sun L., Jiang M. Q., and Dai L. H., *Scripta Materialia*, 63 (2010) 943-946
- [82] Yu G. S., Lin J. G., Mo M., Wang X. F., Wang F. H., and Wen C. E., *Materials Science and Engineering A*, 460-461 (2007) 58-62
- [83] Dubach A., Prasad K. E., Raghavan R., Löffler J. F., Michler J., and Ramamurty U., *Journal of Material Research*, 24 (2009) 2697-2704

MESOSCALE MODELLING OF FAILURE IN PARTIALLY SINTERED METALS : NUMERICAL TECHNIQUES AND ANALYSIS OF FRAGMENTATION PATTERNS

N. Durr, M. Sauer and S. Hiermaier

Fraunhofer Institute for High-Speed Dynamics, Ernst-Mach-Institut, Eckerstr. 4, 79104 Freiburg, Germany

Abstract. In this contribution, we present a methodology for the mesoscale analysis of failure and fragmentation of partially sintered metals. As model materials, we used metallic samples constituted of either copper or iron or a mixture of both. They are produced from cold-pressed powders with subsequent sintering at 700°C. By varying the manufacturing pressure, different material variants were obtained. Based on the statistical analysis of micrographs, three-dimensional voxel-based representative volume elements (RVE) were generated with the software GEODICT at Fraunhofer ITWM, Kaiserslautern. The RVE topology is an agglomerate of metallic grains bonded by an artificial material that represents inter-granular cohesion. From these RVEs, finite element models were built, the simulations were done with the commercial code LS-DYNA. The material data for these mesoscopic models was derived partly from literature and partly by the fitting of simulated homogenized stress-strain response to experimental tensile tests. In order to represent intergranular failure, the so-called node-split method was used at interface nodes: the nodes are split once a critical effective plastic strain failure criterion is reached in the adjacent elements. The modelling approach was applied to the simulation of small scale fragmentation tests. In the experiments, millimetre-sized cubes impacted a thin aluminium plate at velocities between a few hundred and a few thousand meters/second. The resulting fragmentation pattern can be analysed and qualitatively compared to corresponding simulations with the mesoscale model. Simulation results are used to derive statistical distributions of fragment..

1. INTRODUCTION

The ability to predict the influence of manufacturing parameters on the behavior of polygranular materials under impact loads could speed up the material development process in areas such as defense technology, chemical processing, refining, etc. The aim envisaged in this project is the development and validation of numerical methods for the simulation of the mechanical behaviour of these polygranular materials at grain scale. These methods shall enable the predictive analysis of the dependencies of the mechanical properties - specifically the fragmentation behavior - on the morphological and constitutive nature of a material at grain scale. Simulation capability of this kind can be effectively applied to design new materials with tailored mechanical properties.

The behavior of such materials is governed by a number of factors. Apart from loading and sample geometry, the mechanical properties of grains and grain interfaces, i.e. the mesoscopic material properties, and the mesoscopic material structure, i.e. distribution and sizes of grains and pores as well as their shapes and orientations, play an important role.

The desired simulation capability comprises several aspects. First, a computational method must be identified that allows the parameter-controlled generation of representative volume elements (RVEs) of the considered materials with realistic microstructures. This includes the task of generating computational meshes of these microstructures. Secondly, a finite-element solver for continuum mechanical conservation and constitutive equations is needed, which permits a three-dimensional, time-dependent simulation of the response of an RVE to external loads, including a treatment of inter-granular failure and fragmentation. As a last step, the developed model shall be used in simulations of impacts on aluminum plates and deliver relations between the fragment size distribution and the model parameters (grain distribution, size of grains, type of material, etc.).

2. CONSTRUCTION OF THE RVE

2.1. Investigated materials

In order to have common, well-known materials that do not react upon impact, commercially available copper powder (Cu, type AK <160µm, manufacturer: ECKA) and iron powder (Fe, type ASC100.29, manufacturer: Höganäs) were selected as raw materials. Whereas the Fe powder has a rough particle surface, the Cu powder consists of spherical particles, see Fig. 1 (left and middle). The typical grain size for both powders ranges from 5 µm to 100 µm. Both powders are produced in a spraying process (atomized Fe/Cu). In order to study the effect of using a mixture of the two base materials, a mixture with an equal volume share of both materials was

also prepared. Manufacturing of the partially sintered samples was done at the branch of the Fraunhofer Institute for Manufacturing Technology and Applied Materials Research (IFAM) in Dresden, Germany, and comprised the following two main steps:

- Uniaxial cold pressing of 130 mm long and wide, 8 mm thick samples with varying pressure values (300, 350, 400, 500 and 580 MPa). Zinc stearate was used as lubricant for the matrix.
- Sintering with a peak temperature of 700 °C, this temperature was kept constant for one hour.

To provide an impression of the structure of the final material, a micrograph for the CuFe mixture pressed at 400 MPa is given at the right of Fig. 1.



Figure 1. Iron powder (left), spherical copper powder (middle) (both pictures by Fraunhofer IFAM, Dresden, the additional scale has been manually inserted); micrograph of processed CuFe mixture (right).

2.2. Derivation of a mesoscopic structure

The polygranular materials investigated here consist of grains with a size of 5 µm up to 100 µm. Since the shape of the grains is to be represented in a finite element model, the element size needs to be smaller than the smallest grains that shall be modeled, i.e. 2 µm. Macroscopic samples are in the range of at least a few millimeters and therefore cannot be modeled in microscale resolution with the computer hard- and software available today. In order to obtain information for the macroscale, the well-known concept of Representative Volume Elements (RVEs) is used. In general, RVEs are used to compute a homogenized material response for an applied loading. This response, e.g. in the form of a homogenized stress state, can then be used in a macroscopic analyses. RVEs can also be used for the derivation of macroscopic material models if a sufficiently large number of loading states are analyzed.

A statistical evaluation of chord length distributions in micrographs on which metallic grains and pores are discernable was the first step of the structure generation process. The chord length is defined as the straight distance between two points on the boundary of the cross section of an object (grain or pore); if a regular pattern of chord lengths is analyzed, one obtains a chord length distribution, i.e. a statistically descriptive measure which characterizes the size and the shape of one or more objects. On the bases of chord length distributions, RVE's were generated at the "Fraunhofer Institut für Techno- und Wirtschaftsmathematik" in Kaiserslautern, Germany, using their software „GEODICT“ [1]. The RVEs were optimized until a reasonable coincidence of the chord length distributions of micrograph and model was obtained. An exemplary structure is shown on Fig. 2. The generated structures have an edge length of 0.8 mm and consist of 64 Million so-called voxels with an edge length of 2 µm. Each grain is identified by a unique number. As can be seen in the figure, intra-granular pores were disregarded in the model. The grain shape in the model ranges from irregular to almost spherical, as is the case in the micrograph.

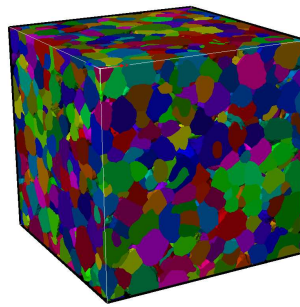


Figure 2. RVE resulting from micrograph analysis, edge length 0.5 mm. The picture of the RVE is a smoothed representation of the original RVE, the smoothed RVE was generated with the software “Simpleware” of Simpleware Limited, Exeter, United Kingdom.

2.3. RVE meshing, Failure Modeling Approach and Inter-Granular Boundary Generation

For use in finite element simulations, the RVE is meshed with cubic elements. To reduce the sample size as far as possible and, thus, to keep the computational effort practicable, the size of the RVE was reduced by cutting off parts before it was meshed. This size reduction was done in small steps while checking that the computed homogenized mechanical response of the RVE response remains the same. The checking was enabled through repeated computation of the homogenized stress response under a tensile loading while the size was decreased. In a second step, the mesh was coarsened. The optimal RVE, in the sense of the computation time, is the sample with the smallest number of finite elements that remains representative. In our case, a cubic volume with 0.4 mm edge length and a mesh resolution of 8 μm turned out to be appropriate. The influence of the RVE size on the resulting tensile stress/strain curve for a typical low rate tensile loading is depicted in Fig. 3. It can be seen that the stresses at the onset of yielding at a strain of about 0.005 is practically identical for RVE sizes 0.4 and 0.8 mm, only small deviations occur for 0.2 mm. The differences in the post-peak (softening) part of the curves occur due to the localized failure under tensile loading and the homogenization of the strains over the entire RVE. The peak stresses, however, are practically identical.

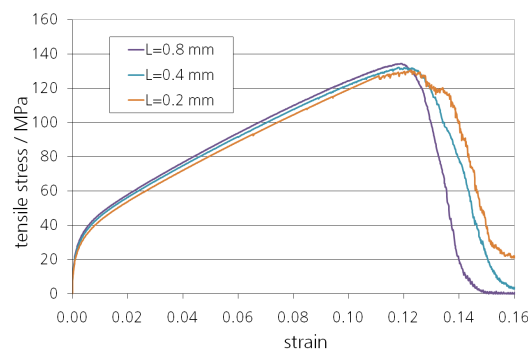


Figure 3. Influence of the RVE size in a typical tensile test simulation, “L” is the length of one edge of the cubic RVE. The same finite element size of 4 μm was used in all three cases.

An important question in modeling sintered material fragmentation is how to numerically describe the failure at grain boundaries. In first tests, we inserted a special “boundary material” at all inter-granular boundaries, and used the conventional, so-called “element erosion” in combination with an effective plastic strain criterion to describe the failure of a grain boundary. However, as elements are simply deleted, this technique leads to a considerable mass and volume loss which leads to unrealistic results especially under shear and compression loading. Therefore, we decided to use the so-called “Node-Split” technique which is available in LS-DYNA. In this approach, a node of the computational mesh can split as soon as an effective plastic strain threshold is reached in all elements the node is connected with. We used the Node-Split technique in combination with an inter-granular boundary material discretized with one layer of elements for modeling a reduced stiffness at the boundaries. This turned out to be necessary when RVE simulations were compared with tensile tests, see section 3. A special algorithm was developed that replaced elements belonging to neighboring grains such that

all grains were clearly separated by boundary material (see Fig. 4). These elements will be called “border elements” in the following.

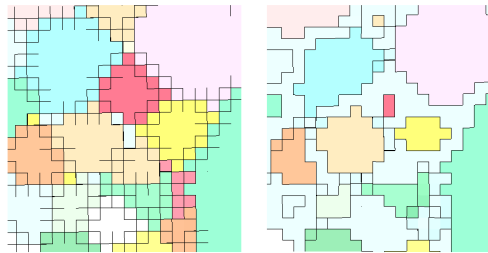


Figure 4. (left) RVE plane section without border generation; (right) RVE plane section after insertion of border elements. The thin lines indicate potentially split element faces.

3. DERIVATION OF MESOMECHANICAL MATERIAL PARAMETERS

For each type of material constituting the RVE (copper, iron and border), a material law was defined. An isotropic elastic-plastic law with linear hardening was assumed (see Fig. 5). The values of parameters depend on the material considered (metallic grain or border).

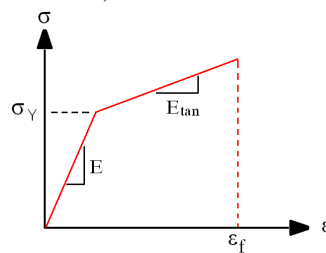


Figure 5. Schematic linear elastic – plastic material law used for metallic grains. σ_Y denotes the yield strength, E is Young’s modulus, E_{tan} is the plastic hardening modulus.

3.1 Material Parameters from Literature

The elastic parameters (Young modulus E and Poisson’s ratio ν) that are assigned to metallic grains were derived from literature, as well as values of initial yield stress and hardening slope for the plastic behavior. Since mechanical properties of the bulk grains of metallic powders were not available, averaged values of typical copper and cast iron were used.

3.2 Derivation of Parameters for Inter-Granular Boundaries

The parameters for inter-granular boundaries highly depend on the fabrication process and thus cannot be found in the literature. As they cannot be measured directly, they were derived by inverse parameter identification, i.e. by simulating tests and optimizing the parameters in a procedure similar to the one used in [2]. The principle we followed here was to add as few parameters as possible. Physically, the border is supposed to be weaker than the metallic grains. To determine realistic border values, a quasi-static tensile test was simulated with a first set of parameters and compared to the same experimental loading case. This comparison is made possible as the averaged stress and strain measured on the RVE are considered macroscopic values, according to the definition of a RVE. A three-step optimization process has then been applied, Fig. 6:

- (1) Optimization of the initial yield stress: this value is set through the initial yield stress of the border.
- (2) Optimization of the plasticity curvature: a damage model of the RVE at grain scale is realized. For this purpose a failure interval, in terms of critical effective plastic strains, is uniformly distributed to all inter-granular nodes. This allows the successive birth of cracks in the RVE during the loading and leads to a softened stress increase (concave curvature).
- (3) Optimization of the global failure point: this point is also coupled to the damage model of the RVE, a global stress decrease occurs when enough nodes have split after the neighboring elements reached the effective plastic strain criterion.

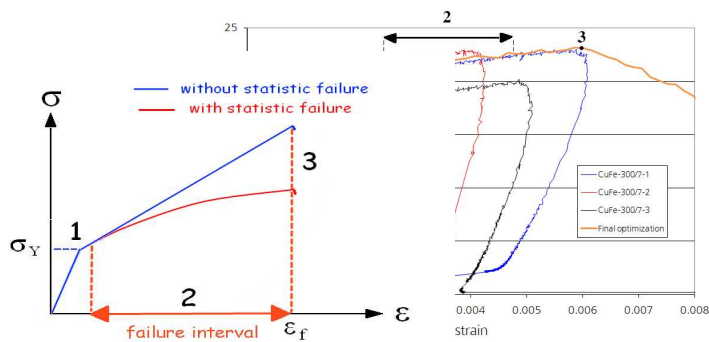


Figure 6. (left) Schematic visualization of the optimization of the mesomechanical material parameters (numbers 1 to 3 are explained in the text); (right) Simulation with optimized material parameters for the CuFe 300 MPa material type compared to three test results. The measured strain values are based on clip-gauge data.

As illustrated in Fig. 6, there is considerable variability in the measurements for that case (Cu 300 MPa). A more detailed investigation of that variability would require a number of tests that is large enough for a statistic analysis; however, this was beyond the scope of this study. Instead, the curve that exhibits a medium stress level has been selected as reference curve.

Another observation from Fig. 6 is that the softening behavior (region after peak stress) differs significantly from the experimental data. One reason is that the test data in the figure are from clip gauge measurements: As the cracks in the samples occurred outside the measuring section, the strain decreases. The small slope in the softening region occurs as an artifact, as we compare a small RVE with a large tensile test sample and therefore use different reference lengths for the strain calculation.

4. CUBE IMPACT TESTS ON ALUMINUM PLATE

4.1. Experimental setup and observations

The impact experiments we will use as reference for simulations were conducted with cubes (side length 3 mm) fired against an aluminum plate (thickness 0.8 mm) [3]. A single witness plate of titanium (4 mm thickness) was used for capturing fragments. The experiments have been executed with a gas gun and a sabot catch system which ensures that the target plate is not impacted by sabot parts. The experiments were done with the Fe 580 MPa and the CuFe 300 MPa sinter material. The impact speed was chosen in three different velocity regions of about 500 m/s, 1500 m/s and 2600 m/s. All experiments have been conducted with an air pressure in the impact chamber of 0.5 bar.

At the lowest impact velocity of about 500 m/s, the CuFe and the Fe sample perforate the target plate without significant fragmentation. The perforation causes a rectangular hole in the target plate, whereas the higher impact velocities generate circular holes in the target plate with a diameter of about 6 mm. At a velocity of about 1500 m/s, see Fig. 7 (top left), the CuFe sample produces some larger fragments in the central region around the shot axis, whereas the Fe sample is primarily flattened to the shape of a truncated pyramid, see Fig. 7 (bottom left). In the case of the CuFe sample, clouds of fine fragments occur in the region behind the cube. These fragments are visible in the photographs as a dark gray region. Single fragments of this small size are beyond the spatial resolution of the camera. This cloud of fine fragments does not occur in the Fe experiment under comparable impact velocity. At 2600 m/s, Fig. 7 (right), fine fragments are generated in both cases, and a fragment cloud typical for hypervelocity impacts is observed.

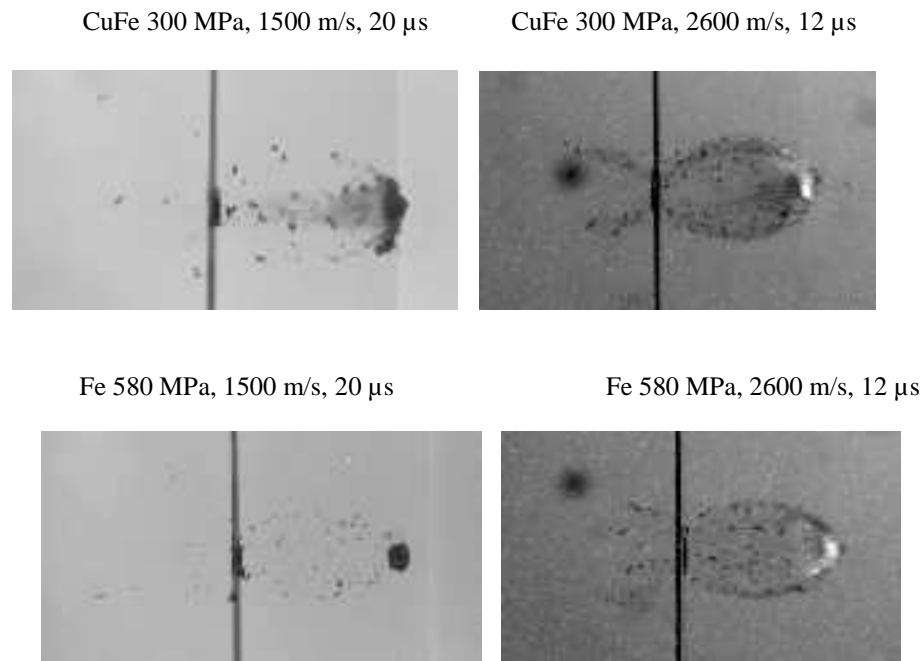


Figure 7. Perforation of an aluminum target plate (0.8 mm thickness) by cubes (3 mm side length) made of partially sintered material [3]. Projectile material, impact velocity and time after impact are given at the top of each picture.

4.2. Exemplary Impact Calculations on the Mesoscopic Scale

The developed mesoscopic model allows for the simulation of further loading states, as far as the scope of assumptions is respected. In the exemplary calculations presented below, no strain rate dependency is incorporated in the mesoscopic material laws, instead, the values are identical to those identified through the process described in section 3. However, as dynamic mesoscale simulations showed, different macroscopic material responses are obtained when the strain rate is varied. This is due to mesoscopic inertia effects that induce velocity-dependent internal stresses.

Impact simulations of CuFe and Fe cubes (same fabrication pressures than in experiments) of size 0.4*0.4*0.4 mm on an aluminum plate of 0.1 mm thickness were performed. Fig. 8 shows simulation results of Fe cubes, which correspond to “downscaled” versions of the tests presented in the previous section. The “downscaling” is necessary for mesoscale simulations as the original cube size of 3 mm is so large that individual grains could not be represented in a computational mesh, the required number of elements would be far too large. Using this kind of simulations, impact velocities of 150 m/s, 475 m/s, 1600 m/s and 2600 m/s were analyzed, for CuFe and Fe cubes.

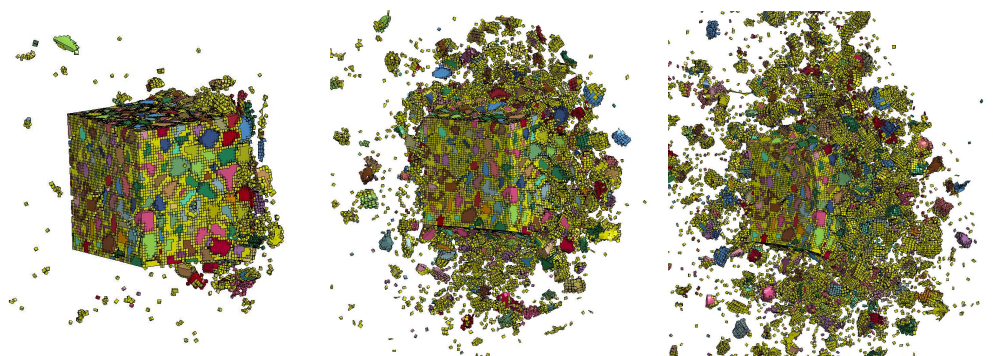


Figure 8. Examples of mesoscale simulation results: Fe cube after plate perforation. (left) $v=475$ m/s; (middle) $v=1600$ m/s; (right) $v=2600$ m/s.

Although the results of the “downscaled” simulations are not directly comparable to the tests, they qualitatively reproduce some of the features that can be observed in the original tests, as summarized here:

- 1) Partial fragmentation occurs for low velocities (CuFe at 150 m/s, Fe at 475 m/s).
- 2) The weaker the material, the higher is the degree of fragmentation at a given velocity (compare Fe at 475 m/s yields approximately the same degree of fragmentation as CuFe at 150 m/s).
- 3) Complete fragmentation for Fe occurs at 1600 m/s and higher velocities.
- 4) The higher the velocity, the finer the fragments.
- 5) The hole in the aluminum plate generated by the perforation is rectangular for low and circular for high velocities.

4.3. Quantitative fragmentation analysis from numerical parameter studies

Besides the qualitative analysis of the number of fragments, from which some trends can be derived when the impact velocity evolves or when the material varies, a precise quantitative analysis of the fragment size distribution is necessary. Currently, a reliable, exact and efficient method for the determination of fragment size distributions from the experiments shown above is still under development. However, the analyses can be done on the basis of the simulation results which are presented in the following. A good method for the analysis of fragmentation from simulations consists in counting the number of fragments in fragment mass classes. The histograms on Fig. 9 show such an analysis for an RVE of edge length 0.4 mm, composed of the materials CuFe 300 MPa and Fe 580 MPa, respectively. The mass classes on the horizontal axis indicate the upper value of the respective interval. A separate frequency scale is used for the smallest fragments (which are single elements in the simulation).

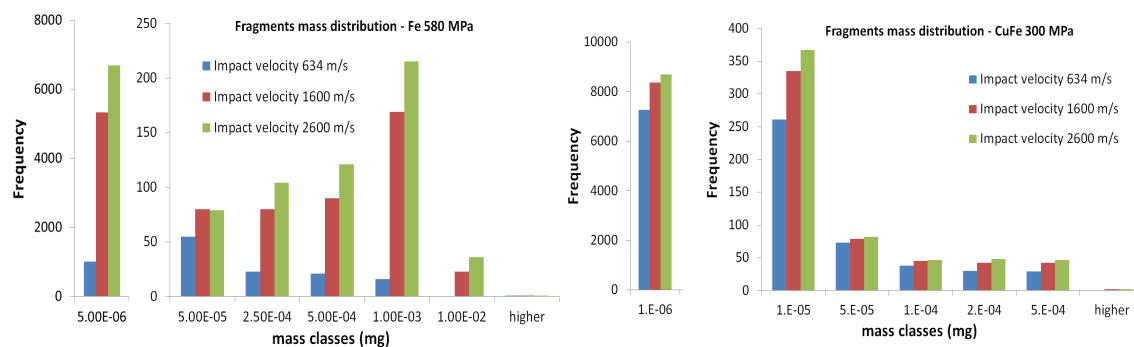


Figure 9. Histograms representing fragments mass distribution within mass classes for RVEs of 0.4 mm edge length. (left) CuFe 300 MPa ; (right) Fe 580 MPa.

A natural limit for this type of analysis is the mesh resolution, as no smaller fragment than the element size can be obtained. This explains the overpopulation of the smallest class, however, the mass proportion of these fragments is small compared to the mass of the entire cube. Still, some conclusions can be drawn from these histograms. As the impact velocity increases, each mass class possesses a bigger population of fragments. The overall mass of the RVE is conserved between the different impact velocities as the “higher” class consists of the remaining non-fragmented block after the impact. Its size increases with decreasing impact velocities. It is interesting to notice that the deviation of distribution between different impact velocities is drastically weaker for the Fe 580 MPa than for CuFe 300 MPa. As the latter sample was fabricated with a weaker pressure (and subsequently less grain bonding), and as copper is not as stable as iron, small impact velocities already lead to considerable fragmentation; a high degree of fragmentation is thus observed for CuFe at all velocities, which reduces the effect of impact velocity. On the other hand, the stronger Fe 580 MPa sample fragments little for small velocities, but shows high fragmentation for high velocities. This can be seen in the higher frequency deviation in each mass class.

Currently, as already mentioned, it is not possible to simulate real-size (millimeter-sized) samples due to the high number of Finite Elements needed to represent the microstructure. For a comparison of simulated fragment size distributions from downscaled simulations with experimental observations in the future, the influence of the scaling needs to be investigated. Therefore, the fragmentation of cubes with two edge lengths, 0.4 mm and 0.2 mm, upon impact on plates of thickness 0.1 and 0.05 mm, respectively, was simulated. It is important to mention that the scaling was done on the cube and plate dimensions only, whereas the grain sizes and their distribution remains the same. Thus, the 0.2 mm cube has been obtained as a sub-volume of the 0.4

mm cube. The analysis of the fragmentation is done based on an average fragment volume for each sample and impact velocity. This average fragment volume was defined as the median of the cumulative volume distribution.

Table 1. Average fragment volume (in $0.001 * \text{mm}^3$) after impact of RVE against aluminum plate. (top) CuFe 300 MPa; (bottom) Fe 580 MPa.

CuFe 300 MPa Unit: $0.001 * \text{mm}^3$	v = 634 m/s	v = 1600 m/s	v = 2600 m/s
L = 0.4 mm	0.169	0.109	0.093
L = 0.2 mm	0.257	0.106	0.094
Fe 580 MPa Unit: $0.001 * \text{m}^3$	v = 475 m/s	v = 1600 m/s	v = 2600 m/s
L = 0.4 mm	54.5	30.1	0.118
L = 0.2 mm	7.18	3.69	0.117

For both materials, at the velocity of 2600 m/s, a nearly identical average fragment size for both cube dimensions was obtained. The same can be said for 1600 m/s for the mixture sample. For the other cases, deviations between both scales occur and no direct relation between fragment size and scale can be explicitly formulated. From this it can be concluded that there is an upper threshold of the average fragment volume for which the scaling approach is valid. The cubic root of the average fragment volume can be taken as a measure for the effective fragment size. Using this measure, the ratio of the effective fragment size to the cube length can be set up as a simple criterion for the validity of the scaling. In our case, the scaling seems to hold for values of this ratio up to 0.25, which means that the scaling is only valid if the cube edge length is at least four times larger than the obtained effective fragment size.

5. CONCLUSION

The methodology for the multiscale analysis of deformation and failure of partially sintered metals outlined in this paper contains several steps. From microstructure analysis, a RVE that contains material and geometric information was built. Mesoscopic material parameters were determined by fitting homogenized simulation results to results of experimental tensile tests. The material model chosen was selected as the one that yields a good accordance of experimentally measured and homogenized simulated response with the smallest number of parameters.

Furthermore, experimental cube impact tests on aluminum plates were performed. They were simulated using mesoscopic models with downscaled cube and plate dimensions. Similar fragmentation phenomena could be observed from qualitative comparison of experiments and simulations. A first version of a criterion for the validity of the scaling was derived from a set of simulations. This criterion shall be refined in the future, thus allowing for a quantitative comparison of simulated fragment size distributions from mesoscale models with real-scale tests.

Acknowledgments

We thank Frank Bagusat and Martin Lück, both scientists at EMI, for providing the experimental basis of this work. The project was partly sponsored by the United States Department of the Navy, Office of Naval Research (ONR), under grant No. N00014-07-1-1053, this support is gratefully acknowledged.

References

- [1] www.geodict.com
- [2] Wicklein, M.; Thoma, K.: Numerical investigations of the elastic and plastic behavior of an open-cell aluminum foam. *Mat Sc. Eng.*, 2005, A 397: 391-399.
- [3] Sauer, M.; Bagusat, F.; Durr, N.; Klomfass, A.: Fragmentation of Partially Sintered Materials – Experimental Investigation and Mesoscale Simulation. *Proceedings of the 11th Hypervelocity Impact Symposium, Freiburg 2010* (in print).

NANO MATERIALS FOR ARMOR APPLICATIONS

S. Yeshurun

VP & CTO Plasan Sasa Ltd, Israel

In the nature small molecular building blocks are joined to produce nanostructures with defined geometries and specific functions. It is becoming apparent that nature's bottom-up approach can be mimicked to produce engineered materials properties. This tremendous opportunity has led to the development of hard protective coating, hard materials for armor applications such as transparent ceramics, high efficiency ceramic armor, cutting tools as well as wide variety of sensors applications. Nano powder as ceramics as well as other nano particles offers unique opportunity to scale down and control the properties of bulk materials at the nanometer scale.

In Plasan we are involve in wide diverse of nano materials research and development including process, materials, physical and mechanical and ballistic properties evaluation methods. In the presentation we will explore our recent activities in the CNT fibers and nano ceramics.

Our preliminary results show that with CNT fibers we can build new composites architecture with multi-functional and high mechanical properties. We also found that producing nano scale Alumina could lead to superior properties compare to the current commercial available Alumina.

POLYCRYSTALLINE CERAMICS WITH FINE MICROSTRUCTURE FOR ARMOR APPLICATIONS

G. Rossiquet¹ F. Bernard² and P. Forquin³

¹ UMR 3080 CNRS/Saint-Gobain, Saint-Gobain CREE, Cavaillon, France

² UMR 5209 CNRS, Département nanosciences - Laboratoire ICB, Dijon, France

³ UMR 7554 CNRS, Laboratoire de Physique et de Mécanique des Matériaux, Metz, France

Ceramic materials for armor application are devoted to lightweight armor systems for protection against light caliber. They are capable of displaying significantly better protective performance than an equivalent weight of metal armor. Their use allows significant reduction in armor weight due to the low density and also a good protection against armor piercing ammunitions due to their high ballistic properties. The design of these systems is typically based on the mechanical properties (hardness and strength) of the ceramic material and its ability to fracture the core. A rear compliant layer is used to catch the debris from the projectile and the ceramic material. Investigations here are focused on the development of silicon carbide for armor application, which combines low residual porosity and a very fine microstructure. Such a fine grain size represents a technological breakthrough in comparison to the actual ceramic solutions for this application and improved mechanical properties are expected.

The work is separated into two parts. Ceramic processing is used to disperse the raw powders, homogenize sintering additives and shape green parts. Sintering investigations in solid and liquid states, using two different methods (pressureless-sintering and spark plasma sintering), are a key step to reach the optimal microstructure for each material. Spark Plasma Sintering seems to be a very good alternative in comparison to the pressureless-sintering to avoid the grain growth thanks to the pressure applied and the lower sintering temperatures involved. Low quantities of sintering additives are used. It is possible to produce large samples with a high density, a fine microstructure and a good homogeneity.

The second part of this study is devoted to the comprehension of impact resistance and to its link with the microstructure. Up to now, ballistic tests (shooting on plates) are used to ascertain effectiveness of ceramics for armor applications and to rank the performance of the various candidate materials. Results and ranking are very empiric and the correlation between armor ballistic performance and fundamental material properties have been unsuccessful. Modeling and numerical simulation are used and materials data are obtained through mechanicals experiments in quasi-static and dynamic regimes.

PROCESSING OF ULTRAFINE-GRAINED NICKEL BY DISLOCATION ACTIVITIES AT INTERMEDIATE DYNAMIC STRAIN RATE : MICROSTRUCTURE EVOLUTION AND MECHANICAL PROPERTIES

L. Farbaniec¹, A. Abdul-Latif², J. Li¹, H. Couque³ and G. Dirras¹

¹ LSPM, CNRS, UPR 3407, Institut Galilée, Université Paris 13, 99, avenue J. B. Clément, 93430, Villetaneuse, France

² Laboratoire d'Ingénierie des Systèmes Mécaniques et des Matériaux, 3 rue Fernand Hainaut 93407 St Ouen Cedex, France

³ Nexter Munitions, 7 route de Guerry, 18023 Bourges, France

A Dynamic Plastic Deformation (DPD) is a relatively new technique of synthesizing bulk nanostructured or ultrafine-grained materials [1-3]. By means of DPD concept a commercially pure (99,97 %) texture free coarse-grained Ni (8.73 μm) was deformed under compression at room temperature at an intermediate dynamic strain rate of about $3.3 \times 10^2 \text{ s}^{-1}$. The resulting microstructure and texture evolution have been investigated along with mechanical behaviors and the underlying deformation mechanism after quasi-static compressions at room temperature and at a strain rate of $2 \times 10^{-2} \text{ s}^{-1}$. Scanning Electron Microscopy (SEM) and Transmission Electron Microscopy (TEM) investigations reveal that the initial equiaxed grains evolved into a mixed structure, including sub-grains and elongated grains. The latter giving rise to a laminar-like structure with a distance between high angle grain boundaries in the range of several hundred nanometers, depending on the location along the sample's diameter. The mechanical behavior was investigated along the normal and axial directions, respectively parallel and perpendicular to the DPD compression axis. Overall, the stress-strain response demonstrate an increase of the yield strength (from 620-640 MPa to 650-750 MPa, depending on the location and orientation), about 8-9 times compared to the initial state (80 MPa), most probably related to the grain refinement and dislocation density increase. In addition, the change of compression loading direction and of the texture orientation lead to differences in work hardening behavior.

References

- [1] Huang F, Tao NR, Lu K, J. Mater. Sci. Technol., 2011, 27(1), 1-7.
- [2] Li YS, Tao NR, Lu K, Acta Materialia 56, 2008 230-241.
- [3] Li YS, Zhang Y, Tao NR, Lu K, Acta Materialia 57, 2009, 761-772.

DYNAMIC COMPACTION RESISTANCE SINTERING : A NEW PROCESS FOR PROCESSING ADVANCED MATERIALS

P. Acquier^{1,2,3}, S. Lemonnier¹, C. Terner¹, E. Barraud¹, T. Grosdidier², A. Rusinek³, N. Allain-Bonasso² and J. Capelle^{3*}

¹ Institut franco-allemand de recherches de Saint-Louis, 5 rue du Général Cassagnou, 68301 Saint-Louis Cedex, France

² Laboratoire d'Etude des Microstructures et de Mécanique des Matériaux – CNRS UMR 7239, Université Paul Verlaine - Metz, 57045 Metz-Cedex, France

³ Laboratoire de mécanique Biomécanique Polymère Structure, ENIM – Ecole Nationale d'Ingénieurs de Metz, 1 route d'Ars Laquenexy, 57078 Metz Cedex 3, France

Advanced materials processing is most often intimately linked to the development of new advanced processes. Among them, Spark Plasma Sintering (SPS) has recently been the focused of many studies thanks to its high potential in the sintering stage of the powder metallurgy technique. The principle is similar to hot pressing since metal or ceramic powder is contained in a graphite die subjected to quasi-static loading and heated. However, in the SPS process, heating is obtained by Joule effect through the application of high current densities at low voltage. By this way, high heating rates and low sintering temperatures (the load application is accompanied by a decrease in the sintering temperature) can be achieved. Both these parameters allow avoiding or at least limiting grain growth phenomenon during sintering stage. This particularity makes the SPS process a good choice for the processing either of nanomaterials or of dense materials with densities close to the theoretical one (~99%) or both of them. However, the complete densification of materials is often difficult to obtain due to the limitation of the low applied loading (<100MPa) limited by the mechanical resistance of the graphite die. A change in the pressure nature and/or pressure value could result in achieving fully dense materials.

With this aim in view, and in opposition to the quasi-static loading applied in SPS, other compaction methods such as dynamic compaction could be used. Among them, Split Hopkinson Pressure Bar (SHPB), which is commonly used to dynamically characterize solid materials, appears to be an interesting process. Indeed, it was reported in the literature the compaction at room temperature of titanium powder [1] and bio-compatible material [2] with this process. Due to its high deformation rate ($10^2 - 10^4 \text{ s}^{-1}$) and high pressure values (~GPa) capacities, this process could be chosen as a mean for compacting powders.

Taking these elements into consideration, it has been expected that the combination of SPS and dynamic compaction could lead in the achievement of dense materials exhibiting original properties. Indeed, due to the strong amount of defects which can be introduced in the structure during the deformation, phenomena such as dynamic recrystallisation leading to refinement of the microstructure or metastable structures reaching are expected. Thus, a new process called Dynamic Compaction Resistance Sintering (DCRS) has been developed at ISL since several years. It was envisaged through the coming along of SPS technology on top of a SHPB. Development of the process has been done in terms of materials, electrical parts, mechanicals parts, data acquisition and safety in order to combine these two technologies. Numerical simulation has also been computed in parallel to ensure the good mechanical behavior of the system. After presenting the device in details, the compaction and sintering behavior of model materials such as copper and alumina powders by DCRS will be presented and their properties discussed.

Reference

- [1] H.-A Häggblad and al., Powder Technology 154 (2005) 33 – 42
- [2] M.Trécant, PhD Thesis, Faculté de chirurgie dentaire, Université de Nantes, 1996

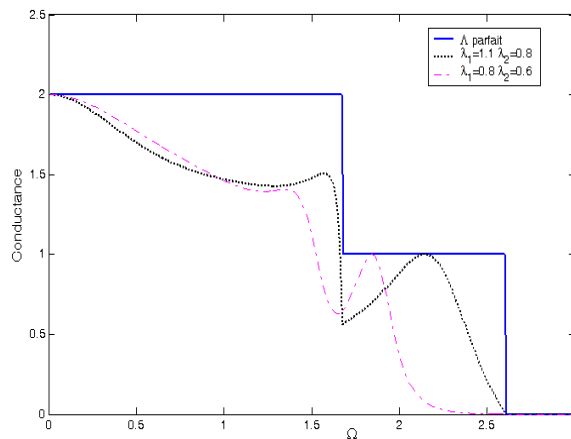
SCATTERING PROPERTIES OF 2D-MESOSCOPIC SYSTEM WITH LACUNA DEFECT

M. Bouateli, R. Tigrine and B. Bourahla

Laboratoire de Physique et Chimie Quantique, Département de Physique, Faculté des Sciences, Université Mouloud Mammeri de Tizi-Ouzou, B.P. N° 17 RP, 15000 Tizi-Ouzou, Algérie.

The scattering and the localisation phenomena of elastic waves in disordered low dimensional systems, such as disordered surfaces is an active research field. The interest in the dynamics of disordered surfaces containing defects has been motivated by increased need to acquire knowledge of their electronic and mechanical properties for developing advanced microelectronic, optical and magnetic devices, as well as the thrust toward nanometer-scale structures. The surface presents itself at the nanometric scale as a distribution of several types of defects such as atomic steps, atoms, terraces and wells with irregular profiles.

In this work, we present a study of the scattering phenomena at the inhomogeneous lacuna in crystalline solid surfaces. The breakdown of translation symmetry induced by the inhomogeneity, gives rise to localized modes of vibration in its neighbourhood. The mathematical framework of the matching method [1-4] and the Newton equation are used in our study which can be applied to analyze the phonon scattering phenomena of the full problem arising from absence of the translation symmetry.



The transmission and reflection probabilities as well as the elastic wave average transmittance across the defect are determined and numerical results are presented in a large band of scattering energies. This illustrates theoretically the variation of the scattering spectra for the hardening and the softening of the elastic constants in the neighbourhood of the lacunar and the coherent coupling between these localized states induced by the defect and the travelling modes of the system lead to Fano resonances in the vibration spectra.

SOL-GEL SYNTHESIS AND DIELECTRIC CHARACTERISATION PROPERTIES OF LEAD-FREE (1-x) Na_{0,5}Bi_{0,5}TiO₃-xBaTiO₃ BASED CERAMICS

S. Kennour¹, A. Chaouchi¹, S. d'Astorg^{2,3}, M. Rguiti^{2,3}, C. Courtois^{2,3}, S. Marinel⁴ and M. Aliouat¹

¹ *Laboratoire de Chimie Appliquée et Génie Chimique de l'Université Mouloud Mammeri de Tizi-Ouzou, Algérie.*

² *Laboratoire des Matériaux Céramiques et Procédés Associés– Université de Valenciennes et du Hainaut-Cambrésis, Z.I. du Champ de l'Abbesse, 59600 Maubeuge, France.*

³ *Univ. Lille Nord de France, F-59000 Lille, France*

⁴ *Laboratoire CRISMAT, UMR 6508 CNRS/ENSICAEN 6 Bd Maréchal Juin, 14050 Caen cedex, France.*

The crystal structure, microstructure, dielectric and ferroelectric properties of (1-x)Na_{0,5}Bi_{0,5}TiO₃-xBaTiO₃ ceramics compositions for x= 0, 0.03, 0.05, 0.07 and 0.1 were investigated. Structural variation according to the system composition was investigated by X-ray diffraction analyses. The results revealed that the synthesizing temperature for pure perovskite phase powder prepared by the present sol-gel process is much lower (600°C), and a rhombohedral-tetragonal morphotropic phase boundary (MPB) is found for x= 0.07 composition which shows the highest remanent polarization value and smallest coercive field. The optimum dielectric and piezoelectric properties were found in the 0.93Na_{0,5}Bi_{0,5}TiO₃-0.07BaTiO₃ compositions, show good performance with good piezoelectric properties (piezoelectric constant d₃₃ of 120 pC/N), the good polarization behaviour was observed with remnant polarization (P_r= 12,18 μC/cm²), coercive field (E_c= 2,11kV/mm), and enhanced dielectric properties ε_r >1500. The 0.93Na_{0,5}Bi_{0,5}TiO₃-0.07BaTiO₃ composition ceramics is a promising lead-free piezoelectric candidate for applications in different devices.

ULTRAFAST FAILURE OF AU NANOFILMS IN NONEQUILIBRIUM HEATING PROCESS

W. Ma, X. Ma and Z. Zhou

Institute of Mechanics, Chinese Academy of Sciences, China

This article deals with the experimental and theoretical studies on the thermomechanical response of Au-Cr double-layer nanostructure irradiated by ultrashort laser pulses. First, we have completed the ultrafast thermal shock experiments and observed evident nonthermal ablation phenomenon of Au nanofilm caused by ultrashort laser pulses. A stripe pattern of narrow bands on a contrasting background is visible in the area irradiated by laser and a crack developed along the stripe is caused by the tension stress acting in the Au nanofilm plane. Though the material undergoes large plastic deformation, not any evidences show that the compressive deformation takes place in the Au nanofilm. Moreover, the nonthermal ablation and damage of the Au nanofilm in the heating area is visible after irradiated, implying that heat diffusion is not important during irradiated by laser. Secondly, to study the ultrafast thermomechanical responses of Au nanofilm, a modified continuum model on the base of the chemical view point of atom structure is developed. In this model, the Au nanofilm is considered as an electron-lattice system. The thermal expansion effect of hot electron gas due to absorption of photon energy induces an additional action to the electron-lattice system. Thus, in nonequilibrium energy transport process, the ultrafast thermal shock caused by band electron expansion produces an acting force inducing the damage and failure of the system. Presently, the viscoplastic Au nanofilm is assumed to comply with the Bodner-Partom unified constitutive model and elastic Cr substrate is isotropic. The analytical results show that, the modified continuum model can better describe the nonequilibrium dynamic responses of Au nanofilm and gives a logical explanation for the nonthermal ablation or failure of Au nanofilm during nonequilibrium heating of ultrashort laser pulses; conversely, the classical continuum model only approximately describes the stress evolution during thermal equilibrium and hardly reveal the generation of the ultrafast thermal stresses during nonequilibrium heating.